Electronic Thesis and Dissertation Repository

4-13-2018 2:00 PM

Polarimetric SAR as a Tool for Remote Sensing Salt Diapirs, Axel Heiberg Island, Nunavut

Elise M. Harrington
The University of Western Ontario

Supervisor
Neish, Catherine D.
The University of Western Ontario

Graduate Program in Planetary Science

A thesis submitted in partial fulfillment of the requirements for the degree in Master of Science

© Elise M. Harrington 2018

Follow this and additional works at: https://ir.lib.uwo.ca/etd

Part of the Geology Commons

Recommended Citation

Harrington, Elise M., "Polarimetric SAR as a Tool for Remote Sensing Salt Diapirs, Axel Heiberg Island, Nunavut" (2018). *Electronic Thesis and Dissertation Repository*. 5321.
https://ir.lib.uwo.ca/etd/5321

Abstract

The costs and hazards associated with traditional geological mapping have driven rapid advancement of remote predictive mapping techniques using satellite data. However, few studies have implemented synthetic aperture radar for geology. This study uses quad-polarimetric RADARSAT-2 and PALSAR-1 data to produce circular polarization ratio images over Axel Heiberg Island, Nunavut, Canada. These images are used to characterize the radar properties of gypsum and anhydrite diapirs and secondary salt deposits that have been mapped using visible and near infrared, short wave infrared, and thermal infrared spectroscopy. Diapiric salt outcrops appear rough in radar at the C-Band and L-Band (cm-dm) scales, whereas the secondary salts appear smooth. Ground truthing in the field confirms that salt diapirs are rough from millimeter to meter scale, whereas secondary salt minerals are precipitating on smoother surfaces, like floodplains and hillslopes. These results show that radar can be used to differentiate between diapiric and secondary salt exposures.

Keywords

i

Co-Authorship Statement

The spectral mapping of gypsum and anhydrite exposures in this thesis was performed by Maria Shaposhnikova under the supervision of Dr. Catherine Neish and Dr. Livio Tornabene. Future papers will include co-authorship with these colleagues.

Acknowledgments

Table of Contents

List of Tables

List of Figures

List of Appendices

Chapter 1

1   Introduction

The Canadian High Arctic contains abundant, underexplored mineral and petroleum resources (Embry and Mayr 1991). However, geological field mapping in the Arctic is limited by seasonal and logistical constraints, so these reserves and their host rocks have only been assessed at a preliminary level. With the rise of orbital Earth observation and geographic information systems (GIS), more industries and government organizations are applying remote sensing for surveying land. Despite major advances in satellite imaging techniques, few studies have incorporated synthetic aperture radar (SAR) for geological mapping. The aim of this thesis is to serve as a proof-of-concept study incorporating SAR for geological mapping with optical and multispectral imagery. Near-infrared wavelengths and SAR are sensitive to vegetation; because the Canadian High Arctic has very little vegetation, it is an ideal place to test analyses using these products.

The mapping targets in this study are gypsum ($CaSO_4 \cdot 2H_2O$) and anhydrite ($CaSO_4$) salt exposures on Axel Heiberg Island, Nunavut. Axel Heiberg Island contains abundant anhydrite diapirs from the Carboniferous Otto Fjord formation. Gypsum and anhydrite are soft and soluble minerals, therefore the diapirs erode rapidly when exposed at the surface. These erosion characteristics make diapirs prominent in SAR backscatter images, which are sensitive to surface roughness. Rougher surfaces generally scatter radar signals in all directions, including back at the receiving antenna, thereby producing a stronger response. In contrast, smoother surfaces will reflect incident beams away from the SAR antenna. The highly eroded outcrops on Axel Heiberg Island produce stronger signatures in SAR compared to the more resistant surrounding rocks. An integral part of this project is to ground-truth remote observations, and field investigations in July 2017 confirm that the diapirs are rough at all (mm to m) scales. In contrast, gypsum and anhydrite minerals are dissolving out of the diapirs and are precipitating to form smoother deposits, like floodplains, as well as precipitating in perennial springs.

The objectives of this thesis are to demonstrate the use of satellite multispectral data to identify and map anhydrite and gypsum on Axel Heiberg Island, and to use SAR to differentiate between diapiric and secondary salts. Field investigations are used to ground truth the remote predictions concerning the surface roughness, and subsequent SAR signature, between diapiric and secondary salt exposures. Samples of both types of salts were also sampled from the field for X-Ray Diffraction (XRD) lab analysis to compare the salt compositions against spectroscopic observations.

1.1 Remote Sensing and GIS

Remote sensing is a rapidly developing field. The tools and methods used for Earth observation have been greatly refined over the past century. Although the invention and refinement of photography took place during the early to mid-1800s, it was not until the First and Second World Wars that aerially acquired images were used for regional reconnaissance, and that specialists were specifically trained in their interpretation. World War II spurred the first use of the electromagnetic spectrum outside of the visible range for remote sensing purposes (Campbell and Wynne 2011). The first radar systems were land-based and had meter-scale wavelengths. These were appropriate for naval navigation but not detailed imaging. The Allied countries worked to reduce radar wavelengths, thereby producing the first radar imaging systems used by aircraft. Throughout the 1950s and 1960s, real-aperture radar systems and synthetic aperture radar (SAR) were developed and refined, with applications broadening from military to earth sciences (Campbell 2004).

The first spaceborne imagers were launched in the 1960s (Elachi 1988). These paved the way for Landsat 1. Landsat 1, launched in 1972, carried an experimental Multispectral Scanner (MSS) which not only measured reflected sunlight in the optical range, but also at two infrared wavelengths. The use of the MSS for imaging beyond the optical range opened doors for multispectral analysis, i.e. the identification of surface materials based on their physical absorption and emission at a molecular level. With near global coverage and new opportunities for spectral analysis, Landsat 1 inspired a new era for satellite Earth observation worldwide (Campbell and Wynne 2011). In 1978 the launch of SEASAT opened the doors for spaceborne active remote sensing for scientific purposes.

SEASAT demonstrated the utility of microwave and radio wavelengths to study ocean topography, meteorology, and regional land topography (Elachi 1988). The success of SEASAT spurred the launch of more spaceborne SAR, like Canada's RADARSAT-1, which was launched in 1995. Along a similar timescale, new techniques were developed using polarized radar beams. Polarimetric radars can receive horizontally, vertically, or circularly (clockwise or counterclockwise) polarized radar beams. The way in which radar beams interact with a surface can alter their polarization states, and these properties can make polarimetric radar a useful tool in characterizing surface materials (Neish and Carter 2014). Satellite radar data has since been used for soil moisture monitoring, forestry, ocean studies, agriculture, meteorology, snow and ice monitoring, and geological mapping (Elachi 1988; Campbell 2004). By the 1980s and 1990s satellite observation technology had been improved to provide imagery at much finer resolutions (Campbell and Wynne 2011). The success of RADARSAT-1 lead to the development of RADARSAT-2, launching in 2007, with fully polarimetric capabilities. RADARSAT-2 is the primary radar used in this study.

As satellite remote sensing has produced data with increasingly high spatial resolution, the demand for digital maps has also grown considerably. Geographic information systems (GIS) have emerged concurrently with remote sensing to keep pace with technology required to process and interpret satellite imagery. "GIS" can stand for both "geographic information systems" which refers to the physical hardware and software of computer-based cartographic systems, as well as "geographic information sciences" which refers to the holistic theory and applications behind geographic visualization techniques and data organization (McMaster and Manson 2010). This thesis uses GIS in the sense of both definitions simultaneously, as discussing the science also implies use of GIS software programs. Although the first geographic information systems were created in the 1960s including the Minnesota Land Management Information System and the SYMAP (synagraphic mapping) software, GIS did not develop as a field until the creation of the National Center for Geographic Information and Analysis in 1988. The center hosted a series of workshops to advance core topics in GIS research, prompting the foundation of the University Consortium for Geographic Information Science in 1994 (McMaster and Manson 2010).

Today, use of GIS spans the public and private sectors, including geological surveying, human geography, environmental monitoring, and emergency services (Antenucci et al. 2010; Mockert 2010). Satellite remote sensing data can aid in many of these areas. For geological surveying, the use of aerial photographs, the Global Positioning System (GPS), as well as topographical maps can substantially increase mapping efficiency and reduce time needed in the field. Similarly, by using GIS to combine satellite imagery, field measurements, and subsurface data from geophysical surveys and drill cores, geologists can more quickly pinpoint where ore deposits or petroleum reservoirs may be located (Antenucci et al. 2010). The use and demand for GIS technical skills has accelerated since the 1980s and today software like ESRI's ArcGIS and Harris Geospatial Solutions's ENVI are widespread, with many universities and private companies offering courses and workshops in their use.

1.2 Radar

Despite these advances in remote sensing and GIS technologies, few attempts have been made to use synthetic aperture radar (SAR) for geological mapping. Unlike spectroscopy or optical imagery, radar data provides information about the physical properties of a surface, not the absorption and reflection of sunlight by different atomic structures (Neish and Carter 2014). Because SAR backscatter is sensitive to slope variation, it is useful in highlighting structural morphologies. On a finer scale than slope variation, SAR is sensitive to surface roughness. Rough surfaces scatter radar beams in more directions than smooth surfaces, so rough surfaces provide stronger radar response because more of the beam is scattered back to the receiving antenna. Conversely, smooth surfaces reflect the signal away from the receiver, producing weaker responses, unless the incidence angle of the radio wave is very close to the local slope angle (Figure 1). An analogy for such a smooth surface would be a flashlight inflecting on a mirror. At an angle, all the light from the flashlight is reflected away from its source, but if the flashlight is aimed perpendicular to the mirror, the amount of light returning to the source is high.

Radar is also sensitive to electrical and physical properties of materials, in addition to surface roughness. The depth of penetration (d) (Equation 1) is dependent on the radar's wavelength (λ) and the electrical properties of the surface (real component of dielectric
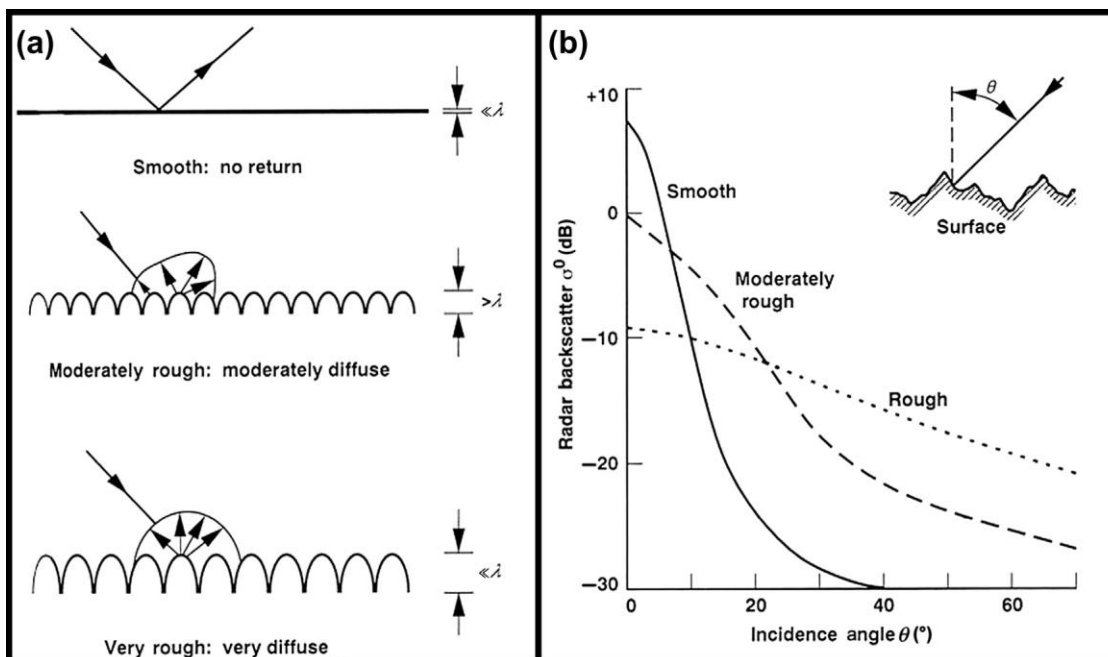
Figure 1: The effects of surface roughness and incidence angle on radar response. a) Smooth surfaces reflect radio waves away from the source, providing weak backscatter response at large incidence angles. Rougher surfaces scatter the incident beam in many directions, including back towards the receiver, producing a stronger response. b) An exception to the general rule that smooth surfaces produce weak backscatter responses is when the incidence angle of the radar beam is close to local slope angle. The closer that incidence angle is to the local slope of a surface, the stronger the received response (From Neish and Carter 2014, after Farr 1993).

permeability, ε' and loss tangent, tan δ) (Neish et al. 2011).

$$d = \frac{\lambda}{2\pi\varepsilon'^{\frac{1}{2}}\tan\delta} \qquad (Equation\ 1)$$

The loss tangent (Equation 2) is "ratio of the imaginary to the real part of the complex dielectric permittivity," where f is the frequency of the electromagnetic wave, σ is the free charge conduction, and ε is the absolute permittivity of the material (Carrier et al. 1991; Campbell 2002).

$$\tan \delta = \frac{\varepsilon''}{\varepsilon'} = \frac{\sigma}{2\pi f \varepsilon} \qquad\qquad (Equation\ 2)$$

As the dielectric constant increases, penetration depth decreases. Although highly conductive materials, such as metals, seawater, or wet soils, have shallower penetration depths, they also reflect radio waves with higher intensities, producing higher radar backscatter. Resultingly, radar signatures over wet soils may be more heavily influenced by dielectric properties than by surface texture – an important consideration when using SAR to characterize relative roughness.

Because active remote sensing provides its own signal (i.e. is not dependent on reflected sunlight or emitted radiation), SAR can be used to image during nighttime hours and is useful in mapping areas frequently obscured by cloud coverage, like many wet tropical areas (Elachi 1988). Canada launched RADARSAT-1 in 1995 which carried a singularly polarized C-Band ($\lambda = 5.6$ cm) SAR. The singular polarization meant that RADARSAT-1 was only able to transmit and receive radar beams transmitted in a horizontal polarization (HH). RADARSAT-1 was used for mapping structural geology features for ore and petroleum exploration, as well as for mapping prominent fault lines for earthquake research. It was also very successful in monitoring Arctic and Antarctic ice, monitoring environments in tropical areas, and it had agricultural, forestry, and oceanography applications. Its successor, RADARSAT-2, is also a C-Band SAR but with full quad-polarization capabilities, meaning it can both send and receive radar beams in horizontal and vertical polarizations. However, very few studies have taken advantage of the quad-polarimetric capabilities of RADARSAT-2 for geological exploration, with previous work emphasizing Quaternary surficial materials, vegetation, and soil moisture (Shelat et al. 2012; Collingwood et al. 2014). Only preliminary studies have explored the potential for bedrock mapping (Singhroy et al. 2004; Choe et al. 2017). This thesis represents a proof-of-concept study to apply polarimetric SAR for geological mapping. We have combined polarimetric SAR, thermal infrared (TIR), visible and near infrared (VNIR) spectroscopy, true-colour satellite imagery, pre-existing geological maps, and ground truthing for our study. The SAR we are using includes C-Band ($\lambda = 5.6$ cm) from RADARSAT-2 and L-Band ($\lambda = 23$ cm) from Japan's Phase Array Type L-Band SAR

(PALSAR-1). The TIR, VNIR, and true-colour imagery come from the ASTER and Landsat-8 satellites, and salt compositional predictions from spectroscopy are compared against XRD sample analysis. By combining multiple data sources, we can find the most effective methods to implement radar as a tool for remote predictive geological mapping of salt diapirs on Axel Heiberg Island, Nunavut.

1.3   Salt Diapirs

The target rocks in this study are sulphate salt diapirs. Salt minerals are less dense than other types of rock. They form diapirs form through the differential loading of denser rock on top of a thick salt deposit (Ramberg 1981; Suppe 1985). Salt minerals behave plastically on a geological timescale, and "ooze" up through and away from the overburden, much in the way a glacier flows in response to gravity. There are three main categories of evaporite minerals that undergo tectonism at low confining pressures. These are halite (NaCl), sulphates [predominantly anhydrite ($CaSO_4$) and its hydrated form, gypsum ($CaSO_4 \cdot 2H_2O$)], and bittern salts [potash minerals, like sylvite (KCl)]. Each of these mineral groups are highly soluble (anhydrite: 1.97 g/l, gypsum: 2.0 g/l, halite: 264 g/l, sylvite: 340 g/l at standard temperature and pressure). They are termed "evaporites" because they commonly precipitate out of aqueous solution in large water bodies as water is removed from the system via solar evaporation. They precipitate in reverse order of their solubility, with anhydrite and gypsum precipitating at 75-85% water loss, anhydrite and gypsum precipitating with halite from 85-90% water loss, pure halite precipitating at 90-98% water loss, and bittern salts precipitating in extreme salinity at ~99% water loss (Warren 2006). Because halite requires more water loss to precipitate than gypsum or anhydrite, it typically forms in shallower waters.

These precipitated minerals can form rock units up to 100s of metres thick stratigraphic units within a sedimentary basin. In shallow seas, like the Sverdrup Basin during the Carboniferous, gypsum can precipitate at the rate of up to 5 cm/yr, and halite can precipitate over 10 cm/yr (Jackson and Hudec 2017). Gypsum and anhydrite can also precipitate in areas of salt and freshwater mixing, but these are not considered evaporites. Bittern salts do not play an important role in the salt tectonics on Axel Heiberg Island, and are not discussed further. Although Axel Heiberg Island hosts abundant carbonate

formations, which may also be evaporitic in origin, these have significantly higher internal strength than salt minerals, and therefore do not flow under the same conditions that lead to salt tectonism.

The term diapir comes from the Greek word diaperno meaning "to penetrate" (Jackson and Hudec 2017). Diapirs are named as such because of the way they typically form mounds or domes that discordantly puncture through overlying rock units. The components of a diapiric system include an autochthonous salt layer, which is the concordantly deposited evaporite layer (parallel to other strata), and allochthonous salt layer, which has mobilized, forming the domes. The primary force effecting salt movement is the gravitational force (Ramberg 1981). The denser overburden weighs down on the buried salt layer, pushing it outwards, much like pushing down on the chocolate coating of a candy bar and watching the caramel force itself out. The overburden, or chocolate, is brittle and breaks whereas the salt layer, or caramel, squishes viscously and flows out laterally. The salt that flows away is considered withdrawn, or expelled, and can either feed an upward-moving diapir, or thicken the autochthonous source layer. The salt rises to compensate for the energy potential of the sinking overburden (Jackson and Hudec 2017).

In addition to gravitational loading, displacement and thermal loading can also mobilize salt units. Whereas gravitational loading is a constant strain, displacement loading is more episodic, pertaining to pulses of tectonic compression or extension. Salt is weak, and tends to localize regional strain, therefore pre-deformed salts are more susceptible to displacement loading (Suppe 1985). Thermal loading can contribute to the fracturing of the overburden, providing space for confined salts to move upwards. Rocks expand when heated, and salt rock expands at a much greater rate than siliciclastic rock. Therefore, stress accumulates if there is no space for the salt to expand, causing brittle deformation in overlying overburden (Jackson and Hudec 2017). Viscosity and frictional forces resist salt movement – viscosity is the salts' internal strength, and friction refers to drag forces that cause shearing at salt-overburden contacts. Friction plays a smaller role in thicker evaporite layers (Jackson and Hudec 2017).

Not all salt tectonism results in dome shaped structures. Salt sheets and salt canopies form when allochthonous salts spread out laterally and form concordant units (Hudec and Jackson 2006). Visually, these can look like a flat cap mushroom, growing out of the salt source layer. The mushroom stock is diapiric in nature, and is discordant with the strata, while the cap (salt sheet) spreads out laterally, concordant with the strata. Salt sheets have only one salt stock feeding them, whereas salt canopies are coalescing salt sheets that are fed by multiple salt stocks that often share the same source layer (Figure 2). Salt canopies usually have welded salt layers where the sheets coalesce (Hudec and Jackson 2006; Jackson and Hudec 2017).
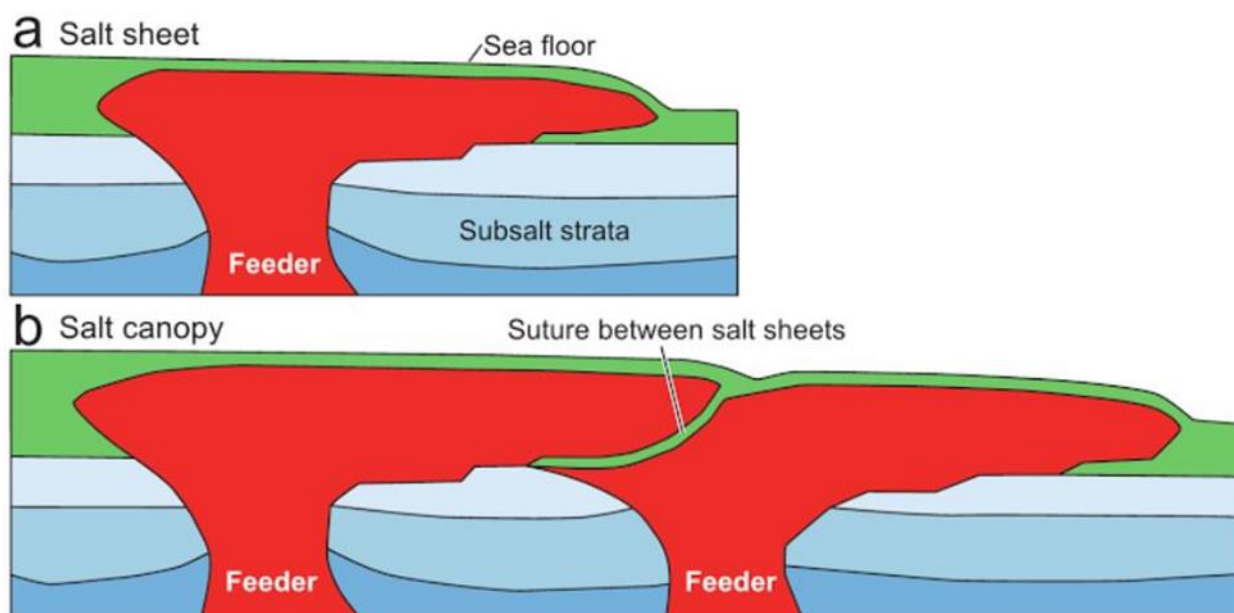
Figure 2: Concordant salt structures a) Salt sheet with only one discordant feeder b) Salt canopy, with two discordant diapiric feeders. A suture has formed at the contact between salt sheets (From Jackson and Hudec 2017).

1.4 Regional Geology of Axel Heiberg Island

The study site for this project is Axel Heiberg Island (Figure 3), where a salt canopy is hypothesized to have produced an abundance of salt diapirs. In the modern day, Axel Heiberg Island is considered a polar desert environment because potential evaporation exceeds the annual precipitation (Andersen et al. 2002). At White Glacier (79º27'N,

90º40'W) mean temperature is -15.2ºC. Winter temperatures reach below -40ºC, whereas summer months are often above zero (Andersen et al. 2002; Mueller and Pollard 2004). Annual recorded annual precipitation at White Glacier between 58-117 mm (Mueller and Pollard 2004). Geologically, Axel Heiberg is located within the Sverdrup Basin, which spans 1300 by 500 km of the northern Canadian High Arctic. The Sverdrup Basin is a 13 km thick sedimentary package deposited between the Early Carboniferous to the Paleogene (Embry 2009) and overlies the Franklinian Basin (Harrison and Jackson 2014b). Axel Heiberg Island hosts 9 km out of the 13 km of Sverdrup Basin strata, and this sedimentary package has undergone substantial deformation. During its early formation, the Sverdrup Basin was a shallow sea between the North American Craton and a northern landmass named "Crockerland". The basin was filled with sediments that were derived from Crockerland, Devonian strata, and the Canadian and Greenland Precambrian Craton (Patchett et al. 2004; Embry 2009). The Paleogene Eurekan orogeny 62 to 33 Ma led to regional folding across the Axel Heiberg and adjacent islands and into Greenland (Harrison and Jackson 2014b).

The depositional history of Axel Heiberg Island is complex. Facies include a full suite from terrestrial fluvial-deltaic to deep marine sediments, along with shallow marine evaporites and igneous intrusions (Harrison and Jackson 2014b). Modern geomorphological processes include perennial spring activity as well as mass wasting, fluvial, and periglacial processes. The Sverdrup Basin underwent four main tectonic intervals between the Early Carboniferous to the Paleogene. In the first stage, the Sverdrup Basin experienced rifting between the early Carboniferous through the mid-Permian, depositing redbeds followed by the precipitation of the submarine Otto Fiord Formation evaporites interbedded with limestones. The Otto Fiord Formation is the source of diapirs on Axel Heiberg Island. The final stages of rifting created accommodation space for the evaporites to be buried under sequences of mudstone and limestone. Post-rifting, the Sverdrup Basin passively subsided. The subsidence allowed for sediment progradation, accumulating over 5000 m of siliciclastic and carbonate material through the Late Permian to Early Jurassic (Harrison and Jackson 2014b). Rifting occurred from the Middle Jurassic into the Early Cretaceous, splitting apart Crockerland (Embry 2009). Petroleum-rich rock was deposited in the Late Jurassic, and
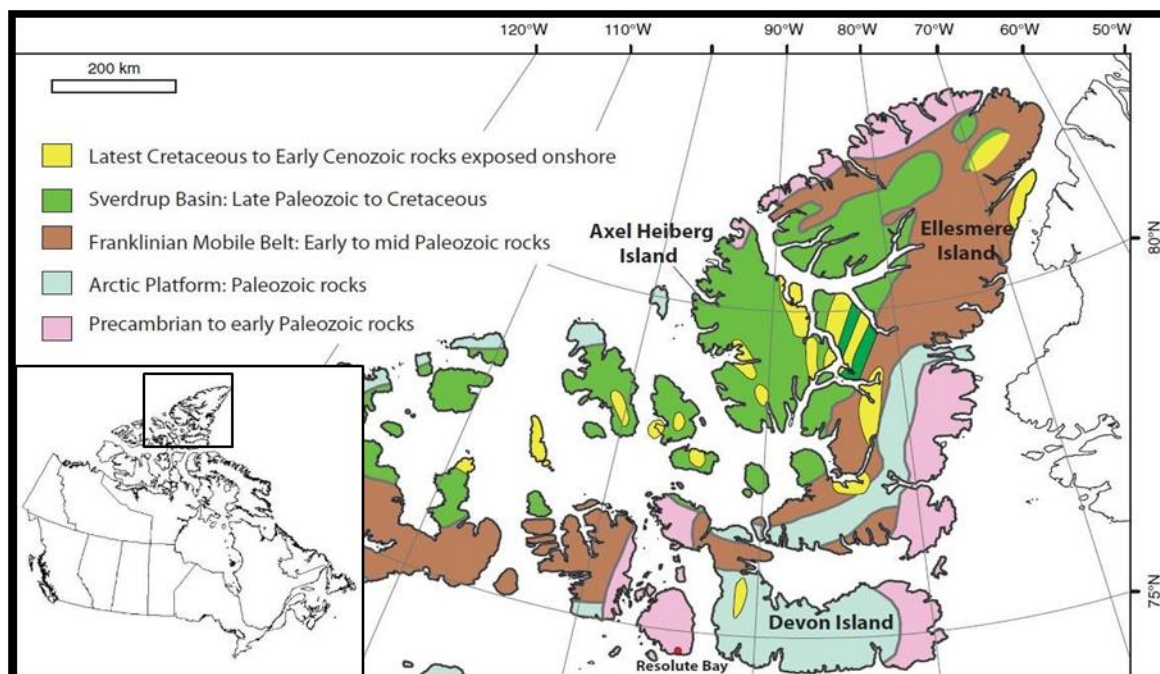
Figure 3: The position of Axel Heiberg Island in the Canadian Archipelago. The green unit represents the extent of the Sverdrup Basin, which accumulated through the Late Paleozoic to the Cretaceous (Modified after Williamson et al. 2014).

some hydrothermal alteration resulted in iron sulphide ore mineralization creating sources of economic interest in the Sverdrup Basin (Harrison and Jackson 2014b).

The Sverdrup Basin contains approximately 100 diapirs (Figure 4), of which 60 are exposed at surface. Of these, Axel Heiberg Island hosts 46 exposed diapirs (Embry 1993). In consequence, Axel Heiberg Island contains one of the highest concentrations of salt diapirs in the world, second only to the Zagros Mountains of Iran. The diapirs on the island are composed of anhydrite, which is weathering to gypsum, and contain interbeds of brecciated carbonates (Jackson and Harrison 2006). Only Stolz diapir is known to contain exposed halite, although groundwater is hypothesized to flow through subsurface halite near Colour and Wolf diapirs based on the geochemistry of nearby perennial springs (Battler et al. 2013; Harrison and Jackson 2014a). The Otto Fiord Formation is ≤410 m thick and was deposited during the Late Mississippian to Late Pennsylvanian. The interstratified anhydrite and limestone precipitated in a submarine environment.
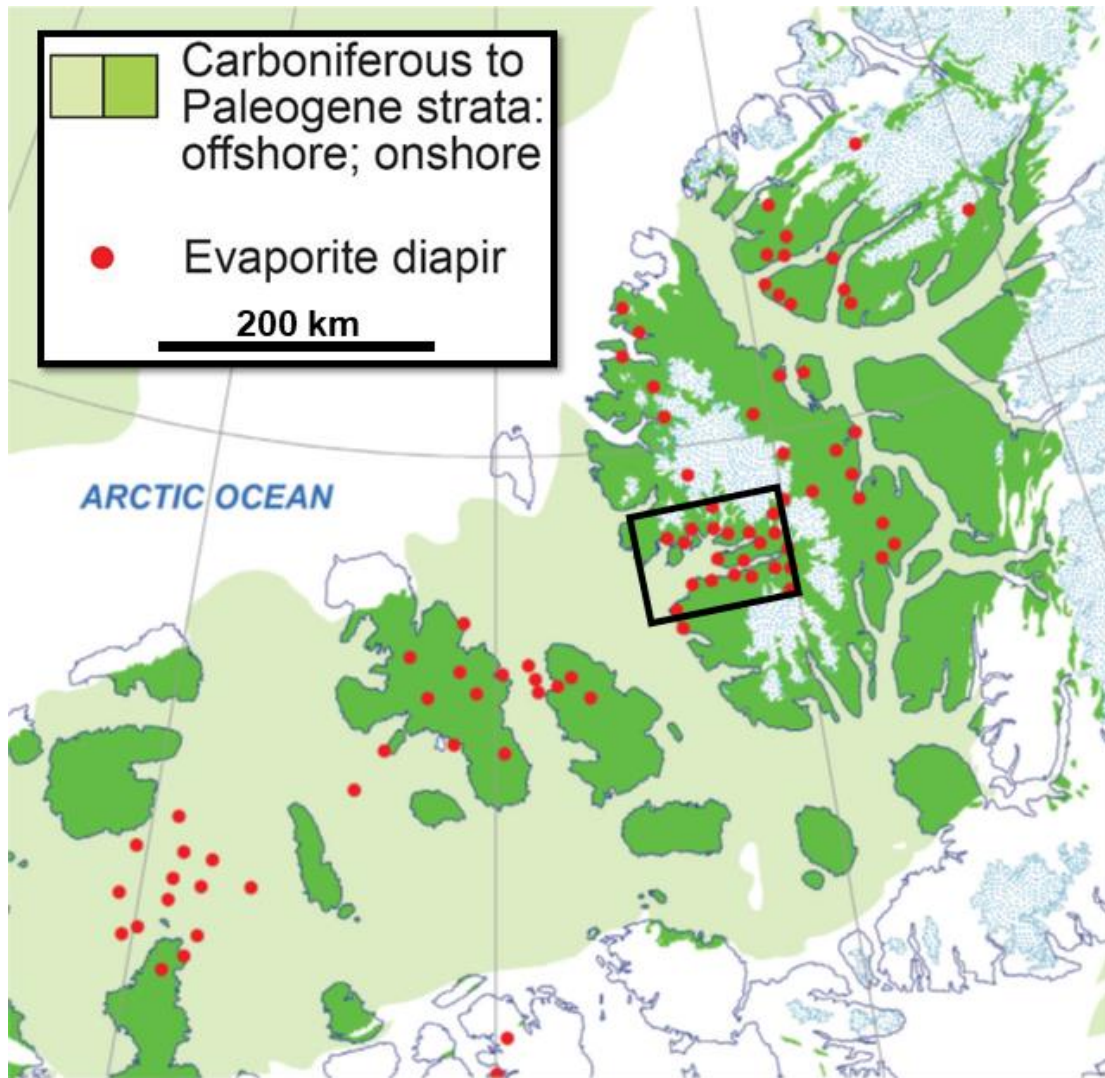
Figure 4: Locations of mapped salt diapirs in the Sverdrup Basin, Canada. Black box outlines the wall-and-basin structure (WABS) region on Axel Heiberg Island, NU (Modified after Harrison and Jackson 2014a).

The diapirs on Axel Heiberg Island were only recently mapped in detail. Through field traverses across the Expedition and Strand Fjord regions, Jackson and Harrison (2006) found a 60 km wide area of deformation where locally folded strata do not align with the regional deformation. This area, termed a wall-and-basin structure (WABS), contains a higher abundance of diapirs (Figure 4) than the rest of the island. They hypothesize that the WABS represents a salt canopy, where rising diapirs came together, joining to form a stratiform sheet and disrupting the surficial strata. This second generation of diapirism
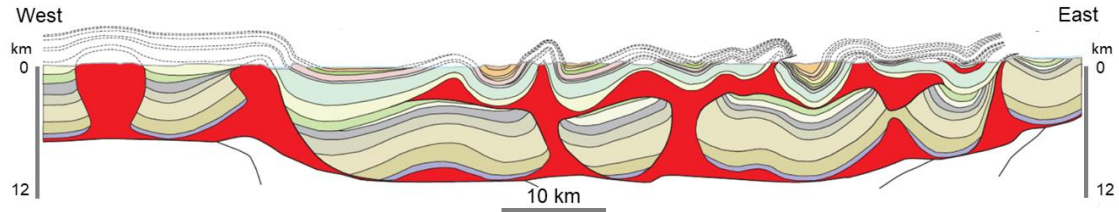
Figure 5: Salt canopy in cross-section of Axel Heiberg Island wall-and-basin structure. Otto Fjord formation (salt) is shown in red (Modified from Harrison and Jackson 2014a).

has led to the high concentration of diapirs exposed at surface (Jackson and Harrison 2006; Harrison and Jackson 2014a). The tectonic events that have deformed the Sverdrup Basin have contributed to the rise of the diapirs into the overlying strata. The basin was rifted until the mid-Permian, and thermally subsided between the Late Permian though the Early Jurassic. The older diapirs began their ascent during the Late Triassic and were greatly accelerated by the onset of Arctic Ocean seafloor spreading during the Cretaceous. This rifting thinned the crust and produced extensional faults that provided planes of weakness for diapir ascent (Jackson and Harrison 2006; Harrison and Jackson 2014a).

1.5 Aims and Objectives

Axel Heiberg Island is of economic interest for resource exploration. As mentioned previously, the Late Jurassic rocks of the Sverdrup Basin are known to contain large petroleum resources. Salt diapirs frequently help to form structural traps for petroleum reservoirs (as well as lead and zinc orebodies), making diapirs a key first target for resource exploration (Rouvier 1985; MacGregor 1993; Jackson and Harrison 2006). However, the Island's remoteness makes traditional field mapping difficult and expensive. Furthermore, the Canadian Arctic is virtually inaccessible during winter seasons, being dark for half the year and obscured by extensive snow coverage. To advance exploration in inaccessible regions, industries and agencies are turning to remote predictive mapping methods. This is the first study to characterize the polarimetric SAR properties of salt diapirs for remote predictive mapping. SAR not seasonally constrained

by daylight hours or cloud coverage, making it a useful tool in the Arctic. Unlike passive remote sensing methods (e.g. spectroscopy, optical imagery) radar transmits its own signal, meaning it can be used during Arctic winters and on cloudy days. Radar is sensitive to soil moisture and vegetation, but much of the Arctic is a dry and barren polar desert. Subsequently, the Canadian High Arctic is an ideal location in which to explore the limits and capabilities of SAR for geological mapping (McHone et al. 2002). Seven out of eight RADARSAT-2 images used in this study are acquired over the WABS region. Three out of five diapirs (Colour, Wolf, and Strand diapirs) visited during field investigation in July 2017 are within the imaged WABS area. Stolz and Whitsunday Bay diapirs are east of the WABS zone but were also imaged and visited during the field season. Although Stolz diapir is the only dome with exposed halite, there are halite salts in the perennial springs and their deposits near Colour, Wolf, Expedition, and Junction diapirs. Of these, Stolz, Colour, and Wolf diapirs were visited in this study to compare remote sensing data with field observations.

The thesis is divided into five main chapters, including this one. Chapter 2 reviews the methodology used in processing the spectral and radar datasets, as well as the ground truthing during the 2017 field season. Chapter 3 show the results of the study, including the final processed images and the radar properties for diapiric and secondary salts. Chapter 3 also quantitatively describes the salt diapirs visited in the field at the outcrop and hand sample scale and presents the XRD lab results of samples acquired in the field. Chapter 4 discusses the benefits of using multiple remote sensing datasets to make geologic interpretations, including VNIR, TIR and shortwave infrared (SWIR) spectroscopy and polarimetric SAR. Additionally, the radar backscatter responses at C-Band (5.6 cm wavelength) and L-Band (23 cm wavelength) over the salt deposits are compared. Chapter 4 also discusses the implications of secondary salt remobilization for periglacial terrain formation, as well as the discussion of salt minerals and potential diapirism on other planetary bodies. Chapter 5 provides concluding remarks.

Chapter 2

2 Methods

One of the key aims of this study is to demonstrate methods of combining multiple datasets for remote predictive geological mapping. We have acquired visible and near-infrared (VNIR, 0.4-1.4 µm), shortwave infrared (SWIR, 0.9-2.5 µm), thermal infrared (TIR, 8-14 µm), and radar imagery (5.6 and 23 cm), along with topography data of our study region. VNIR, SWIR, and TIR data are used to highlight gypsum and anhydrite spectral signatures, and the TIR spectral data are used to map the locations of the signatures produced by these salt deposits. The radar data are used to characterize the surface roughness properties of salt diapirs and secondary salt deposits. Digital Elevation Models (DEMs) are used for terrain correcting radar images as well as interpreting the geomorphological nature of salt exposures (i.e., diapiric or secondary, based on topography). Finally, an important part of this study is ground-truthing. After visiting Axel Heiberg Island, we are better able to evaluate and understand the remote sensing data. In the field, we observed how the secondary salts are precipitating and are otherwise being mechanically transported. We also compared the surface roughness of salt diapirs as observed in the field to the signatures seen in the SAR data. Lastly, we sampled the salt minerals for lab XRD analysis to compare their mineralogical compositions against interpretations made from orbital spectroscopy.

2.1 Visible, Near Infrared, and Thermal Infrared Spectroscopy

The satellite spectroscopy methods applied in this study are passive forms of remote sensing. Like a non-flash optical camera, neither the Optical Land Imager (OLI) on Landsat-8, nor the Advanced Spaceborne Thermal Emission and Reflection Radiometer (ASTER) instrument on the Terra satellite provide their own signal. However, unlike optical imagery, they can detect radiation extending beyond the visible range on the electromagnetic spectrum. When sunlight hits the Earth's surface, three processes happen: some radiation is reflected, some is absorbed, and some is transmitted (Campbell and Wynne 2011). Reflected radiation bounces off the surface and its intensity at

different wavelengths can be recorded by spectral sensors. Radiation that is transmitted penetrates the surface; the depth of penetration is a function of wavelength, with longer wavelengths penetrating further into the subsurface. As the light penetrates the surface, some of it gets absorbed. Absorbed radiation interacts with the surface at an atomic level, and some of this energy is reemitted. The wavelength of the reemitted light is dependent on the blackbody temperature of the surface; rocks on Earth typically reemit at infrared wavelengths.

Spectral signatures for a given material show the intensity of reflected radiation over a range of wavelengths (Figure 6). Materials have absorption bands at wavelengths where radiation is absorbed by an atom or molecule, thus resulting in lower reflection intensity. Molecules possess up to four types of energy: translational, rotational, vibrational and electronic. Of these, the vibrational and electronic energy states can be affected by electromagnetic radiation from the visible to thermal infrared (TIR) range of the electromagnetic spectrum (Elachi and van Zyl 2006; Gupta 2017). The materials reflect different wavelengths at different intensities, and these unique signatures can help in identifying surface materials.

Changes in electronic energy states are most noticeable in materials containing transition metals. Transition metals include iron (both ferrous and ferric ionization states), copper, manganese, nickel, and chromium. Ions of these metals are particularly sensitive to radiation in the visible and near infrared (VNIR) range of the electromagnetic spectrum. An example of this phenomenon are iron oxide minerals. Hematite (Fe_2O_3) is often red because it exhibits strong absorption at visible wavelengths shorter than 520 nm, with a steep absorption edge up to 0.7 nm (Lane et al. 1999; Gupta 2017). Because the VNIR range is predominantly absorbed by metal-bearing compounds, VNIR spectroscopy is particularly useful for targeting metal-bearing mineral assemblages like mafic to ultramafic rocks and sulphide deposits. Conversely, carbonates, sulphates, and felsic mineral assemblages typically do not exhibit strong absorption features in the VNIR range.
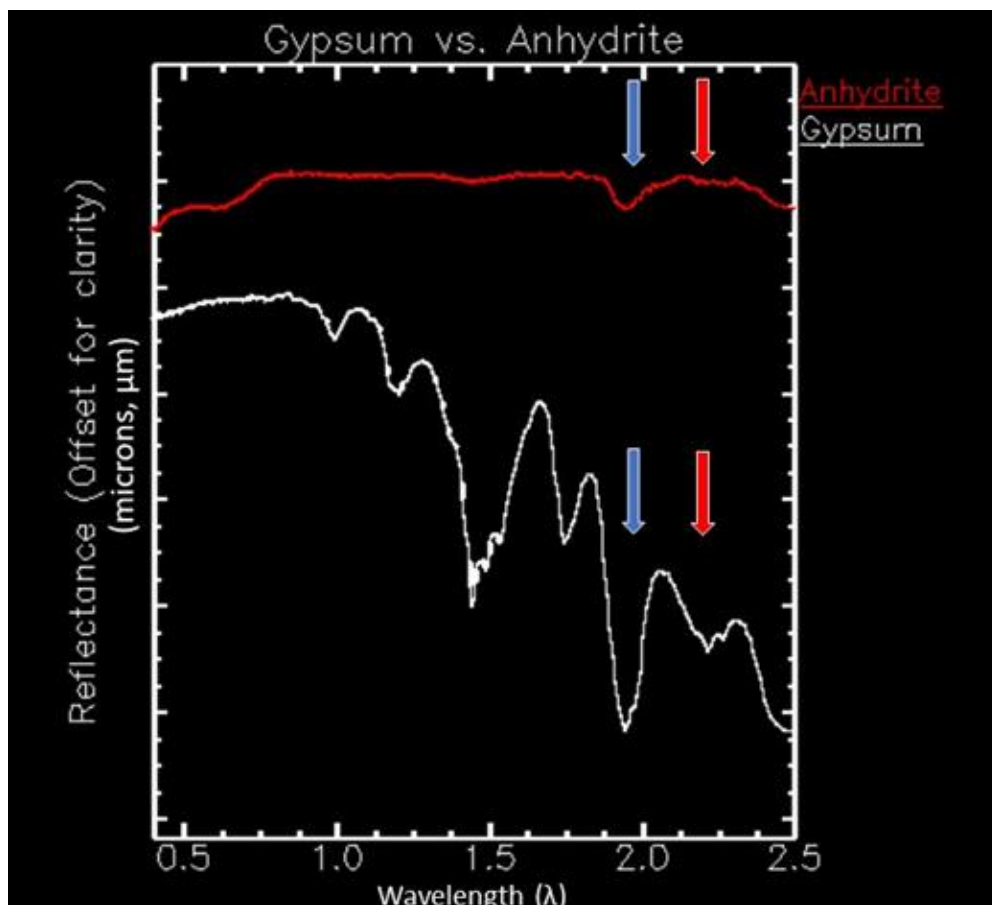
Figure 6: Absorption spectra of anhydrite and gypsum. Blue arrows highlight an absorption feature from water at 1.9 μm (stronger in gypsum, a more hydrated mineral). Red arrows show overtone features at 2.2 μm, again more prominent in gypsum. Figure modified from the ENVI spectral library

Changes in vibrational energy states, on the other hand, are more noticeable in silicates, carbonates, and sulphate mineral assemblages. These energy state changes predominantly occur in response to SWIR through TIR radiation, producing overtone features. Carbonates, hydroxyl-bearing minerals (e.g., phyllosilicates like micas and clays), and hydrated minerals (i.e. minerals with water trapped in their crystal lattice, like gypsum) show strong absorption features under SWIR radiation (Elachi and van Zyl 2006). Carbonates, hydroxyl-groups, and sulphates, as well as silicates and oxides, are sensitive to TIR radiation and show strong absorption bands in the TIR range (Gupta 2017). Because TIR remote sensing is sensitive to felsic-silicate minerals, some of the most

abundant minerals in the Earth's crust, it is very useful in remote predictive geological mapping.

However, because individual minerals can contain multiple constituents, their spectral signatures can be quite complex. Hornblende $(Ca,Na)_{2-3}(Mg,Fe,Al)_5(Al,Si)_8O_{22}(OH,F)_2)$, as an example, will show absorption bands from its iron, hydroxyl ions, and silicate components. Impurities within a crystal structure (e.g. trapped metal-ions in a silicate) can produce additional absorption features, often rendering spectral remote sensing data difficult to interpret. Furthermore, because rocks are often collections of mineral assemblages, and often contain interbeds of other rock types, interpreting their spectral signatures becomes increasingly complicated. Finally, surface weathering, soil coverage, vegetation, ice and snow can also obscure the spectral signature of underlying bedrock. It is emphasized that spectroscopic data is interpretative rather than definitive.

In this study, composite multispectral imagery from Landsat 8 and ASTER are used to identify gypsum and anhydrite-rich regions indicative of salt deposits on Axel Heiberg Island. Six archival Landsat-8 tiles were acquired from August of 2014 and 2015. The following bands were mosaiced in the Environment for Visualizing Images (ENVI) software using the seamless mosaic tool: B2 (0.45-0.51µm, visible - Blue), B4 (0.64-0.67µm, visible - Red), B5 (0.85-0.88µm, NIR), B6 (1.57-1.65 µm, SWIR), and B7 (2.11-2.29 µm, SWIR). The mosaiced bands are stacked together using the Layer Stacking tool in ENVI. These are used to produce a colour composite band ratio image (R: B6/B7, G: B6/B5, B: B4/B2) (Shaposhnikova et al. 2016). Because gypsum is a water-bearing mineral, it is expected to show an absorption band at ~1.9 µm (Elachi and van Zyl 2006). Subsequently, the B6/B5 ratio (1.57-1.65µm /0.85-0.88) is expected to be low over areas of abundant salt concentration due to absorption. Placing the B6/B5 ratio in the green channel of the band strength map highlights the sulphate minerals in bright magenta because the red and blue channels represent bands that are observed at higher intensities (Figure 7, Figure 8). The band ratios were produced using the Band Ratio tool in ENVI. This absorption feature is also highlighted in a darker pink in an ASTER SWIR composite image (R: B4 (1.656 µm) G: B5 (2.167 µm) B: B6 (2.209 µm) (Figure 9)).
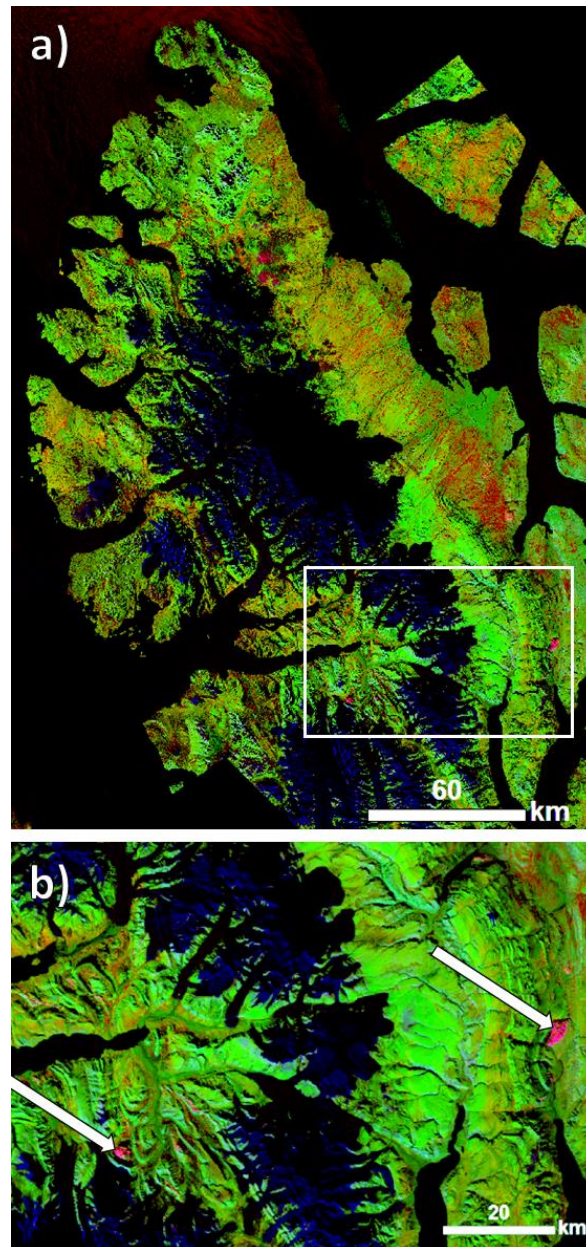
Figure 7: a) Landsat-8 band ratio image over Axel Heiberg Island (R: B6/B7, G: B6/B5, B: B4/B2). A min-max stretch is applied, setting the minimum value to 1 to filter interference from water and ice reflection. The B6/B5 (1.57-1.65μm /0.85-0.88μm) ratio in the green channel is expected to be low over areas of gypsum because of a water absorption feature at ~1.9 μm, highlighting sulphate minerals in magenta. The ice sheet is represented in blue. The location of Figure 7b is denoted by the white rectangle. b) Close up of Landsat-8 composite images around key study site, outlined by white rectangle in 7a. White arrows denote prominent diapirs.
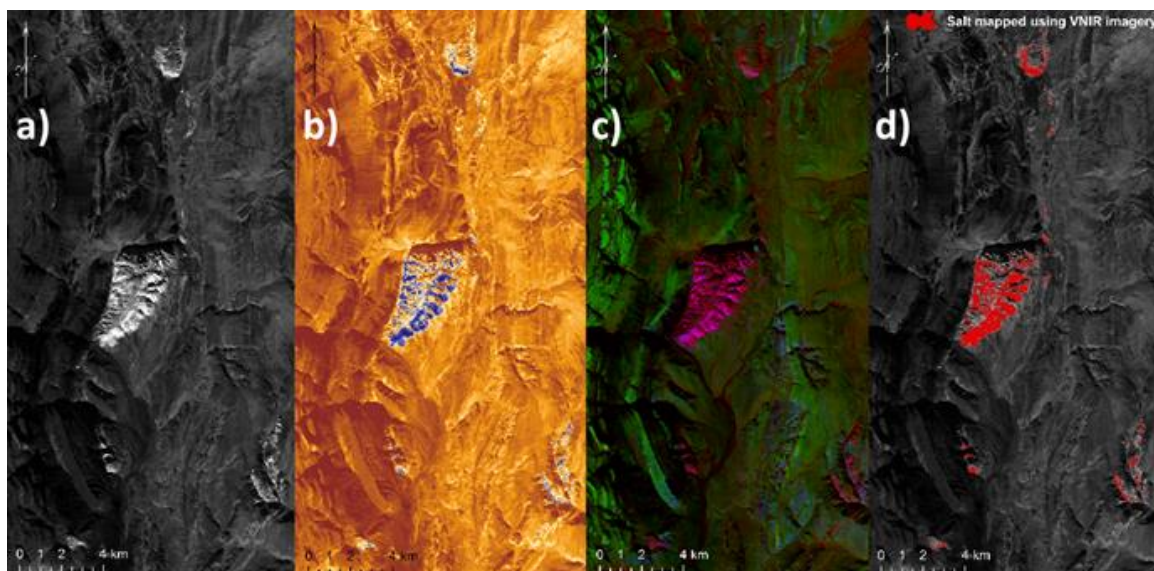
Figure 8: VNIR Salt Mapping over Whitsunday Bay Diapir, eastern Axel Heiberg Island. a) Landsat-8 greyscale and b) colour composite (R: B12 (8.925-9.275µm), G: B11 (8.475-8.825µm), B:13 (10.25-10.95µm)). Salt appears white in the greyscale image, blue in colour composite. c) Landsat-8 colour composite (R: B6/B7, G: B6/B5 (0.85-0.88 µm), B: B4(0.64-0.67 µm)/B2(0.45-0.51 µm)). The absorption feature at ~2.2 µm in gypsum and anhydrite leads to a high B6/B7 ratio over the salt exposure, highlighting the salt in magenta. d) Example of manually mapped salt (red) using a combination of a-c VNIR composite images.

Gypsum and anhydrite also have a deep absorption feature in the TIR spectrum at ~8.6 µm. Thirteen archival ASTER TIR images from 2001-2005 were acquired over Axel Heiberg Island. These have also been mosaiced in ENVI. Combining the ASTER TIR bands B11 (8.634 µm), B12 (9.075 µm), B13 (10.657µm) to produce an RGB colour composite image (R: B12, G:11, B:13) in ENVI similarly highlights the sulphate minerals in a maroon colour, as again the wavelength in the green channel is absorbed more than the other wavelengths (Figure 10).

The TIR composite image shown in Figure 10 is used to map areas with the highest gypsum and anhydrite signatures. The mapping was performed by manually tracing out each area in ArcMap. Previous field maps (Harrison et al. 2015) and topographic and morphological data from the CDEM are used to differentiate between salts that are
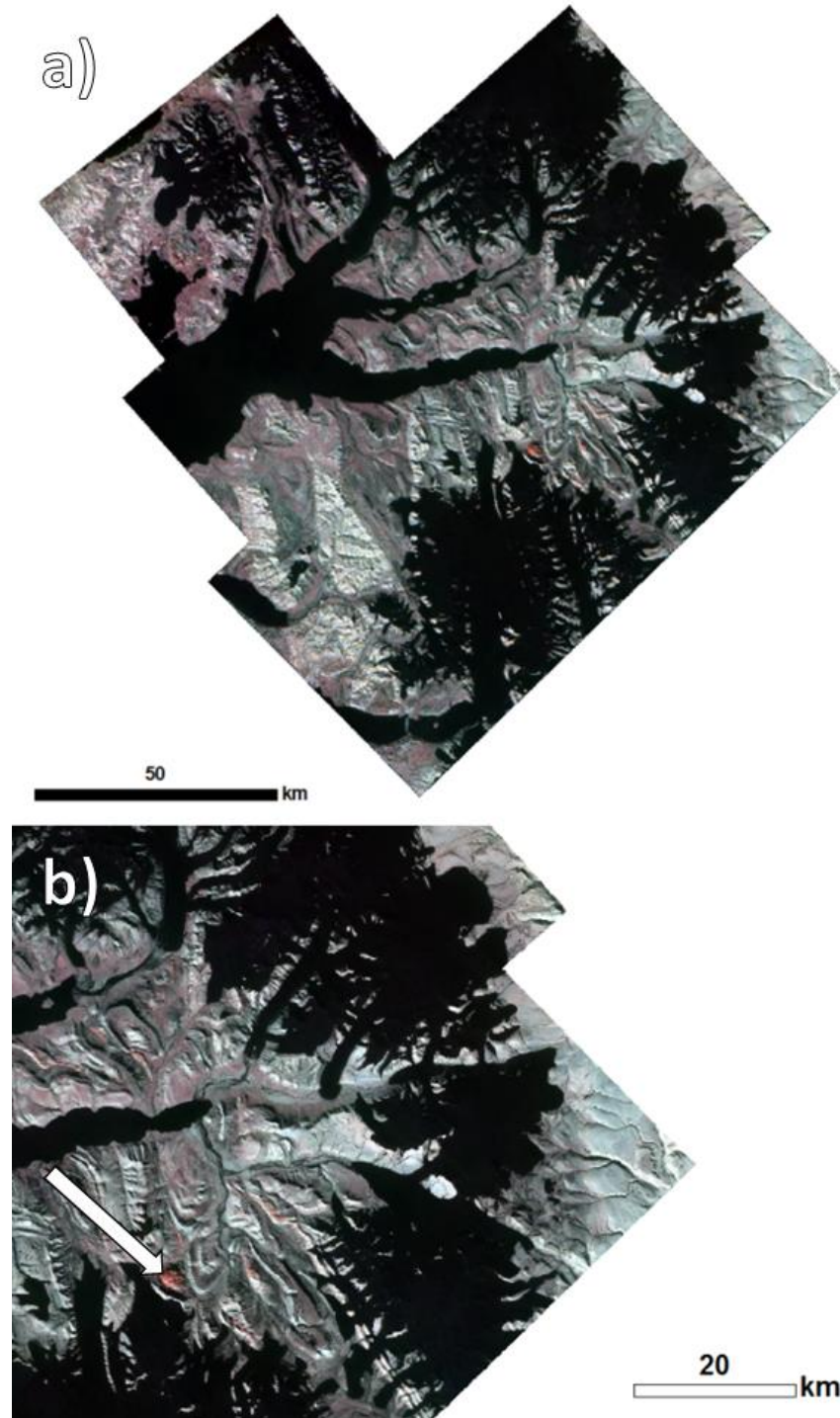
Figure 9: a) ASTER SWIR composite image (R: B4 (1.656 µm) G: B5 (2.167 µm) B: B6 (2.209)), highlighting the sulphate minerals in a darker pink than surrounding rock units. A 0.5 percent clip stretch has been applied. b) Close up SWIR image of area denoted by white box in 7a. The white arrow denotes a prominent diapir.
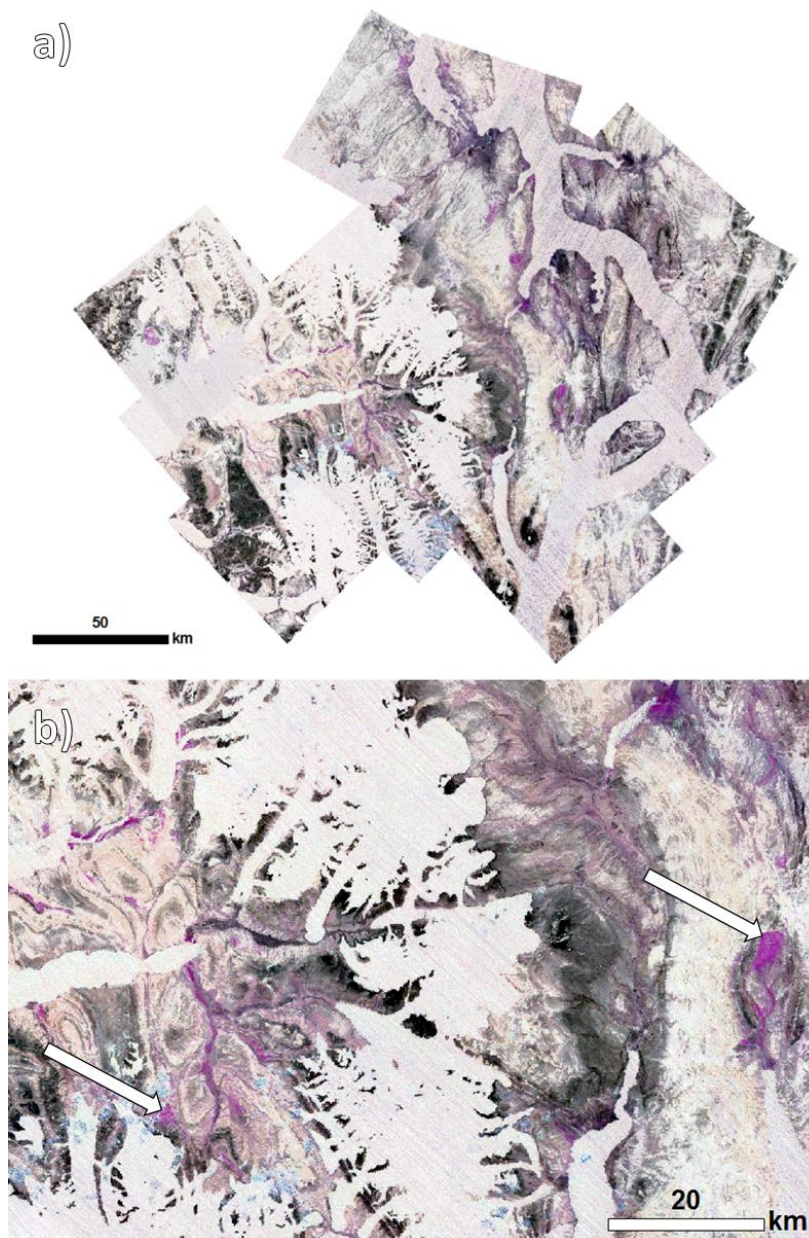
Figure 10: a) ASTER TIR composite image over Axel Heiberg Island (R: B12 (9.075 µm), G:11 (8.634 µm), B:13 (10.657 µm)). A min-max stretch is applied, setting the minimum value to 1, filtering interference from water and ice reflection. Gypsum and anhydrite have a deep absorption feature at ~8.6 µm, implying that sulphate-rich regions will have low values in the green channel, highlighting the sulphate minerals in dark purple. Dark purple signatures are strong not only over salt domes, but also their adjacent gullies, hillslopes, and streambeds b) Close up image of area outlined in 7a. Prominent diapirs are denoted by white arrows.

suspected to be diapiric in nature, versus secondary remobilized salts. The radar images are then used to characterize the CPR radar signatures of areas mapped as salt diapirs against the other secondary salts and the surrounding rocks, providing us with a standard that can be used for mapping new diapirs. Using the zonal statistics tool in ArcMap we determined the CPR values for each area mapped as a salt. These are then averaged for each radar dataset as both "average per diapir" (the average of all diapir mean values) and as "average per pixel" (the mean pixel value for all pixels mapped as salt diapirs). This process is repeated for salt diapirs and secondary salt deposits separately.

2.2 Polarimetric Radar

SAR is an active form of remote sensing that involves transmitting a radio signal to the surface of the Earth and later receiving its echo. This produces a radar image, which can be useful for characterizing surface roughness. The roughness of a surface, as well as its dielectric properties and large-scale topography, controls the intensity of the radio signal reflected towards the satellite antenna (Neish and Carter 2014). Differences in surface roughness can be attributed to variations in rock composition and erosion, enabling SAR to be a useful tool in remote mapping.

Polarimetric radar data provides more detailed information about the surface properties. The SAR beams can be transmitted circularly polarized, in either a left or right polarization "sense", or the circular polarizations can be constructed from horizontal and vertical linear polarization data. After reflecting off surfaces, polarized waves may be received in the "same sense circular" (SC = received signals share polarization direction as transmitted signal) or the "opposite sense circular" (OC = received signals have opposing direction as transmitted signal). The circular polarization ratio (CPR) is the ratio of SC/OC and can constrain surface roughness and morphology (Figure 11).

Rough surfaces will have CPR values between ~0.5 to 1 as the multiple bounces randomizes the polarization of the scattered beams (Neish and Carter 2014). Smooth surfaces have low CPR values, typically below 0.5, as the reflected beams from a single bounce flip polarization sense once, while reflecting most of the signal away from the antenna. If the beam bounces off a second surface, like a large boulder or crack, the
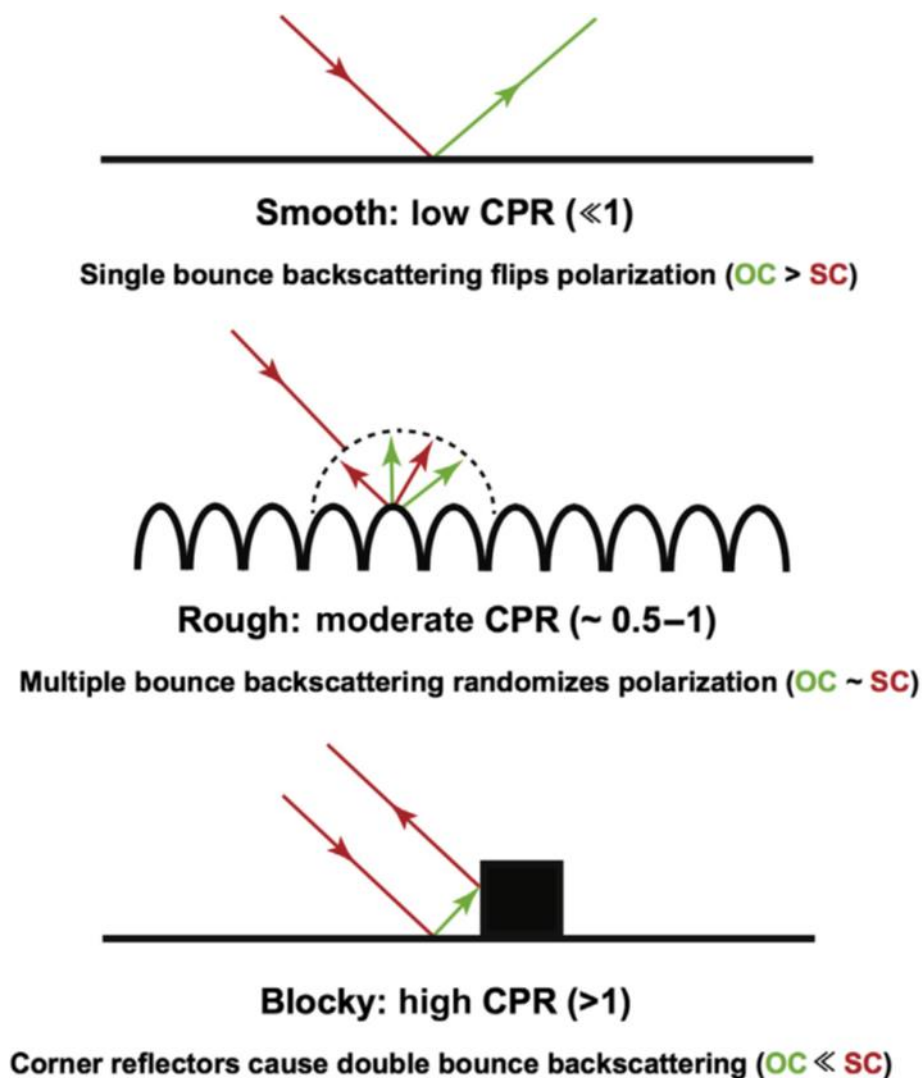
Figure 11: Diagram showing the effects of surface roughness on circular polarization ratio. Smooth surfaces reflect radar beams once, in the opposite polarization sense as the transmitted beam, resulting in very low CPR values. Rough surfaces variably scatter incident beams in a mix of opposite and same sense polarized returns – the rougher the surface, the higher the CPR value. Blocky surfaces cause double-bounce scattering, which flips the polarization sense twice, resulting in a high same-sense radar return (Figure from Neish and Carter 2014).

polarization sense flips a second time. Surfaces dominated by large blocks or cracks cause double bounce scattering, because the returned signals frequently bounce twice, and flip polarization sense twice. Because blocky surfaces return predominantly same-

sense signals they are associated with high CPR values (CPR > 1) (Campbell 2012, Neish and Carter 2014). Ice has low microwave loss and can produce CPR values up to about 2. As cracks and voids within the ice scatter the radar, the signals propagating through the ice add constructively, producing high return of same sense signals (Campbell 2012).

Surface roughness is controlled by emplacement properties (like the textural differences between pahoehoe and a'a lavas as basalt flows and cools – see Neish et al. 2017) and/or surface weathering characteristics (Choe 2017). Rock salts are expected to produce strong signatures in SAR because the low hardness and high solubility of salt lends them to be readily eroded, forming a rough surface. Halite salt diapirs have also been shown to erode into grooved morphologies called *rillenkarren*, which are dissolution features classically seen in limestone (Figure 12) (Stenson and Ford 1993; Fiol et al. 1996). Subsequently, salt exposures are hypothesized to appear rougher at the surface than the surrounding rock, enabling them to be identified and mapped remotely using radar techniques.
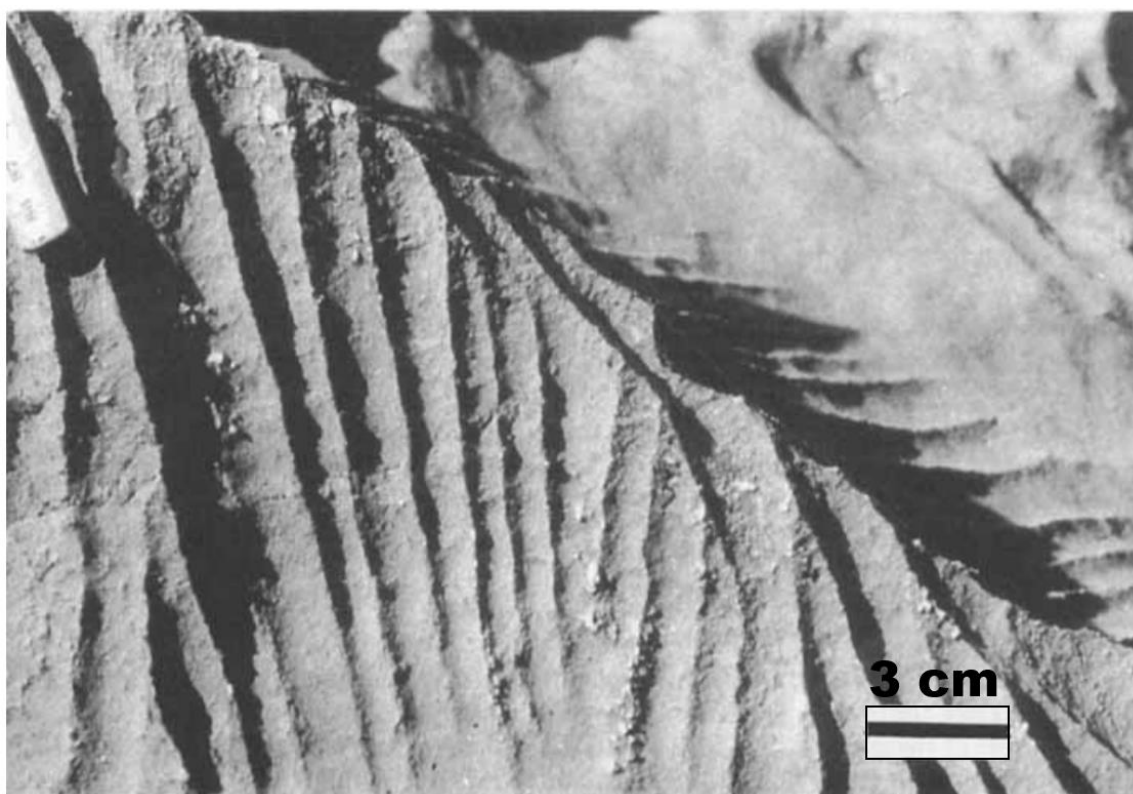
Figure 12: Typical rillenkarren found in karstic limestone landforms in the western Mediterranean (From Fiol et al. 1996).

Eight new fully polarimetric RADARSAT-2 images have been acquired in 2016 and 2017 over the study site in Axel Heiberg Island, Nunavut (

Figure 14). RADARSAT-2 uses C-Band SAR, with a wavelength of 5.6 cm. The images were obtained through the Canadian Space Agency's Science and Operational Applications Research (SOAR) grant program. The raw images are acquired in single look complex (SLC) format, with data describing the intensity of radar beams transmitted and received in the horizontal and vertical orientations (Thompson and McLeod 2004). These data produce a 2x2 quad polarimetric scattering matrix, [S] (Equation 3). The scattering matrix contains four complex components, which represent the intensity of the four polarimetric radar channels. These represent each permutation of radar signals transmitted and received in horizontal and vertical polarizations.

$$S = \begin{bmatrix} S_{hh} & S_{hv} \\ S_{vh} & S_{vv} \end{bmatrix} \qquad (Equation\ 3)$$

Each image has been processed individually to derive circular polarization ratio (CPR) products. To produce the CPR images, the free software PolSar-Pro was used to extract the Covariance matrix (C3) components for each image. Within the program, PolSAR-Pro applies the Lexicographic target vector (Ω) (Equation 4) to the scattering matrix.

$$\Omega = \begin{bmatrix} S_{hh} & \sqrt{2}S_{hv} & S_{vv} \end{bmatrix}^T \qquad (Equation\ 4)$$

This produces the 3x3 covariance matrix (Equation 5). In statistics, a covariance matrix characterizes the elements of a random vector. The C3 matrix is a 3x3 matrix that represents the complete, symmetrized covariance matrix for fully polarimetric data. It represents the total scattering from the sum of the single bounce, double bounce, and volumetric scattering matrices (Freeman and Durden 1998). Thus, covariance matrices represent the most complete way of describing the scattering properties of a reflecting surface for polarized SAR data.

$$[C_3] = \langle \Omega \cdot \Omega^{*T} \rangle \begin{bmatrix} \langle |S_{HH}|^2 \rangle & \sqrt{2}\langle S_{HH}S_{HV}^* \rangle & \langle S_{HH}S_{VV}^* \rangle \\ \sqrt{2}\langle S_{HV}S_{HH}^* \rangle & 2\langle |S_{HV}|^2 \rangle & \sqrt{2}\langle S_{HV}S_{VV}^* \rangle \\ \langle S_{VV}S_{HH}^* \rangle & \sqrt{2}\langle S_{VV}S_{HV}^* \rangle & \langle |S_{VV}|^2 \rangle \end{bmatrix} \qquad (Equation\ 5)$$

Once the covariance matrix has been extracted from SLC components, an elliptical basis transformation is applied in PolSAR-Pro to extract the data in a circular basis. The program achieves this by applying the polarimetric basis change matrix (U) (Equation 6) to the scattering matrix (Equation 7). In these equations, α is the absolute phase term, ϕ is the ellipse orientation angle, and τ is the ellipticity angle. The relationship between these variables can be illustrated by the polarization ellipse (Figure 13).

The absolute phase term (α) depends on the distance from the target surface and the radar sensor but does not affect the returned backscatter intensity. In contrast, ϕ and τ both affect backscatter intensity, with maximum and minimum backscatter occurring at different angles depending on the orientation of the surface and the presence dihedral structures (Choe 2017).

$$[U] = [U(\phi)][U(\tau)][U(\alpha)] = \begin{bmatrix} cos\phi & -sin\phi \\ sin\phi & cos\phi \end{bmatrix} \begin{bmatrix} \cos\tau & i\sin\tau \\ i\sin\tau & \cos\tau \end{bmatrix} \begin{bmatrix} e^{+i\alpha} & 0 \\ 0 & e^{-\alpha} \end{bmatrix} \quad (Equation\ 6)$$

$$[C_3{}'] = [U]^T[C_3][U] \quad\quad (Equation\ 7)$$

This produces the circularly polarized [C_3] matrix (Equation 8).

$$[C_3] = \begin{bmatrix} C_{11} & C_{12} & C_{13} \\ C_{12}^* & C_{22} & C_{23} \\ C_{13}^* & C_{23}^* & C_{33} \end{bmatrix} \quad\quad (Equation\ 8)$$

Three of the matrix elements are real, three are complex numbers with both real and imaginary components, and three are their complex conjugates. The conjugate components are denoted by * in Equation 8 (Boerner et al. 1992).

SLC images have the highest azimuth spatial resolution, but also the most speckle noise. Speckle is the byproduct of SAR having finite resolution, as surfaces are generally rough at scales smaller than the SAR wavelength, which produces multiple distributions in radar return at the pixel level. When SAR images are processed, these variations are coherently added, adding constructively or destructively producing extremely bright or dark pixels (Franceschetti and Lanari 1999). SLC pixels also generally have different
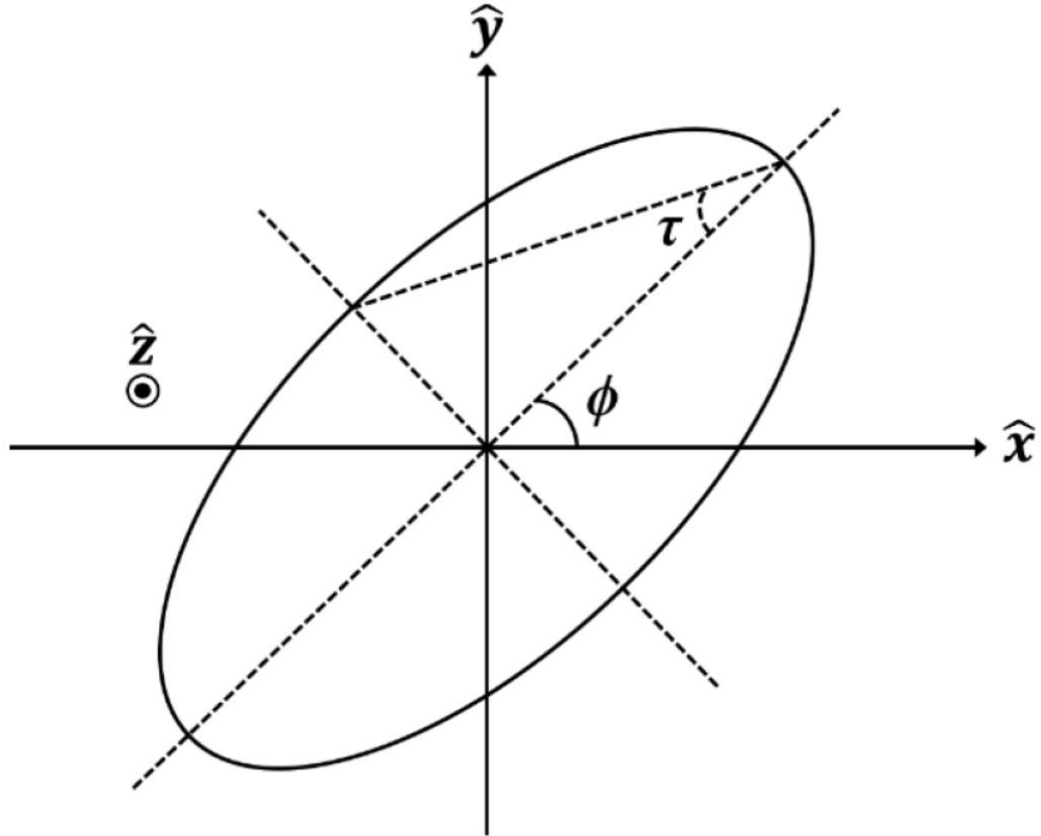
Figure 13: The polarization ellipse visually represents the orientations of circularly polarized wave propagation. The axes, $\hat{x}$, $\hat{y}$, and $\hat{z}$, show the axes of electromagnetic wave propagation plane. ϕ represents the ellipse orientation angle with respect to the $\hat{x}$ axis. τ represents the ellipse orientation angle (From Choe 2017, modified after Lee and Pottier 2009).

range and azimuth resolutions, producing rectangular pixels. The Sentinel Application Platform (SNAP) was used to multilook the C_{11} and C_{22} matrix components, which are needed for calculating the CPR (Equation 9).

$$CPR = \frac{2C_{11}}{C_{22}} \qquad (Equation\ 9)$$

Multilooking is a procedure that reduces speckle noise in radar images at the expense of lowering their spatial resolution. To balance noise reduction and image resolution, there are 5-6 range looks depending on the image. The number of azimuth looks depends on
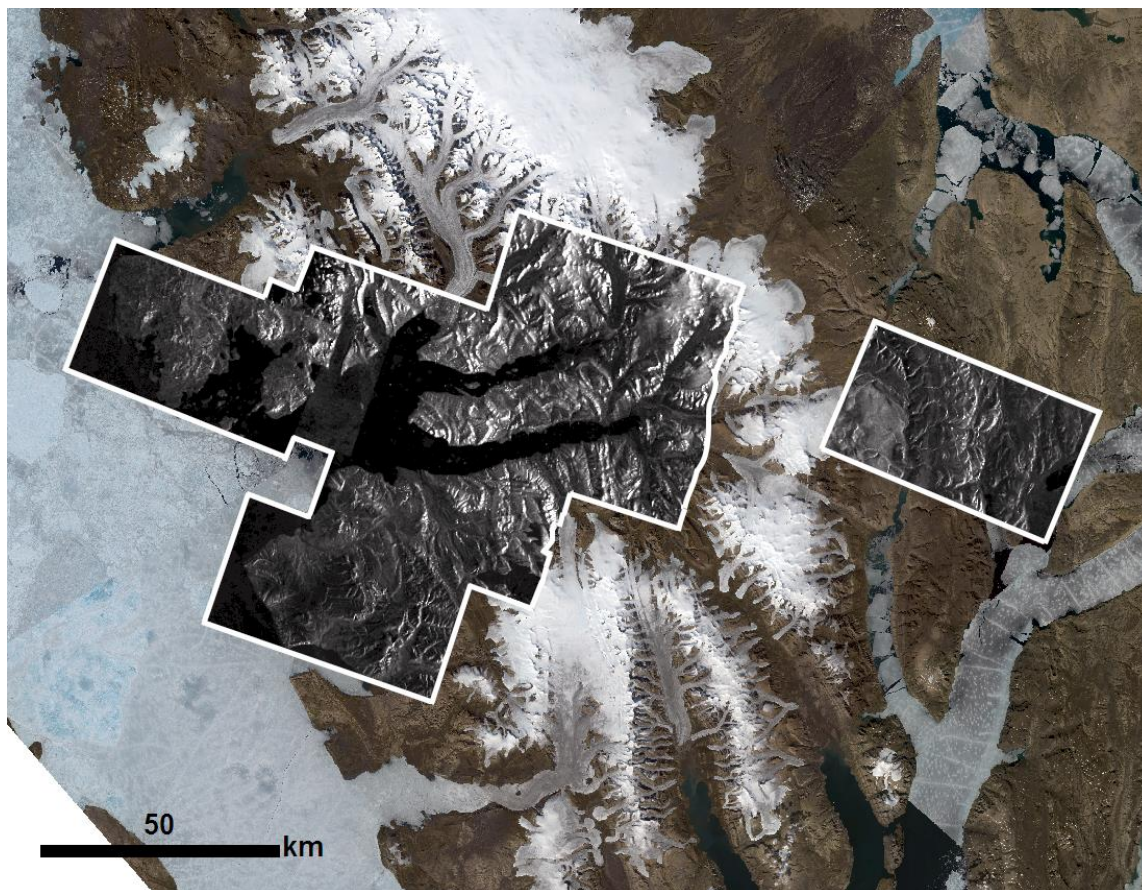
Figure 14: Mosaic of new (2016-2017) RADARSAT-2 HH intensity images over Landsat-8 true colour composite. HH images show intensity of backscatter from radar beams transmitted and received in the horizontal polarization. RADARSAT-2 uses C-Band SAR (λ = 5.6 cm). Surfaces rough at the 5.6 cm scale generally show greater backscatter than smoother surfaces.

pixel geometry for each image, but typically range from 8-9. The total number of looks or each image is 13-15. Speckle noise is inversely proportional to the number of looks in a pixel, such that $1/N^{1/2}$. Therefore speckle noise in the finished products is 27%.

The data are then terrain corrected using the Canadian Digital Elevation Model (CDEM) in SNAP. The CDEM was produced by Natural Resources Canada to provide topographic altimetry data for all of Canada using data collected between 1945 and 2011. The new terrain corrected images are then imported into ESRI's ArcGIS software package and mosaicked together in ArcMap (Figure 15).
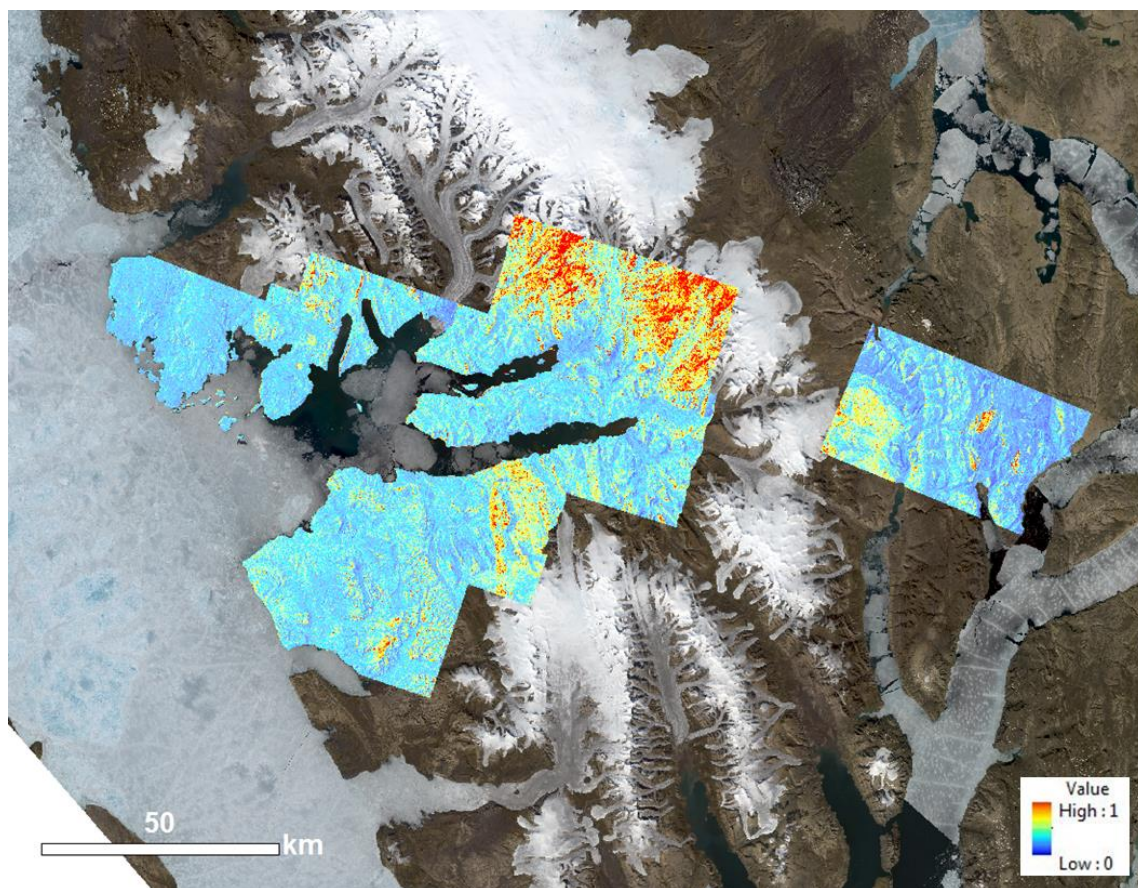
Figure 15: Mosaic of RADARSAT-2 circular polarization ratio (CPR) images over Landsat-8 true colour composite mosaic of Axel Heiberg Island. Water has been masked out. A maximum-minimum stretch has been applied from 0-1, highlighting any areas of double-bounce backscatter (CPR > 1) as bright red.

Archival PALSAR-1 images from the Advanced Land Observation Satellite (ALOS) were acquired through the Alaska Satellite Facility. PALSAR-1 had a longer wavelength than RADARSAT-2, with a 23 cm L-Band SAR. Having a longer wavelength means that these images can penetrate deeper into the surface than C-Band and it measures roughness at the decimeter scale rather than the centimeter scale. Features which appear rough in C-Band may appear smooth in L-Band or vice versa. The PALSAR-1 images do not cover the same areal extent as the RADARSAT-2 images, but there is abundant overlap. The PALSAR-1 images are processed to produce HH intensity images (Figure 16) and CPR images (Figure 17) using same method as the RADARSAT-2 images.
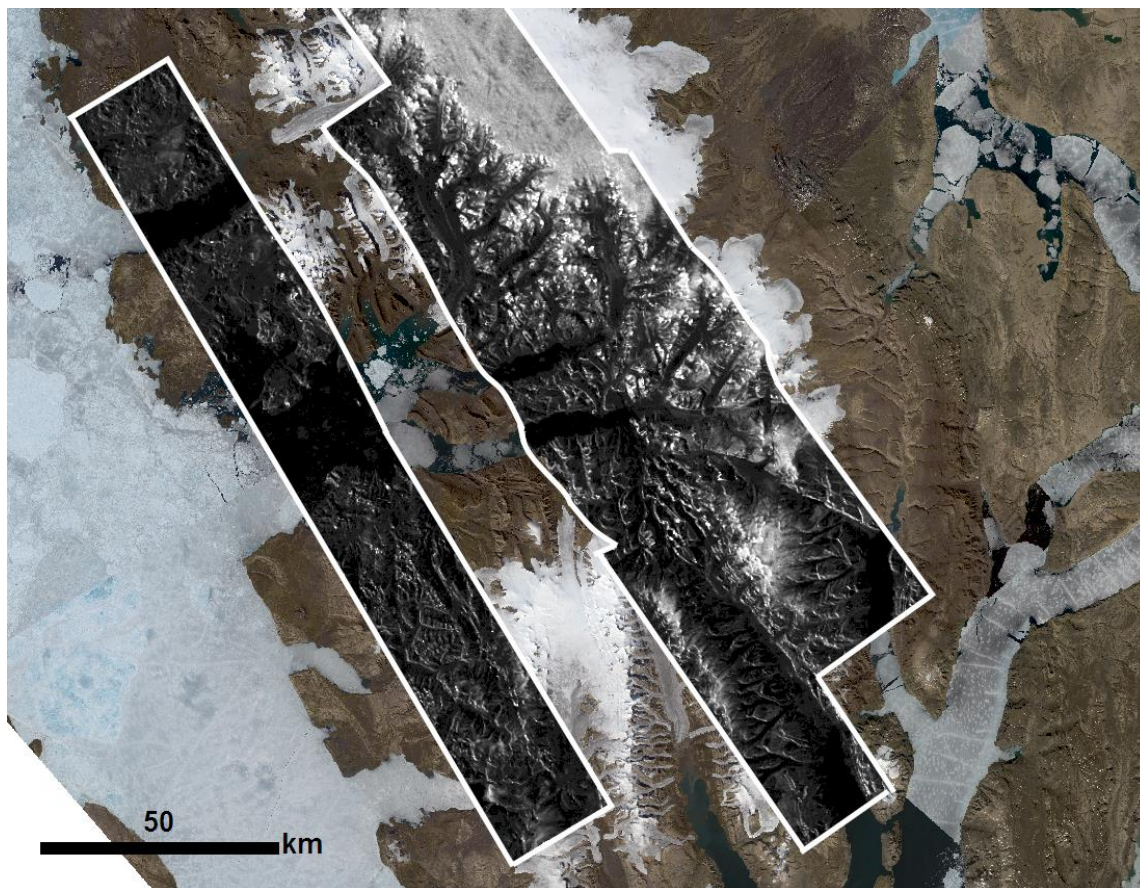
Figure 16: Mosaic of archival 2009 PALSAR-1 HH intensity images over Landsat-8 true colour composite mosaic (R: B4, G: B3, B: B2) of Axel Heiberg Island. Water has been masked out. PALSAR-1 used L-Band radar ($\lambda = 23$ cm), which penetrates deeper into surfaces than C-Band radar and is sensitive to roughness at larger scales.

There are some areas of overlap amongst the RADARSAT-2 image coverage, and there are some discrepancies between overlapping images. The discrepancies are likely the result of minor snow or ice melt during the summer season. Each of the images have different acquisition dates. The first set of radar images were taken in 2016 on June 24th, July 1st, July 18th, July 28th, August 1st, and August 11th. The second set images were acquired later in the season in the following year, on September 26th and 30th, 2017. Landsat-8 images archived from June-August 2016 and September-October 2017 help us to determine the extent of snow and ice coverage, which may alter the radar signals. The June 24th RADARSAT-2 image is roughly centred over South Dome. This diapir shows
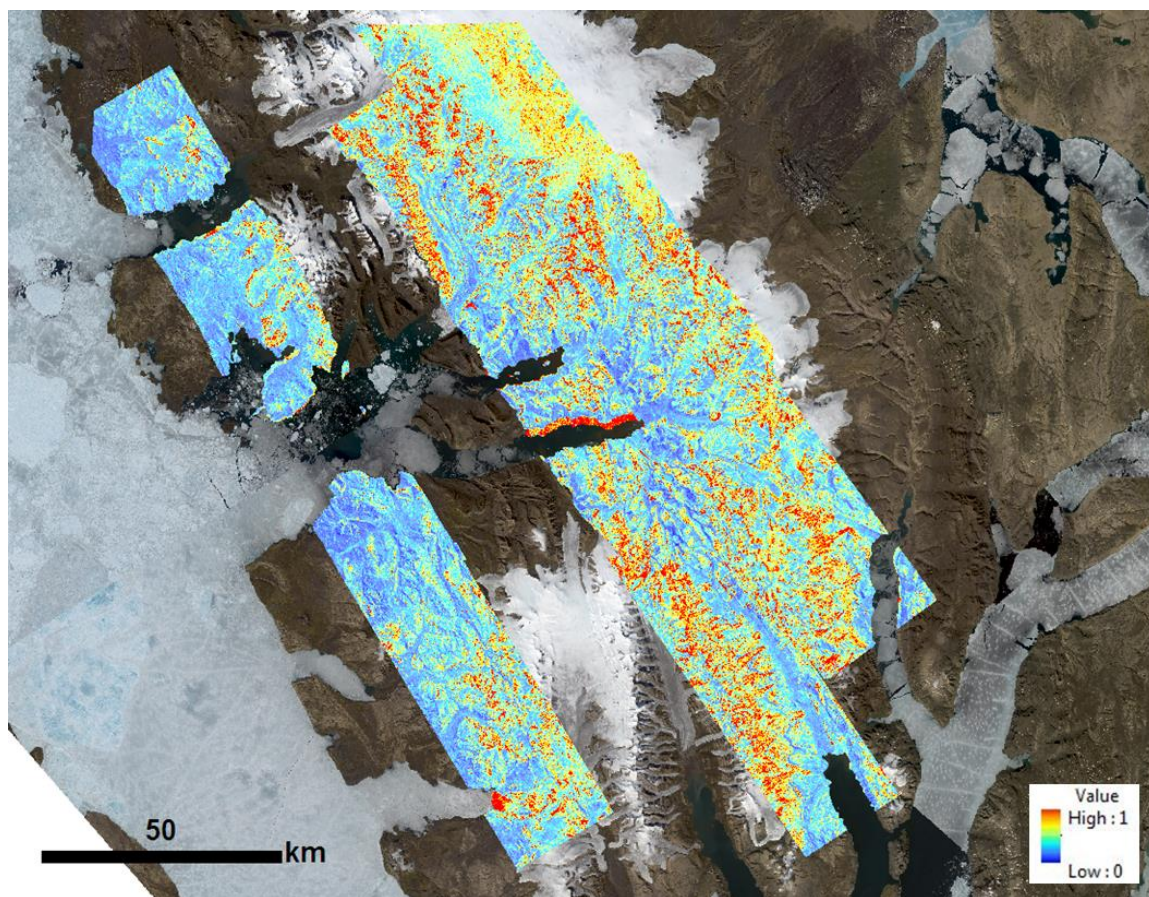
Figure 17: Mosaic of PALSAR-1 CPR images over Landsat-8 true colour composite mosaic of Axel Heiberg Island. Water has been masked out. A maximum-minimum stretch from blue to red has been applied from 0-1, highlighting any areas of double-bounce backscatter (CPR > 1) as bright red.

partial snow coverage on the dome itself and other high topographic points in a Landsat image acquired two weeks later, on July 8th. No Landsat images temporally closer to the radar acquisition date are in the archives over this area, but it can be extrapolated that the snow and ice coverage was likely equal or greater in extent earlier in the season, when the ambient climate is expected to have been colder. There is large overlap between the area covered by the June 24th and July 28th RADARSAT-2 images. A Landsat image acquired on July 29th shows almost no snow (Figure 18), so the July 28th RADARSAT-2 image is selected to overlap the June image in mosaics to attain the most reliable results.

The other 2016 radar images were also checked for possible interfering precipitation.
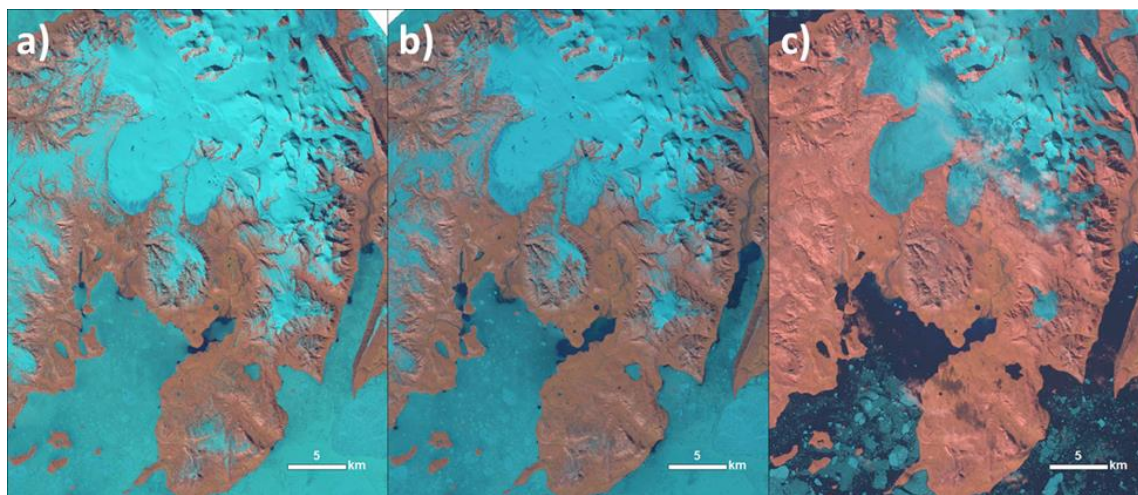
Figure 18: Landsat-8 RGB (R: B4, (Red: 0.636-0.673) G: B3 (Green: 0.533-0.590), B: B2 (Blue: 0.452-0.512)) images. a) July 8th 2016 b) July 12th 2016 and c) July 29th 2016, over South Fjord Diapir. Despite being a "true-colour" composite, the images have been stretched to highlight ice and snow in blue, and exposed rock in red. The July 8th images shows partial snow coverage on the dome itself, and high topographic points. The July 29th images shows almost no snow over the diapir. Because of the reduced snow coverage, the later acquired July 28th 2016 RADARSAT-2 image is used to overlap the June 24th image to reduce interference from ice.

Landsat imagery from July 7th, 2016 southwest of Strand Fjord shows snow on the highest peaks, suggesting that these peaks were also covered during the radar acquisition on July 1. A Landsat image from July 12th shows little snow on the highest peaks, leading us to conclude that there is likely little interference from precipitation in the July 18th RADARSAT-2 image. A Landsat-8 image from September 19th, 2017 shows that there is likely snow coverage throughout the September 26th and 30th, 2017 RADARSAT-2 images (Figure 19). The CPR signatures over glaciated areas have characteristic high CPR values in both 2017 images from the coherent backscatter effect in water ice (Campbell, 2002). In the September 26th image (Figure 19, rightmost CPR image) Whitsunday Bay diapir, Stolz diapir, and the diapir between them have distinctively high CPR values against the surrounding snow-covered terrain, leading to the conclusion that the snow coverage does not significantly affect data interpretation.
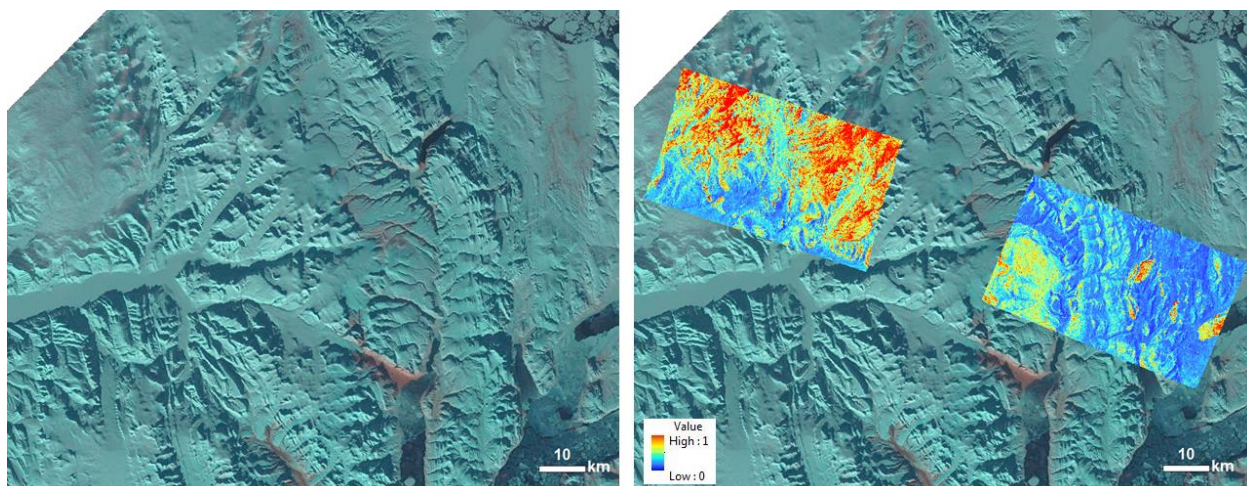
Figure 19: Landsat-8 OLI image from September 19th, 2017 shows that snow or ice covered the acquisition areas of the RADARSAT-2 images from September 26th and 30th. Max-min stretch applied to the Landsat-8 image shows snow and ice in blueish-green. Despite the snow coverage, rock units in the right RADARSAT-2 image still shows distinctive CPR characteristics between the salt diaper, glacier and snow-covered rock units.

2.3 Ground Truth – Axel Heiberg Island Field Season 2017

A field team visited Axel Heiberg Island in July 2017 to compare the salt exposure areas to the remotely produced maps, and to better understand their compositions and morphologies. The TIR and VNIR spectroscopy predict the presence of secondary sulphate salt material in floodplains and gully systems downstream of the diapirs. These deposits were located, documented, and sampled in the field. The SAR images predict differential surface roughness between the diapiric structures and the downstream salt deposits.

The team visited several diapirs on Axel Heiberg Island, including Wolf, Stolz, Strand, Whitsunday Bay, Colour, and South Fjord Diapirs (Figure 20). These investigations compared the scale of surface roughness (mm-m scales) of these diapirs to the SAR signatures (cm-dm scale). Field investigations were carried out through a combination of hiked and helicopter traverses. These sites were selected based on the prominence of salt signatures in the ASTER TIR (South Fjord and Whitsunday Bay Diapirs), an apparent
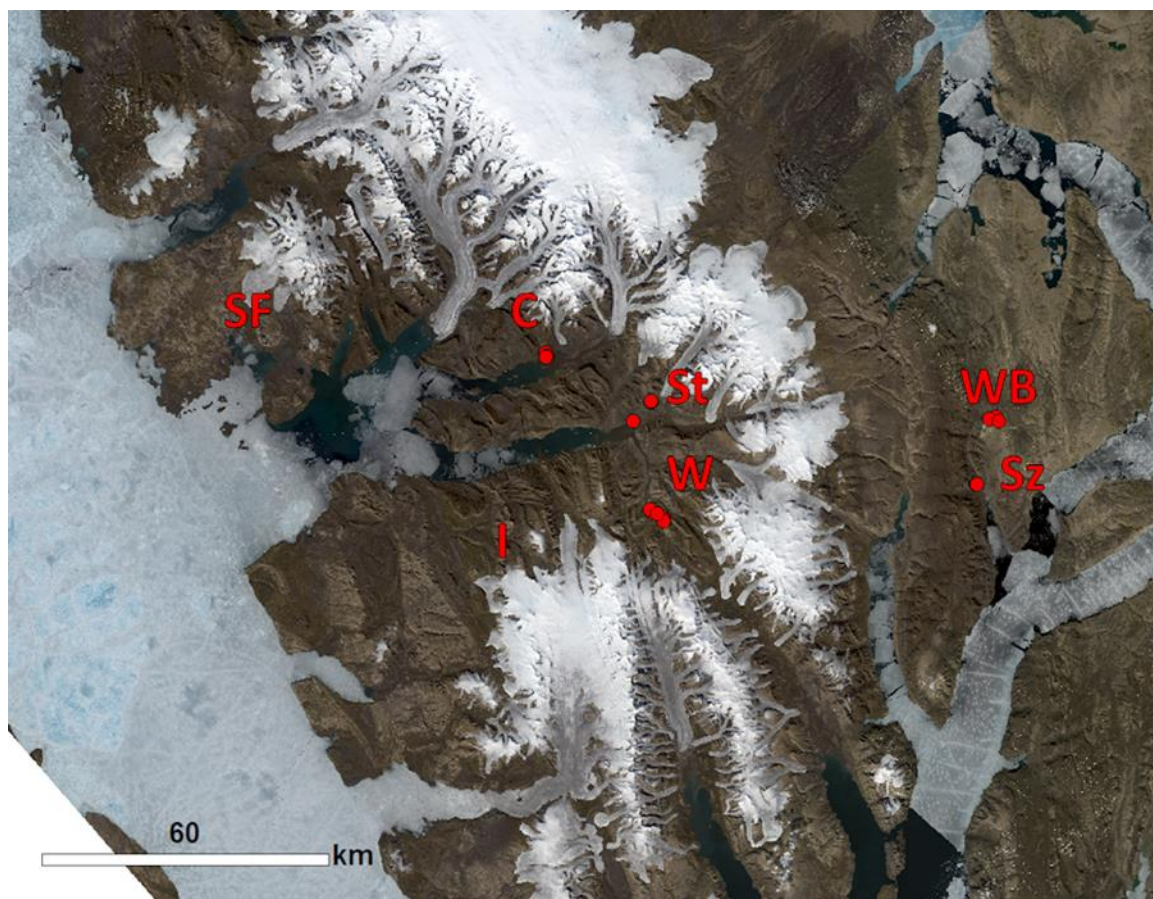
Figure 20: "True Colour" Landsat-8 OLI image (R: B4 (0.636-0.673), G: B3 (0.533-0.590), B: B2 (0.452-0.512)) of study area on Axel Heiberg Island. Visited salt diapirs are labelled. Red dots denote sites where samples for XRD analysis were taken (C: Colour Peak, I: Radar-rough Isachsen Formation, SF: South Fjord Diapir, St: Strand Diapir, Sz: Stolz Diapir, W: Wolf Diapir, WB: Whitsunday Bay Diapir).

contrast between radar rough and radar smooth salt signatures (Colour Peak), the reported presence of exposed halite (Stolz Diapir, Battler et al. 2013), and accessibility from chosen campsites (Lost Hammer Spring, Strand and Wolf Diapirs).

Lost Hammer Spring is a perennial spring that is hypothesized to be upwelling groundwater that has interacted with subsurface halite near Wolf Diapir (Battler et al. 2013). From this site, the team hiked a series of traverses to and around Wolf Diapir, along the north-flowing river floodplain, and around the hills north of camp. Samples were taken from Wolf diapir, salts precipitating in channel floodplains, and salts

precipitating in nearby gullies. From Strand Fjord, part of the team hiked to Strand Diapir and collected samples. Helicopter traverses facilitated the photo-documenting of structures that were not possible to visit on the ground, like South Fjord Diapir which was blanketed in abundant snow and ice (Figure 21).

By helicopter, the team were also able to land at and visit Stolz, Whitsunday Bay, and Colour diapirs on foot. Diapiric materials were sampled at each of these sites. At Stolz diapir, the team sampled exposed crystalline halite and the outflowing perennial spring. We climbed to the top of Colour Peak and were able to photo-document and sample a range of diapir material textures, including highly weathered surficial crusts and intact, grooved crystalline material, as well as precipitated salts around the basal perennial spring.
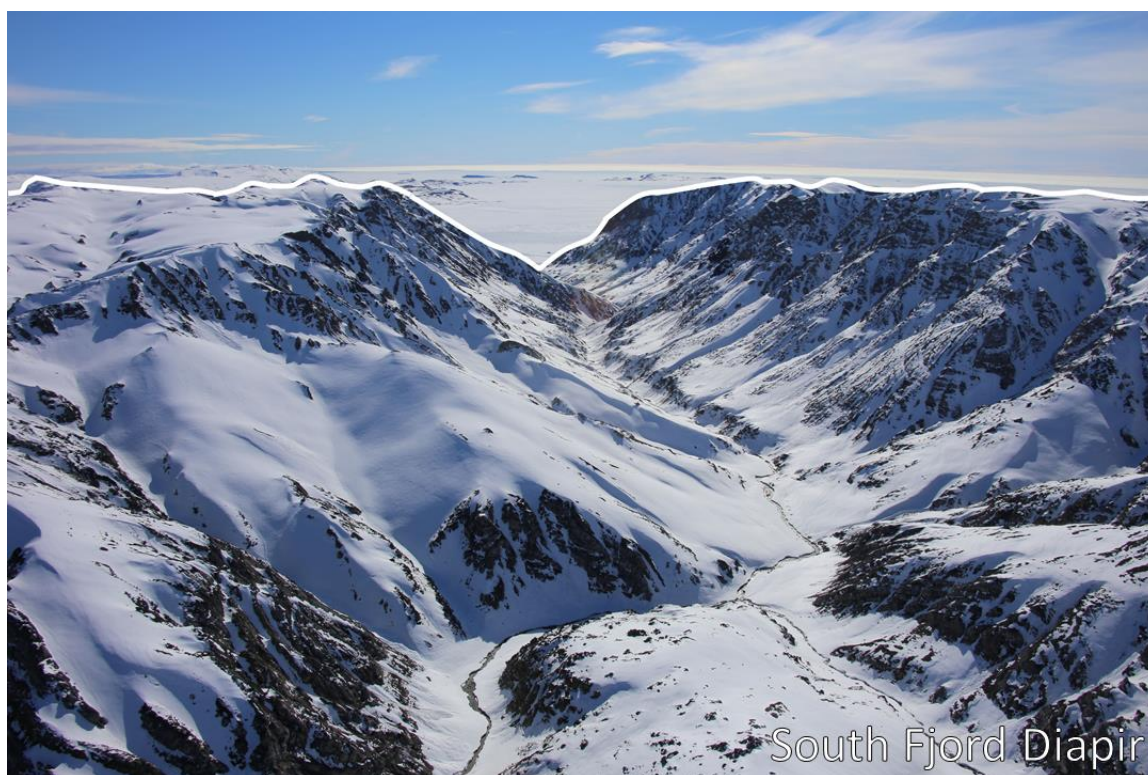
Figure 21: A helicopter traverse over the 5 km-diameter South Fjord Diapir showed that the dome was covered in snow in July 2017. Foreground (below white line) is the southern extent of South Fjord Diapir (Photo credit: Gordon Osinski 2017).

2.4 Powder X-Ray Diffraction Analysis

Powder X-Ray Diffraction (XRD) is a tool used to identify minerals by capitalizing on their unique crystal structures. Crystal structure are linked by atoms, ions, or molecules called "nodes". These nodes can link the crystal structure together through one or two dimensions, called crystallographic directions and planes respectively. Powder XRD is sensitive to the density of planes linking the nodes at the atomic level, and as such XRD allows us to infer crystal structures through their crystallographic density (Bragg 1915).

At a basic level, an XRD machine has an X-ray source and an X-ray detector. These are both aimed at a downward angle, facing each other. A powdered sample is placed in a sample holder positioned below and between the two instruments. When X-rays are emitted from the source, they are refracted within the crystal structure of the sample and are scattered in all directions. If waves received at the detector are in phase, there will be constructive interference and a peak will be recorded at the angle of incidence, θ, which will be a Bragg's angle for the mineral. If the waves are out of phase, there will be destructive interference and no peak will be recorded at that angle. When the crystallographic plane is at its Bragg's angle to the X-ray of wavelength λ, they will refract according to Bragg's Law (Equation 10).

$$2dsin\theta = n\lambda \qquad\qquad (Equation\ 10)$$

Bragg's Law explains the relationship between the Bragg's angle and crystallographic density. In equation 10, "d" represents the interplanar space, or distance between planes within the crystal lattice and "n" is an integer representing the order of reflectance. The XRD machine outputs a graph showing the number of counts over 2θ. The number of counts represents the number of times of recorded constructive interference received at the X-ray detector. From these peaks, the unique crystal lattice structure, and mineral identity, can be determined (Bragg 1915).

A total of 17 samples collected during the 2017 field excursion to Axel Heiberg Island were run through XRD analysis. These have been selected to ground-truth the composition of diapir and secondary salt materials against the predictions made from

orbital spectroscopy and the literature. Using the ASTER TIR and Landsat-8 VNIR and SWIR, the diapirs and secondary salts show the spectral characteristics of gypsum or anhydrite. The literature documents that the diapirs are made of anhydrite that is weathering to gypsum, so either may be present in each sample (Jackson and Harrison 2006). The samples were collected to reflect a diverse selection of diapirs and secondary salt deposits from each site visited during the field season. Sites represented include Colour Peak, Wolf Diapir, Stolz Diapir, Whitsunday Bay Diapir, and Strand Diapir. At each site, different categories of samples were taken. These include "solid" samples of intact diapir material with little alteration (Figure 22), surficial salts found downstream or nearby diapirs (Figure 23), perennial springs salts downstream of Stolz (Figure 24) and Colour diapirs, and highly weathered "crusts" on the outer surfaces of diapirs (Figure 25), and in the special case of Stolz Diapir, in situ halite crystal. The salts were ground into a powder by hand in a mortar and pestle before being run through the XRD machine.
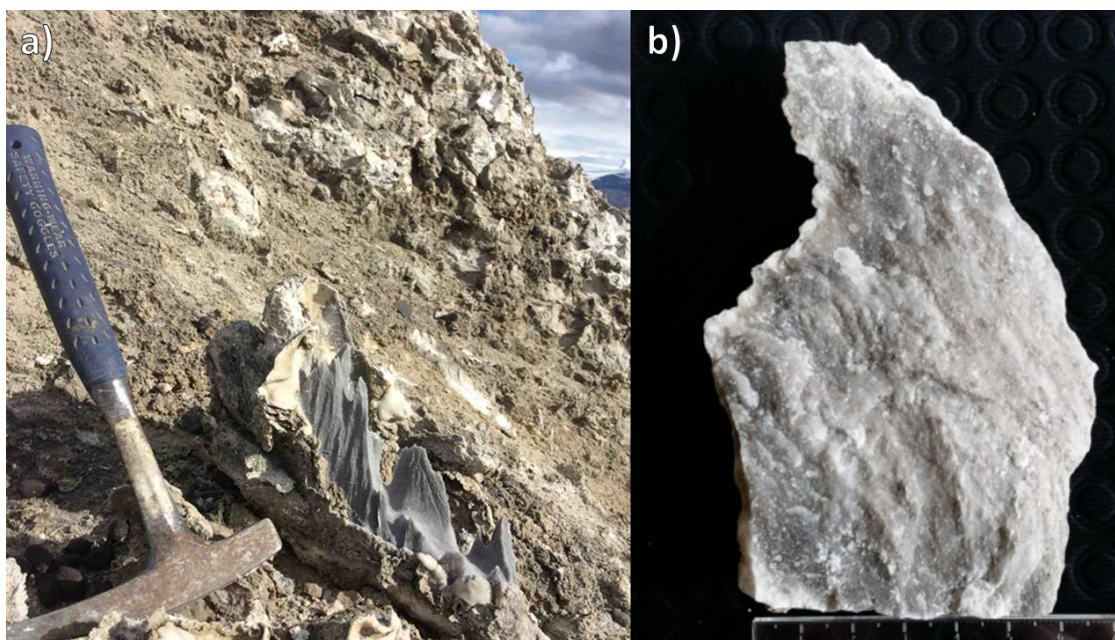
Figure 22: Many of the diapirs visited during the 2017 field season have crystalline structural components, in situ or as broken clasts. a) A broken clast of crystalline anhydrite with gypsum, with weathered crust below. The crystalline material has been eroded into a rillenkarren pattern, likely the result of prolonged subaerial exposure. b) Sample of crystalline salt material from Wolf Diapir.
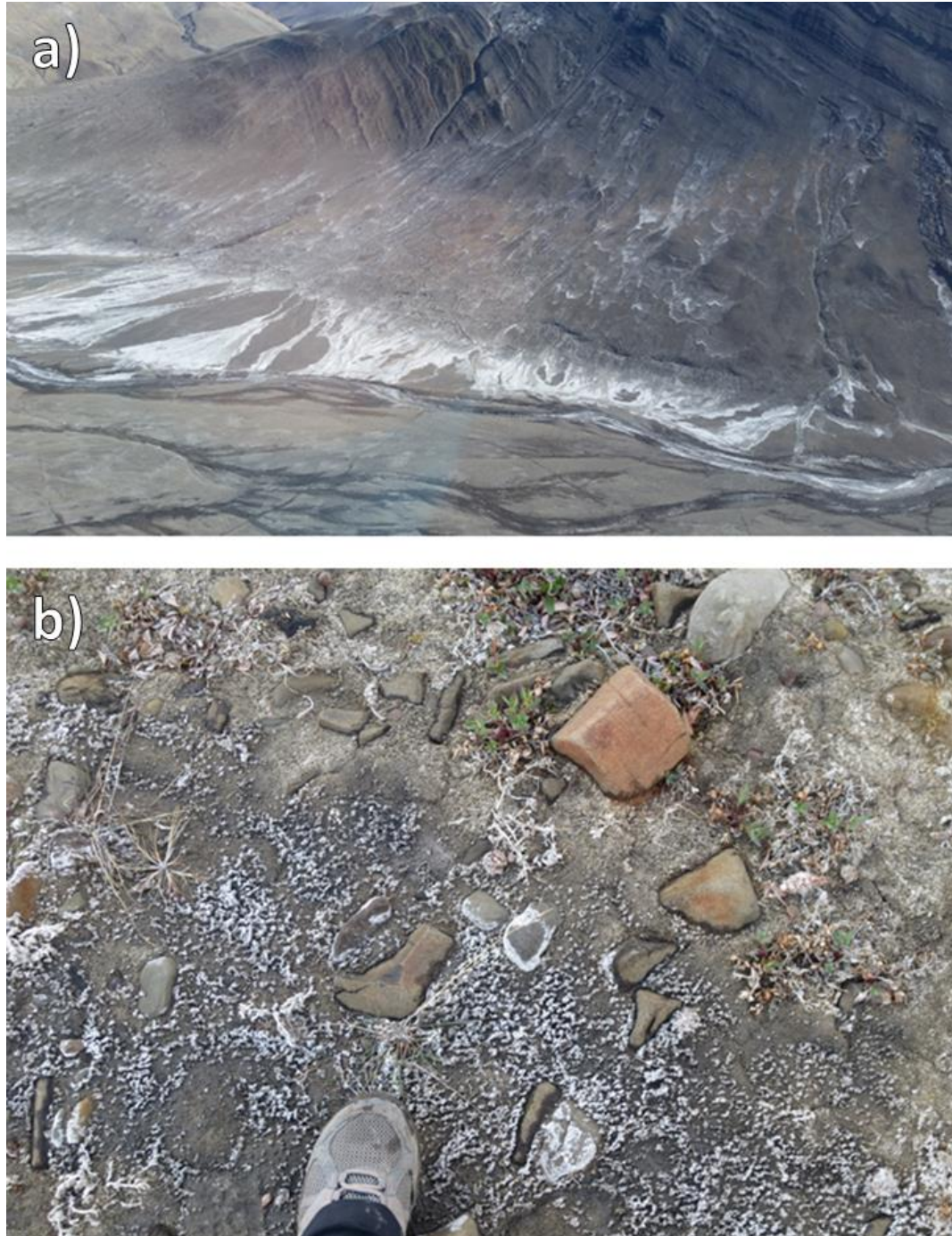
Figure 23: a) Salt minerals are seen precipitating in gullies, on slopes, between patterned ground cracks, and in the floodplains downstream from diapirs and exposures of the Otto Fjord Formation. b) These salts encrusted rocks in floodplains, as well as surficial soils and plants. These salts were not visible during periods of precipitation but recrystallized on dry days.

Figure 24: Two colours and textures in salts from perennial spring emerging from Stolz Diapir. The white salts are predominantly halite/hydrohalite (NaCl, NaCl·2H₂O) whereas the darker grey salts are predominantly thenardite/mirabilite (Na₂SO₄, Na₂SO₄·10H₂O) (Fox-Powell et al. 2018). The different salt mineralogies appear to have separate spring outlets feeding them. Perennial springs are fed from upwelling of salt-saturated groundwater near the base of some diapirs on Axel Heiberg Island.
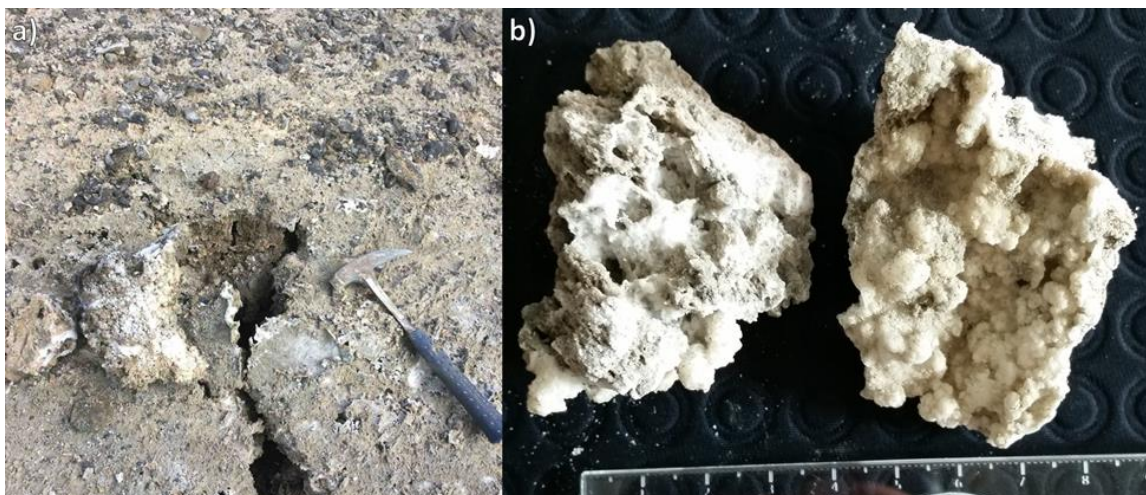
Figure 25: The surfaces of the diapirs are highly weathered and altered to a vuggy crust. a) Vuggy crust on Colour diapir. b) Example of in situ crust from Colour diapir. This material often contained vugs from mm to dm scale. It was not uncommon for a foot to puncture 20 cm deep when climbing on this material.

Chapter 3

3   Results

As shown in Chapter 2, areas of high salt concentration are highlighted in a dark purple colour in the ASTER thermal infrared R: B12, G: B11, B: B13 band composite image, and in dark maroon in the Landsat-8 band ratio composite image R: B6/B7, G: B6/B5, B: B4/B2. These areas were manually traced in ArcGIS to map areas of relative high salt concentration or exposure (Figure 26a). The mapped areas are separated into salt signatures likely representing diapiric salt versus secondary salts (Figure 26b). The distinctions between salt categories have been made based on a combination of topography and existing geological maps. The average RADARSAT-2 and PALSAR-1 CPR values for each polygon are compiled in ArcMap and averaged to characterize the radar signature for diapiric and secondary salts in C-Band and L-Band radar (Appendices A-D). As hypothesized, salt diapirs appear rougher in radar in both C-Band and L-Band than the secondary salt deposits.
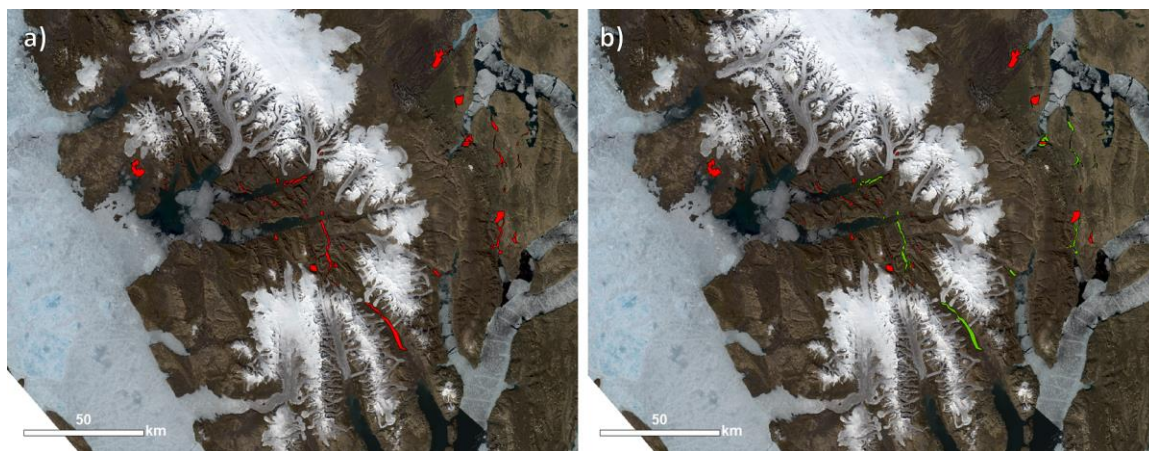
Figure 26: Areas manually mapped as anhydrite or gypsum salt using ASTER TIR data. Background image is true colour Landsat-8 composite image a) All areas mapped as salt shown in red. b) Areas interpreted as diapiric salt (red) and secondary, remobilized salts (green) have been separated out based on morphometric and topological interpretations. Secondary salts are primarily found in gullies and floodplains.

Another outcome of the spectral remote mapping is the discovery of a small island showing salt signatures. The island is located within the WABS region and has the same apparent signature in the Landsat-8 and ASTER composite images as the gypsum and anhydrite diapirs (Figure 27). We interpret this exposure to be a new diapir which is not previously referred to on the geological maps. Previous mapping of the WABS region relied on helicopter and hiked traverses. The mapping was supplemented by aerial photographs and satellite imagery, but these were predominantly used for determining unit thicknesses and not spectral mapping (Harrison et al. 2015). Because the island is a small feature, it was likely overlooked during helicopter traverses and therefore not previously noticed as a salt exposure. This discovery shows that multispectral satellite imagery is a useful tool for regional-scale geological mapping, being able to cover more ground than field mapping alone.
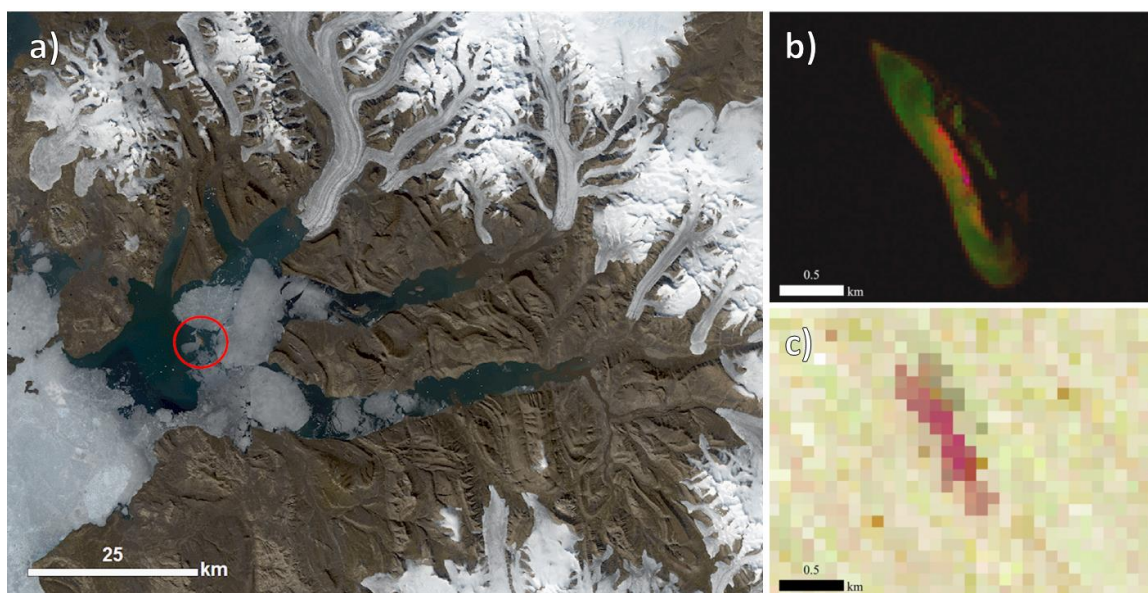
Figure 27: Interpreted salt exposure on small island in Strand Fjord. This exposure has not been included in any previous mapping exercises. a) Location of island on Landsat-8 true colour composite image. b) Landsat-8 band ratio composite highlighting salt in magenta (R: B6/B7, G: B6/B5, B: B4/B2). c) ASTER TIR composite image highlighting salt in dark pink (R: B12, G: B11, B: B13).

3.1 Radar Characteristics: Circular Polarization Ratio Values

The Zonal Statistics tool in ArcMap is used to calculate the average CPR values for each of the salt domes and secondary salt deposits in the study area. When the average CPRs for each of the salt domes in the RADARSAT-2 C-Band radar images are compiled, the average CPR value is 0.47 (scatter amongst individual pixels: SD = 0.23) per dome (Appendix A, Figure 28-29). For areas classified as non-diapric salt, the average CPR in C-Band is 0.24 (SD = 0.09) per outlined region (Appendix B). If we take the CPR values for areas mapped as salt by Harrison et al. (2015) through field mapping, then the salt domes have average values of 0.37 (SD = 0.17) salt in RADARSAT-2 data. Two factors may contribute to the CPR discrepancy between the spectrally mapped diapirs and the field mapped diapirs. One is that the field mapped salt data exclude diapirs in the Sept. 26 2017 RADARSAT-2 image which lies east of the WABS region. Whitsunday Bay diapir, east of the WABS region, appears to be the roughest diapir out of all of the RADARSAT-2 images and would skew the average. Second, Harrison et al. (2015) compiled regional field mapping that predicted and correlated rock units obscured by soil coverage. If parts of diapirs are buried beneath non-evaporitic soils, they will appear smoother in SAR, and will be less likely to register as salt in the spectral imagery.

There are some notable layover issues in the PALSAR-1 images, along with some registration problems. Layover is a phenomenon present in SAR images where the angle of incidence is near the slope angle of the terrain. Radar signals then encounter different parts of the radar-facing slope at the same time, and subsequently return to the receiving antenna at the same time. The resulting product shows the front-face of the slope as compressed in the radar image, whereas the back-facing slope will be distorted and elongated, or it will be shadowed (no echo data received) depending on its slope (Campbell 2002). This problem is more severe in the PALSAR-1 images than the RADARSAT-2 images because they were taken at a lower incidence angle. The polarimetric mode on PALSAR-1 has incidence angles $\leq 30°$, which is similar to the angle of repose for most surface sediments. The incident radar beams are inflecting near-perpendicular to the mountain slopes, producing foreshortened images as signals returned

from the tops of mountains are arriving at the same time as those from the bottoms of mountains. This effect shortens topographic features in the radar images. In contrast, the RADARSAT-2 SAR images were taken with higher incidence angles ranging from ~28-43°, such that foreshortening does not as significantly affect those images.

In the PALSAR-1 images, the layover often resulted in the mapped salt polygons to appear partially overlying water bodies. As a result, we only collected CPR data from a few selected polygons of TIR mapped salt that appeared to be well registered. Some of the polygons were manually shifted to align topographic features in the PALSAR-1 radar acquisitions with the topographic features observed in the DEM and TIR images. The CPR distribution for pixels in these polygons have high standard deviations. The salt domes have an average CPR of 0.59 (SD = 0.30) in the PALSAR-1 L-Band radar (Appendix C). Areas mapped as secondary salt in the PALSAR-1 images have an average CPR of 0.22 (SD = 0.12) per defined area (Appendix D).

These results clearly show that the secondary salt deposits appear much smoother in synthetic aperture radar than diapiric salt domes. The scale of roughness for secondary salts is similar at both C-Band and L-Band (averages of 0.22 ± 0.12, 0.24 ± 0.09).
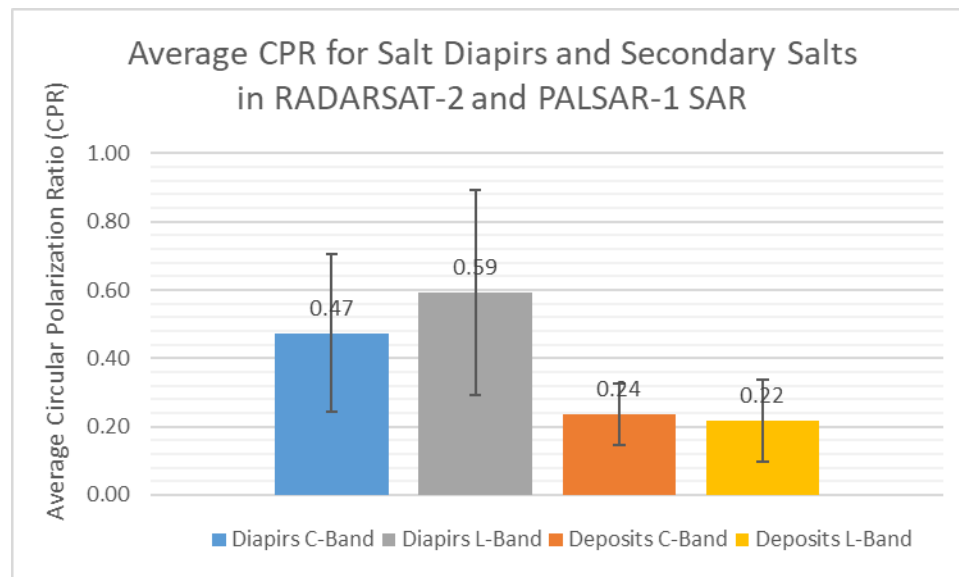
Figure 28: Average CPR values diapiric and secondary salt minerals in RADARSAT-2 C-Band radar, and PALSAR-1 L-Band radar.
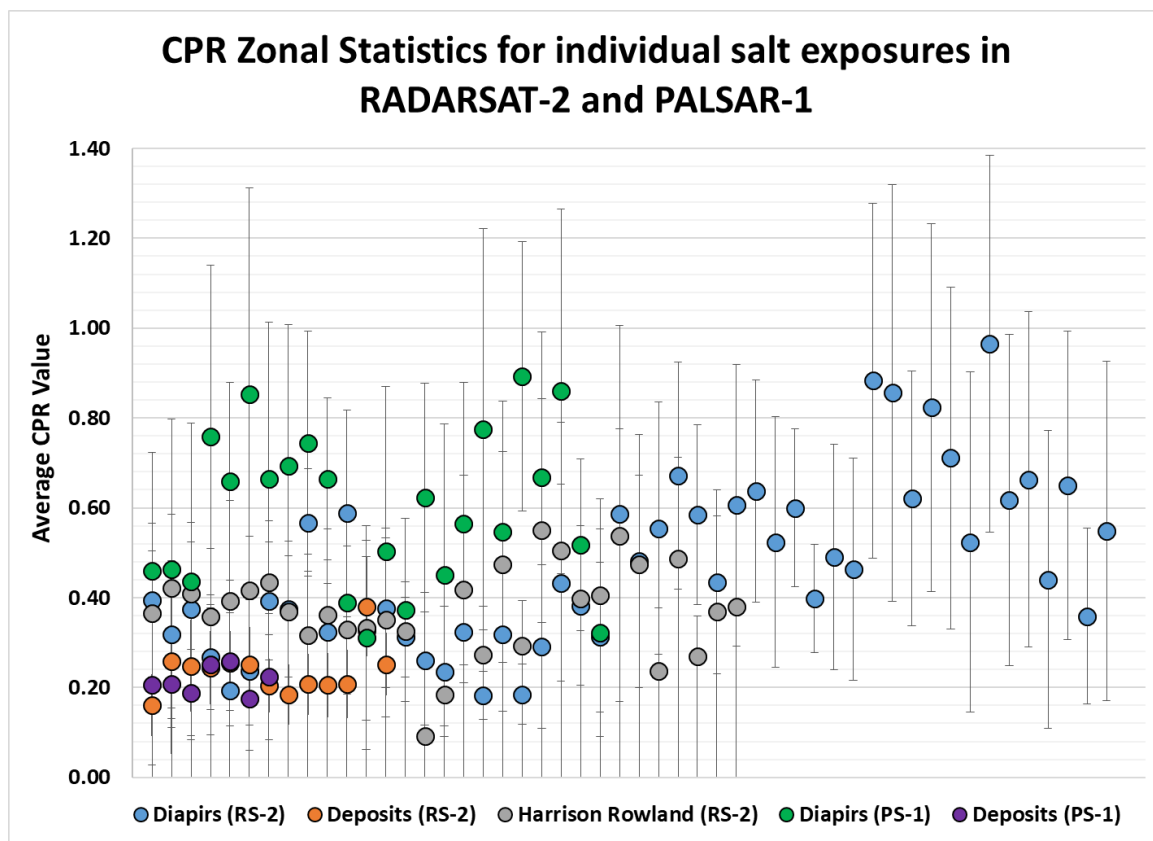
Figure 29: Average CPR zonal statistics for each exposure mapped as salt, for both RADARSAT-2 (RS-2) and PALSAR-1 (PS-1) data. Areas are divided into salt diapirs and secondary deposits. Also shown are the RADARSAT-2 CPR zonal statistics for areas mapped as Otto Fjord Formation (salt) in the field by Harrison et al. (2015). Error bars denote standard deviation of pixel CPR values within each mapped region.

In contrast, the salt diapirs appear slightly rougher on average in L-Band than in C-Band (averages 0.59 ± 0.30 compared with 0.47 ± 0.23). These values are statistically the same, although the small discrepancy may be caused by the preference for salt diapir outcrops to erode into boulders at the dm scale - closer in size to the wavelength of PALSAR-1 (23 cm) than to the wavelength of RADARSAT-2 (5.6 cm).

In general, the salt diapirs produce stronger signatures in SAR at both C-Band and L-Band wavelengths than surrounding rock units. Areas that are heavily glaciated are an exception. Because small voids and/or impurities in ice can cause internal forward

scattering of SAR, the received signals retain their initial polarization state (Neish and Carter 2014). Subsequently, glaciated areas show high circular polarization ratios (CPR > 1). However, one area of interest is south of Strand Fjord (centred at 79.063°N, -91.816°E), shows an anomalously high CPR signature in RADARSAT-2 (Figure 30).

This radar feature has been mapped by Harrison et al. (2015) as quartz sandstone belonging to the Isachsen Formation. During the 2017 field expedition, a helicopter traverse circled these mountains to determine what is causing the rough CPR signature. The topography is high elevation, steep mountainous terrain that is covered in cobble-sized colluvium that would appear rough at the scale of RADARSAT-2 SAR (Figure 31).

An archival Landsat-8 image (July 12th, 2016) taken six days before the RADARSAT-2 image acquisition (July 18th, 2016) of this anomaly show that the high CPR area was neither glaciated nor snow-capped during this time. It is therefore unlikely that the high CPR signature was caused by interference from precipitation. Instead it is likely that the anomaly is a true property of the surface itself.
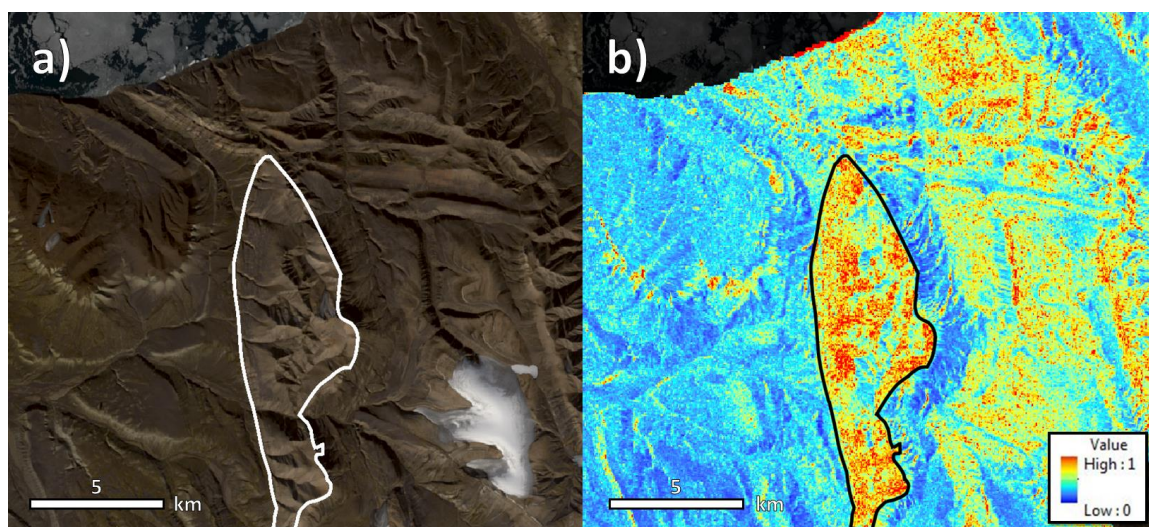
Figure 30: a) Landsat-8 true colour composite image, outlining anomalously rough area in the Isachsen Formation in white. b) RADARSAT-2 CPR image showing the anomaly, outlined in black. This rock unit has been mapped as quartz sandstone by Harrison and Jackson (2014).
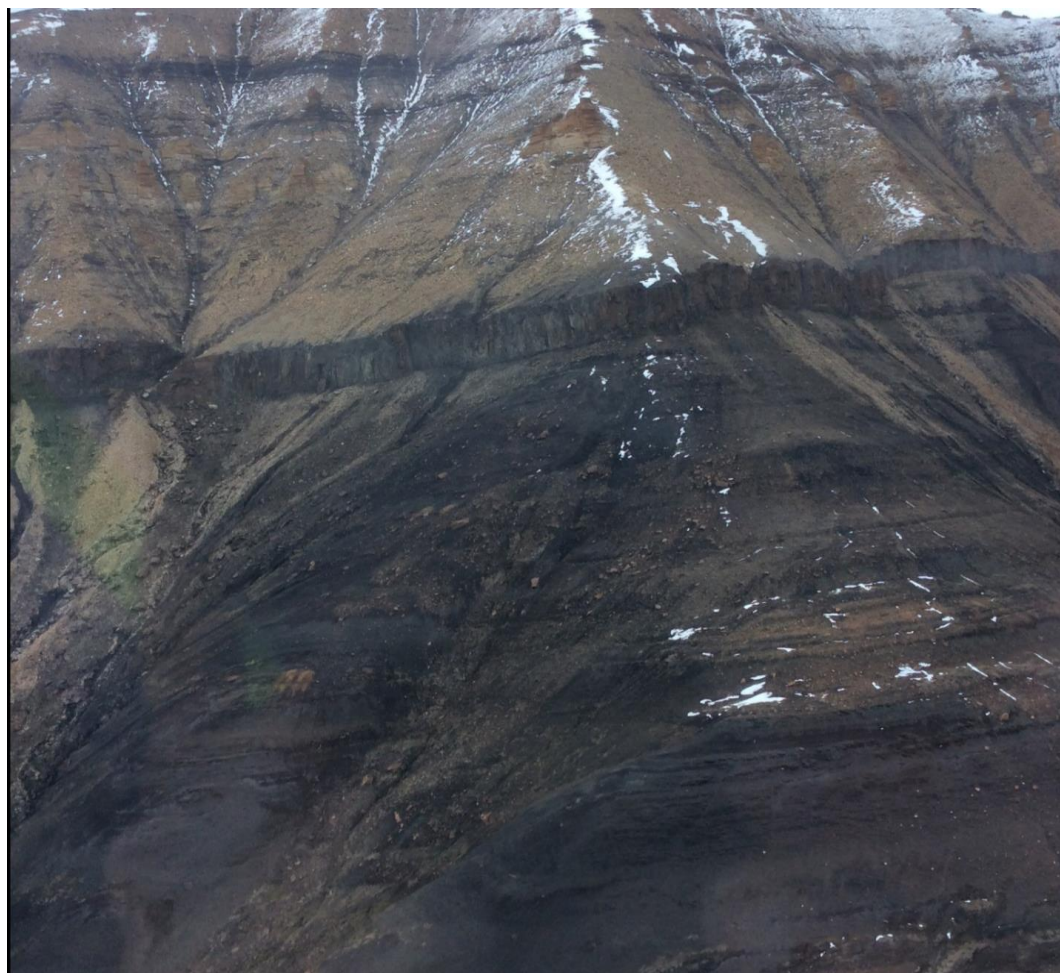
Figure 31: Photo of SAR anomaly from helicopter. The slopes of the mountain are steep and appear to be covered with 4-8 cm sized cobbles.

3.2 Ground Truth

Analyses made from radar and spectroscopic imaging are interpretive. The only way to confirm the presence of sulphate minerals in the outlined areas, and assess the true roughness of the salt diapirs, is by visiting these features in person. A field team visited Axel Heiberg Island in July 2017 to ground truth the remote observations by evaluating the surface composition and roughness of areas outlined in satellite imagery. These sites included areas of hypothesized radar-smooth secondary salts seen in the TIR and SWIR images in addition to known salt diapirs. Many diapirs on Axel Heiberg Island were

visited, including Wolf, Stolz, Strand, Whitsunday Bay, Colour, and South Fjord Diapirs. Field investigations were carried out through a combination of hiked and helicopter traverses. These sites were selected for a variety of reasons, including the prominence of salt signatures as observed in the ASTER TIR data (South Fjord and Whitsunday Bay Diapirs), an apparent contrast in CPR values between radar rough and radar smooth salt signatures (Colour Peak), the reported presence of exposed halite (Stolz Diapir), and accessibility from chosen campsites (Strand and Wolf Diapirs).

In general, all the diapirs show extensive evidence of chemical and mechanical erosion with vuggy karstic dissolution and broken cobbles and boulders of salt material. Surface rubble and sediment grain sizes used in this paper derive from the International Organization for Standardization scale (Table 1). Pebble and cobble sized particles of stratigraphically adjacent units are also entrained into the slope debris at many sites. Secondary gypsum/anhydrite and halite are precipitating not only in perennial springs (notably Wolf-Lost Hammer, Colour Peak, Stolz Diapir) but also in surface runoff on hillslopes, in gullies, and channel floodplains, as predicted by the TIR signatures. In this section, we will discuss how ground truthing diapiric and secondary salts on Axel Heiberg Island support satellite observations and will inform future remote predictions.

Table 1: Sediment size ranges according to the International Standardization Organization scale (ISO 2002).

NAME	SIZE RANGE (MM)
BOULDER	>200
COBBLE	63-200
GRAVEL	2-63
SAND	0.063-2
SILT	0.002-0.063
CLAY	≤0.002

3.2.1 Diapir Descriptions – Regional Textures

The diapirs are very rough, steep sided mountains that are covered in poorly sorted colluvium. The surface textures along the diapir slopes were variable. Some areas are covered in muddy material, others with dry sand, pebbles, and cobble-sized clasts. There are abundant mechanically eroded pebble to boulder sized gypsum scree along the flanks of the slopes, as well as down into adjacent alluvial fans and flattish slopes. At Colour Peak it is observed that although many boulders are scattered at higher elevations, fewer are observed downslope towards the perennial spring at its base (Figure 32).
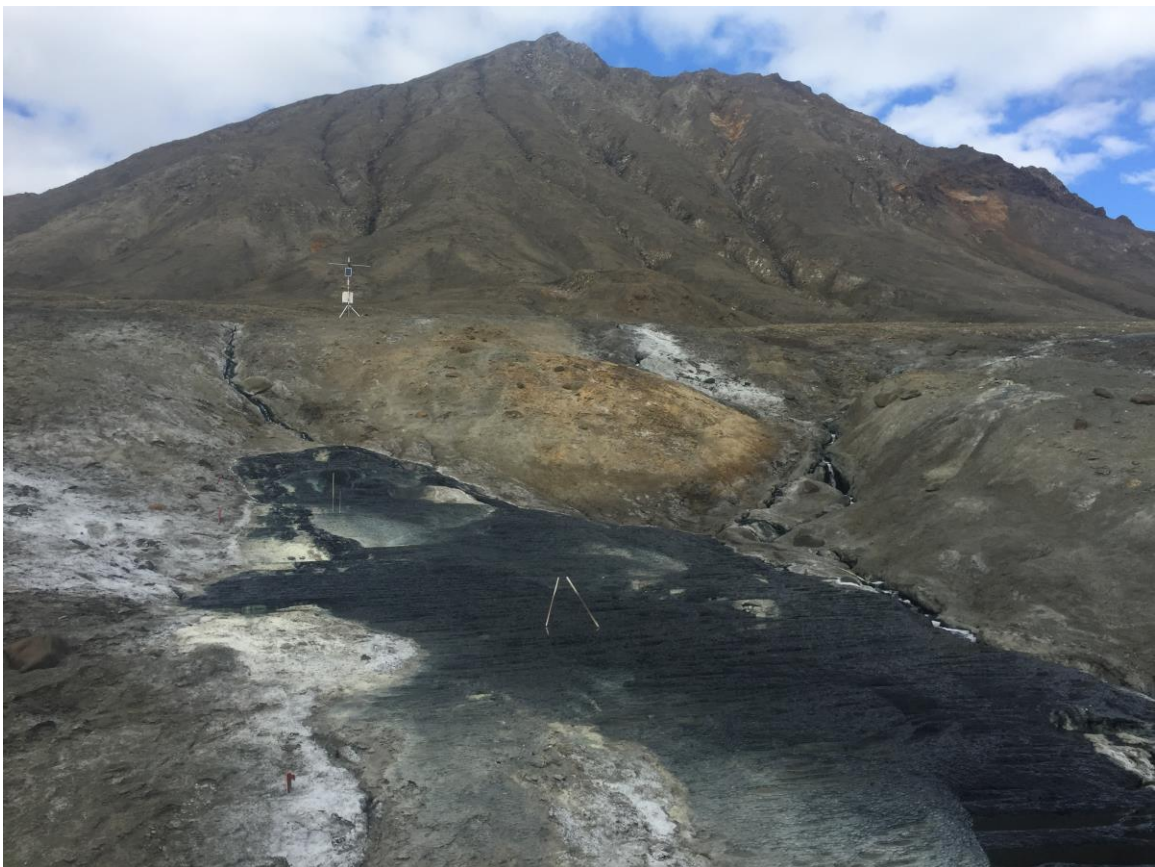
Figure 32: Perennial spring at the base of Colour Peak. The dark black/green area is travertine (CaCO$_3$ rock precipitating out of mineral springs). Most of the surrounding terrain is covered by sandy and muddy soil. The colluvium is pebble to cobble sized, with few boulders (Photo credit: Gordon Osinski 2017).

In contrast, the northern exposure of Strand Diapir is characterized by steep talus slopes with cobble to block sized scree with small patches of gravel and soil. It is likely that regional geomorphology partially controls the extent of the diapir exposed at the surface. Strand Diapir is located east of Strand Fjord - it has been eroded away within the U-shaped glacial valley and is exposed on the north and south side of the valley. The northern exposure is covered by soil and fine sediments to the west. In contrast, boulder-sized scree is ubiquitous along large gullies along the flank of Wolf Diapir and Colour Peak. The diapir outcrops themselves are pervasively rough from the formation of gypsum crusts, and large fragments breaking off mechanically, compared to surrounding quartz sandstone and shale formations. For example, the contrast in surface texture is sharp between Wolf Diapir and the neighbouring Isachsen and Christopher formations (Figure 33a). Whereas Isachsen formation has regularly distributed pebble and cobble sized rocks at its surface, the flanks of the Wolf Diapir are characterized by poorly sorted, very angular colluvium from sand to boulder sized particles. Similarly, Colour Peak is visibly contrasted in surface texture compared to the adjacent mountain to the west (Figure 33b).

3.2.2   Diapir Descriptions – Local Textures

The hand sample-scale texture of the sulphate rocks varies considerably. As mentioned in Chapter 2, diapirs demonstrated a range in textures from the solid, crystalline anhydrite in less altered outcrops to the vuggy, heavily weathered gypsum crusts. The solid, crystalline anhydrite is eroding into points like rillenkarren seen on halite diapirs and in karstic carbonates. The rillenkarren are smooth at the mm scale but undulate at the cm scale. Crystalline anhydrite or gypsum was only observed at Colour Peak and Stolz Diapir, but the gypsum crusts are found at all visited diapirs. Also present at all diapirs is rock that is softer than the crystalline material and is more friable. This rock exhibits variable toughness, with some samples being powdery, and others strongly cohesive. Samples of this type are referred to as "intermediate" because they appear to represent an intermediate weathering stage between the crystalline and crusty rock (Figure 34).

The "intermediate" rock dominates Wolf, Strand, and Whitsunday Bay diapirs. Although all visited diapir outcrops have vuggy crust material encrusting on boulders of Wolf-rock,

Figure 33: a) Edge of Wolf Diapir and the Isachsen Formation (quartz sandstone) is denoted by white line. Notice the even distribution of pebbles and cobbles in the surficial sediments over the sandstone, whereas the edge of Wolf Diapir is sharply defined by poorly sorted mixture of colluvium. (Photo credit: Gordon Osinski 2017) b) In the foreground, the lower slopes of Colour Peak are covered with assorted cobble and boulder sized colluvium and a rough gypsum crust, while in the background (above white line) the Christopher, Hassel and Kanguk formations appear smooth in contrast. c) Higher up on Colour Peak, the slopes are dominated by pebble to cobble sized colluvium, and jagged m-scale outcrops.
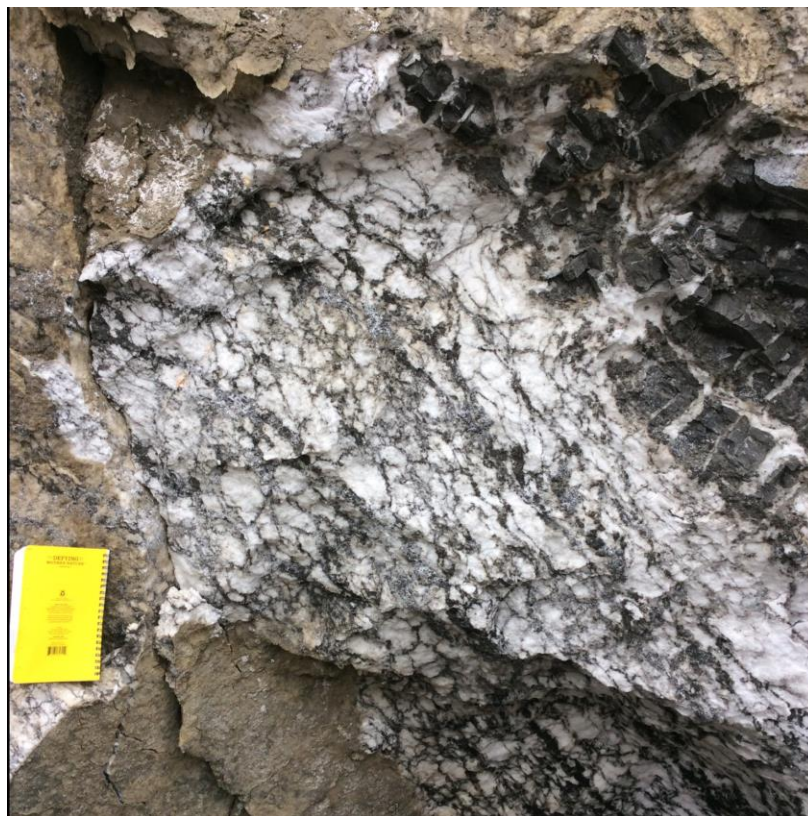
Figure 34: Salt outcrop at Wolf Diapir, veined with limestone. The salt at this outcrop is an intermediate phase between the crystalline anhydrite and gypsum crust textures. The rock is intact, but friable. 16 cm long notebook for scale.

the crust is more pervasive at certain sites. The flanks of Colour Peak are dominated by a few centimeters of a gypsum/anhydrite crust that shows evidence of being secondarily precipitated or highly weathered from dissolution processes. Beneath this crust are large vugs, frequently with 0.5 m deep cavities beneath. The crust itself is very rough at the mm to cm scale. It is also rough at larger scales where dm scale fragments have broken apart, revealing larger vugs.

In some areas, the diapirs are interbedded or veined within other types of rock. Exposures of Strand Diapir show interbedding with limestone. Stolz Diapir is the only site at which primary halite was found in situ. Two streams run through the diapir, and crystalline halite is found in an outcrop downstream of where the streams converge (Figure 35a, Figure 35b). Textures within the halite range from white powdery massive structureless

to colourless/grey clear crystalline halite with perfect cubic cleavage (Figure 35c). Some areas of crystalline halite are yellow-green tinged from localized yellow spots which may be endolith colonies.

Surface textures become subtly smoother away from diapir cores. For example, there are sulphate exposures north of the bulk mass of Wolf Diapir, near Lost Hammer Spring. These outcrops appear blocky, but the talus slopes are very narrow and constrained compared to the bulk mass of Wolf Diapir. The exposed rock outcrop is grey and white, weathering to tan/brown. The gypsum here ranges from crystalline to massive with grains approximately 0.5-2mm in size. The rock is highly weathered and is very friable and powdery, without any of the more crystalline material seen at Colour Peak and Stolz Diapir. The diapir exposures show primary and parasitic folding from the m to dm scale. The talus does not appear nearly as rough as at Wolf Diapir, containing mostly sand and pebbles with localized blocks and cobbles which suggests that diapiric surface roughness is a function of proximity to the core of the structure.

3.2.3   Perennial Springs

Colour Peak (north coast of Expedition Fjord), Wolf Diapir (South of Strand Fjord), and Stolz Diapir (east of ice sheet, outside of WABS region) are in close association with perennial springs, which have unique chemistry. Downstream of Stolz Diapir are extensive, thick perennial spring deposits. Two streams run through the structure, converging along the eastern flank. These streams have similar water chemistry but different sediment loads. Both streams are highly saline, with more Na and Cl than the other perennial springs (Fox-Powell 2018). The streams are hypothesized to run through Stolz's core. Stolz is the only diapir with exposed crystalline halite, but all diapirs from the Otto Fjord Formation are hypothesized to have a halite core. This is because saline perennial springs are present across the island at Lost Hammer Springs, Stolz Diapir, Colour Springs, and Gypsum Hill (Battler et al. 2013; Harrison and Jackson 2014a). The salts within Stolz spring have varying textures, colours, banding, and crystal structure. Upstream are alternating light and dark grey salts. Downstream by a pool are pure white, snow-like salts with bladed/rod crystal structures. The strength of anhydrite/gypsum spectral signature over the spring deposits is notably weaker than the signature over the
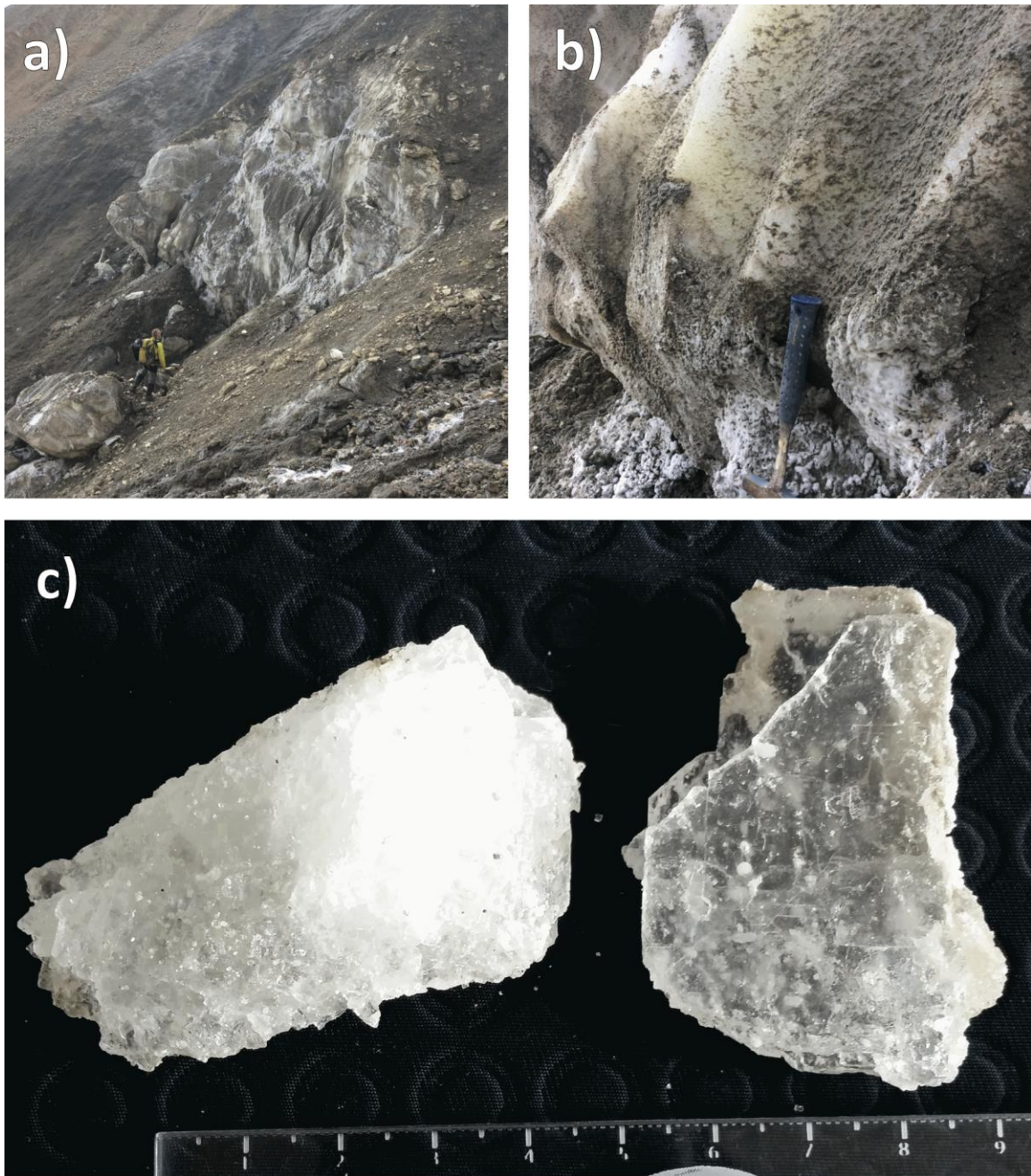
Figure 35: Stolz Diapir is the only diapir on Axel Heiberg Island known to have exposed crystalline halite in outcrop. a) Full view of halite outcrop. b) One section of the halite outcrop that appears tinged yellow. Rock hammer for scale. c) Two textures of halite samples acquired from Stolz Diapir. The left sample is a crystal aggregate, the right sample is from a single large crystal.

diapir itself, likely because the spring is predominantly formed from precipitated halite or calcite travertine.

At Colour Peak, the basal spring smells strongly of H_2S and predominantly precipitates a black calcite travertine and cubic 1-3 mm halite crystals as opposed to gypsum or anhydrite. The presence of H_2S may be related to the formation of gossans around the diapir. Gossans are highly oxidized, iron-bearing rocks. Because of iron oxidation, gossans are often vivid colours, including orange, yellow, and brown. These alteration colours lend to the naming of Colour Peak. Gossans are found in close association with diapirs on Axel Heiberg Island, including North Agate Fjord and Junction Diapir where basaltic intrusions in the Isachsen Formation are altering to form copper and iron sulphides and secondary copper sulphates (Williamson et al. 2011). The gossans are forming from the oxidation of igneous colluvial material found in the scree on the mountain, including gravel of angular igneous lithologies, including what is ostensibly dacite and diorite. Some samples of yellow rhombohedral crystals have been taken to the lab for analysis and may be included in other future works. The calcium sulphates in the diapir provide the sulphur for these alterations to occur. Similarly, around the northern exposure of Strand Diapir, scree in the talus exhibits a strong orange alteration similar to the iron oxidation seen at Colour Diapir. An orange unit capping the hill may be volcanics providing a source for the red staining. Stratigraphically, the salt overlies the orange unit, which may be stratigraphically related to the volcanics staining Colour Peak.

3.2.4   Secondary Salts

The ASTER TIR images predict that there is abundant gypsum and anhydrite deposits that exist beyond the extent of the diapir outcrops as predicted in the RADARSAT-2 and PALSAR-1 images. Ground truthing confirmed the presence of secondary salts as precipitated mineral encrustations in gullies, stream channels, floodplains, and on hillslopes (Figure 36). These salts form an encrustation on pebbles and cobbles in gravelly floodplains and gullies as well as coating some patches of fine-sediment soil in these areas and on non-channelized hillslopes. The composition of the secondary salts varies, with samples including gypsum, calcite, halite, mirabilite, and thenardite. Most of the powder XRD samples of secondary salts include quartz, probably as a contamination

from underlying clastic soils when the samples were taken. These surficial salt deposits are sufficiently pervasive to see from the air as well as on the ground. Although laterally widespread, the salt encrustations are <1 mm in thickness on the surfaces. In addition to the calcium sulphate minerals, halite was identified in some of the floodplain deposits north of Lost Hammer Spring (Figure 37).

Around the Lost Hammer Spring, a four-day period of rain and snow washed away the salts. The surficial salts were observed to reprecipitate after a period of dry weather. The ASTER TIR images show strong signatures for gypsum/anhydrite in the delta over Strand Fjord. During the field investigation, only isolated patches of salts were present, without extensive coverage. The salt is mostly seen precipitating at the contact between wet and dry sand. It had snowed a few days prior to the site visitation which may have washed away accumulated salt minerals. The strong salt signature in the remote spectroscopic data may been formed during a period of dry weather, which would imply that ASTER signatures are dependent on weather during and a few days prior to image acquisition.

Figure 36: White salt minerals are encrusting on the flanks and small gullies on a hillslope on Axel Heiberg Island.

Figure 37: Secondary halite minerals downstream of Lost Hammer Spring. 16 cm long notebook for scale.

Despite no gypsum or anhydrite appearing to precipitate from the spring at Colour Peak, there are thin encrustations of whitish salts precipitating on the surface of some soil patches, akin to the precipitated salts seen near Lost Hammer Spring/Wolf Diapir and in the Strand Fjord delta. There are also coarse sand grains to pebble sized clasts of selenite and other gypsum/anhydrite species within the soils downslope. In the colluvium, gypsum-rich soil, and encrustations are ample sulphates to produce the spectral signature seen in the ASTER TIR downslope of Colour Peak without appealing to the perennial spring to explain the salty spectral signature.

The areas that are radar-smooth but show salt signatures in the ASTER TIR spatially correspond with secondary salts observed in the field. These radar-smooth, salty areas consist of hillslopes and floodplains covered with soils and some colluvial or fluvial pebbles and cobbles. The salt bearing gullies and stream channels contain larger pebbles,

cobbles, and sporadic boulders, but these features are too localized to affect the CPR images at the scale of multilooked RADARSAT-2 (mean 37-49 m/pixel) or PALSAR-1 (mean 42-47 m/pixel) data. Although boulders and cobbles of salt have mechanically broken off diapiric structures, like the flanks of Wolf Diapir, these likely contribute to the rougher radar signatures seen in the CPR images in association with the diapir.

3.3   XRD Results

Seventeen rock and mineral samples were taken from Axel Heiberg Island during the 2017 field season. These samples were chosen to reflect a variety of textures and localities. As mentioned in section 2.4, the selected samples are qualitatively divided into four categories: solid, intermediate, crusty, and surficial. The first through are hypothesized to represent a spectrum of unweathered to highly weathered diapir material, whereas the surficial salts are of secondary nature, and are collected from encrustations on rocks in streambeds and efflorescence on soils. Each powdered sample diffracted the x-rays over a range of angles, where 2θ ranges from 2-82. The number of counts at each 2θ value is recorded in a table, from which a graph is plotted showing the relative abundance of counts. Angles at which the sample shows more instances of diffraction produce peaks. These peaks are like chemical "fingerprints" of mineral crystal structures and are compared against known standards for laboratory tested pure minerals (Figure 38). By matching peaks against known standards, the minerals in each powder XRD sample can be interpreted. The XRD results are summarized in Table 2, whereas the XRD plots for each sample can be found in Appendix E.

Our original hypothesis was that the solid samples would be composed of anhydrite, the intermediate samples a combination of anhydrite and gypsum, and that the crusty samples would be fully gypsum. Instead, the solid samples, while primarily anhydrite, also contain gypsum. Gypsum constitutes both the intermediate and crusty samples. Two of the solid samples did not contain anhydrite. These were was calcite (i.e. limestone) with secondary gypsum, and another was dolomite (i.e. dolostone) with secondary gypsum, trace quartz and other minerals. The literature describes the diapirs containing "subordinate limestone, [and] rare dolostone," (Harrison and Jackson 2014a), which explains the presence of these two rock samples at Whitsunday Bay and Strand Diapir.
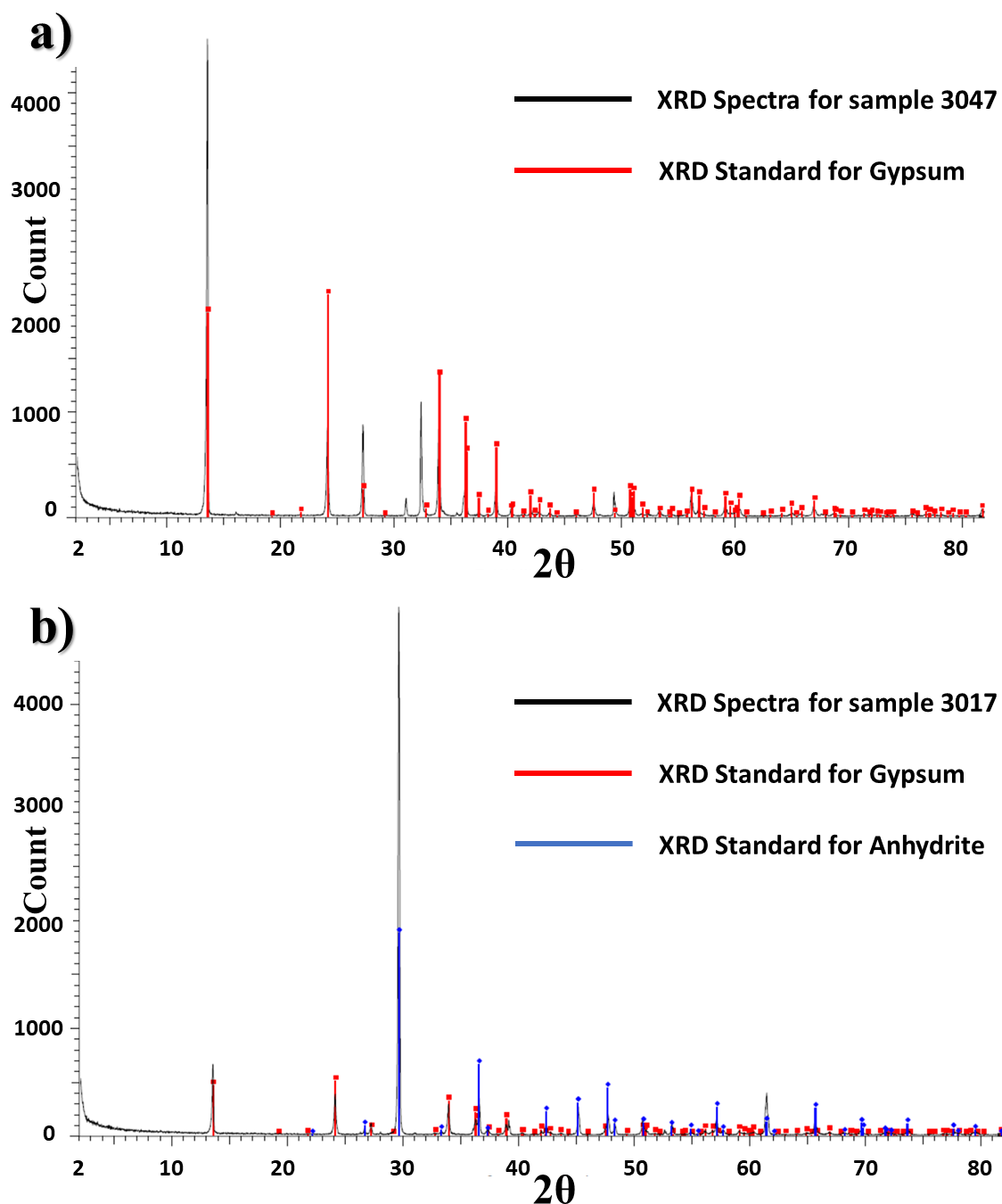
Figure 38: XRD for two samples from Colour Peak a) Sample 3047 is representative of the "crusty" diapir material and matches the XRD pattern of gypsum, notably the prominent peak at 2θ = 13 (Pedersen and Semmingsen 1982). b) Sample 3017 is "solid" diapir material and matches the spectral signatures for both gypsum and anhydrite (Hawthorne and Ferguson 1975) indicating both minerals are present.

Table 2: Summary of XRD results for rock and mineral samples acquired during 2017 field season to Axel Heiberg Island.

SAMPLE ID	SAMPLE LOCATION	SAMPLE TYPE	PRIMARY MINERAL	SECONDARY MINERALS	COMMENTS
3017	Colour	Solid	Anhydrite	Gypsum	
3047	Colour	Crusty	Gypsum		
3037	Stolz	Intermediate w/crust	Gypsum		
3038	Stolz	Intermediate	Gypsum		
3008	Strand	Solid	Calcite	Gypsum	
3024	Strand	Crusty	Gypsum	Trace Quartz	
3035	Strand	Surface	Quartz		
3043	Strand	Solid	Anhydrite	Gypsum	
3007S	Whitsunday Bay	Solid	Dolomite	Gypsum, trace quartz + other	3007S is solid part of sample 3007
3007PW	Whitsunday Bay	Intermediate	Gypsum		3007pw is intermediate part of sample 3007
3052	Whitsunday	Intermediate	Gypsum		Possible endolith
3016	Wolf	Intermediate	Gypsum		Possible endolith
3018	Downstream from Wolf	Surface	Halite		Changed colour after x-ray (Light to dark)
3032	Wolf	Solid	Anhydrite	Gypsum	
3033	Downstream from Wolf	Surface	Quartz	Gypsum Thenardite Clays	
3050	Gullies north of Wolf	Surface	Quartz (soil)	Gypsum Mirabilite Dolomite Kaolinite	Gullies after rain Analysis likely includes some local soil
3051	Wolf	Crusty	Gypsum	Calcite	

In contrast, the surficial salt samples proved very diverse. Often, they include traces of non-salt minerals (i.e. quartz, clays) but these are very likely contamination from the soil. The surface salts ranged in composition from pure halite ($NaCl$), gypsum with thenardite ($NaSO_4$), and gypsum with mirabilite ($NaSO_4 \cdot 10H_2O$) and dolomite. The presence of halite precipitating downstream from Wolf Diapir supports the hypothesis that the more

diapirs on Axel Heiberg Island contain halite cores than only Stolz Diapir. Nesse (2012) explains that thenardite can be found in saline lake evaporite deposits and can be found as an efflorescence on soil. The process of efflorescence reflects the secondary surficial salts observed to be precipitating on the soils and rocks on Axel Heiberg Island. As mirabilite is the hydrated form of thenardite, it is sensible that it should be found in the similar settings. The presence of thenardite and mirabilite in efflorescing soils and precipitating in floodplains down stream of Wolf Diapir provides further insight into the transportation pathways of the groundwater brine that feeds Lost Hammer Spring. Finally, the halite salt sample is noted to have changed colour after x-ray exposure. The original specimen was off-white in powder form, but after being run through the XRD machine it turned a darker grey colour. The implications of this change are unknown, but it is possible that the halite contains radiation-sensitive impurities.

Chapter 4

4   Discussion

The RADARSAT-2 CPR images, PALSAR-1 CPR images, and ground truthing expedition show that the salt diapirs on Axel Heiberg Island, Nunavut, are rough at from the millimeter to meter scale. The vuggy crusts are rough at the millimeter scale. The rillenkarren and gravelly debris are rough at the centimeter scale. The broken cobble and block sized colluvium are rough at the decimeter scale. Finally, the jagged outcrops of diapiric rock themselves are rough at the meter scale.

In contrast, the VNIR, SWIR, and TIR spectral imagery show that there are salts beyond the extent of diapir outcrops. These salts appear smooth at the scale of RADARSAT-2 (5.6 cm) and PALSAR-1 (23 cm) radar. Therefore, by using a combination of TIR and radar data, diapiric and non-diapiric salts can be distinguished remotely, making SAR a useful tool for studying and mapping salts in remote locations, including the Canadian High Arctic, as well as on other planetary bodies.

4.1   Diapiric and Non-Diapiric Salt

The diapiric salts exposed at the surface on Axel Heiberg Island are outcrops of the Carboniferous Otto Fjord Formation. This rock unit has been brought to surface by a combination of relative buoyancy, differential loading, and tectonic extension in relation to stratigraphically younger units. Although quaternary soils cover parts of the diapirs, each salt dome has components of intact outcrops, vuggy crusts, and mechanically eroded colluvium in the form of blocks, cobbles, and pebbles across their area. These are the components producing the radar-rough signatures seen in SAR.

In contrast, secondary salts are being carried away from their source by a combination of different erosive processes, including dissolution and precipitation from subsurface perennial springs. Groundwater that runs through the cores of salt diapirs is enriched with sodium, calcium, chloride, and sulphate ions (Battler et al. 2013; Harrison and Jackson 2014a). When the springs up well to the surface, the salts precipitate out, producing the elaborate springs seen at Lost Hammer Spring, Colour Peak, and Stolz Diapir. Even

though calcium sulphates dominate diapir outcrops, sodium chlorides and sulphates are abundant in these spring deposits in addition to gypsum/anhydrite. Each of these salts produce similar spectral signatures due to water absorption in the VNIR and SWIR ranges. Similarly, surface runoff from rain and snow will dissolve minor amounts of salt minerals out of the diapirs and transport them into gullies and stream beds. When the surface waters dry up, the salt minerals are left precipitated on the surface of the soil. Prior to the 2017 field season, the nature of these salts was unknown, but ground truthing confirmed that the secondary salts have been predominantly chemically remobilized rather than mechanically remobilized (precipitated rather than broken and gravitationally transported). The nature of the secondary salts lends them to precipitate in otherwise radar smooth areas, such as hillslopes, floodplains, and the edges of gullies.

The implication of this phenomenon is that gypsum and anhydrite initially identified by spectroscopy can be differentiated into diapiric and non-diapiric salts using polarimetric SAR. A case example of where this technique can be applied is at Colour Peak (Figure 39a). Colour Peak is a ~550 m high diapir with perennial springs emerging from multiple outlets at its base. There are also abundant remobilized salts from surficial weathering that have migrated downslope. In the ASTER TIR composite image (Figure 39b), the mountain itself and the slopes down towards the fjord are purple, showing signatures of gypsum or anhydrite. However, the RADARSAT-2 C-Band radar image (Figure 39c) shows that only the mountain itself appears rough; the perennial springs and delta to the fjord appear smooth. This example highlights how SAR in combination with orbital spectroscopy can be used to map salt diapirs. This section compares the CPR characteristics of diapiric and secondary salts in both C-Band and L-Band SAR and compares these characteristics to observations made in the field as well as in the spectral datasets.

4.1.1   C-Band vs. L-Band

The diapiric structures have higher CPR values in L-Band polarimetric radar than in C-Band, suggesting they may be rougher at larger scales. However, given the wide range of pixel values, and subsequent overlap in the standard deviations values (0.59 ± 0.30 in L-Band, 0.47 ± 0.23 in C-Band) there is no statistically significant difference between the
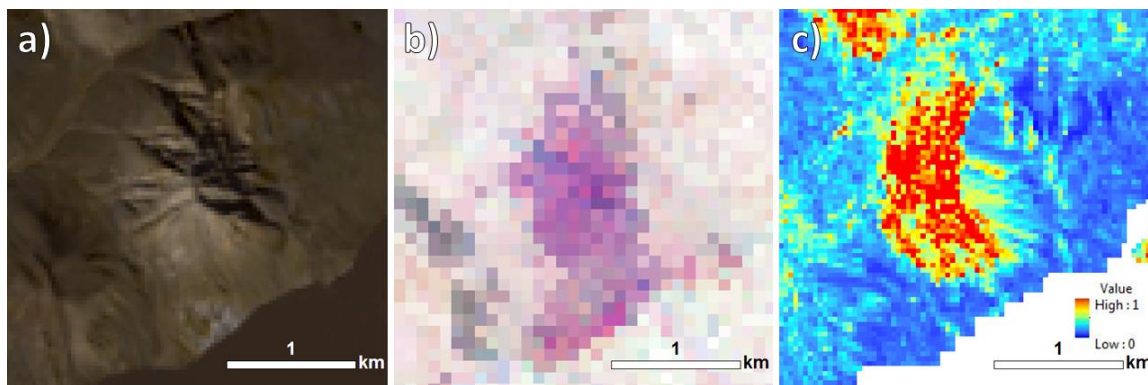
Figure 39: a) Landsat-8 true colour image of Colour Peak. Perennial springs appear white, and there are other, non-visible precipitated surficial salts down its slopes at its base b) The salts produce a gypsum/anhydrite signature in TIR (purple), both from the diapir itself and from the secondary and spring salts c) Only the diapiric mountain itself appears rough in the RADARSAT-2 C-Band CPR radar image.

two. The similarities in CPR values at both wavelengths supports the field observations and conclusions that anhydrite salt diapirs are rough from millimeter to meter scales. Still, it is more common for geological surfaces to appear smoother in L-Band than C-Band rather than vice versa. Erosive processes break materials down into smaller and smaller fragments, leading to surfaces to appear rougher at shorter wavelengths. Therefore, the discrepancy between C- and L-Band may reflect an unusually high distribution of dm-scale rubble-sized colluvium along the diapir flanks, similar to how a mass-wasting event would appear. Ground truthing revealed a large constituent of ~20 cm unsorted angular blocks around the diapirs which may be causing the slightly rougher CPR values seen in the PALSAR-1 imagery. The irregular distribution of these blocks may also contribute to the wide range of received signal intensity. In contrast, the CPR signatures of the secondary salts are very similar in both C- and L-Band. This is because the terrains in which these salts are efflorescing are smooth at both the cm and dm scales. Although these surfaces are rough at the mm scale, these the minute variations are unobserved at the scale of both radar wavelengths.

4.1.2   Spectral, Spatial, and Temporal Resolution

The spectroscopy techniques employed in this study can only be employed when multiple wavelength imagery is available. To produce composite and band ratio images, more than one wavelength is required to visually highlight specific absorption features. Further, it can be beneficial to incorporate data at multiple resolutions when performing remote predictive geological mapping. The salt exposures in the Landsat-8 images show some lateral discontinuity, which may be related to shadowing. Local incidence angles may have attenuated band strength, reducing the spectroscopic character in shadowed regions. Although the ASTER composite images do not appear to have issues with shadowed regions, mapping using ASTER images is limited to its 90 m scale of resolution. Subsequently, the most reliable salt maps were produced using a combination of both Landsat 8 and ASTER spectroscopy together to minimize mapping errors from shadows and poor resolution. Finally, unlike radar, passive remote sensing like spectroscopy is dependent on weather conditions. The Landsat-8 and ASTER images are mosaics of multiple images acquired over multiple orbital periods to minimize cloud coverage in the final products. Similarly, it was necessary to collect Landsat-8 images over a series of multiple days during summer 2016 and 2017 to check for snow and ice coverage. Because SAR is sensitive to snow and ice, these images helped determine the extent of interference from these sources during the RADARSAT-2 image acquisition.

4.1.3   Remote Sensing and Field Geology

One of the main differences between orbital remote sensing and field geology is that spectral remote sensing is more sensitive to the immediate surface materials than geological mapping. For example, in shortwave infrared, a 4 mm thick coating of salts on soil is enough to obscure the spectral signatures of underlying materials (Howari 2004). The composition of surface soil commonly differs from underlying bedrock, especially in vegetated areas that have developed soil horizons. Soil composition is dependent on sediment transport mechanisms and chemical/biochemical weathering. In the Canadian High Arctic, periglacial processes heave underlying bedrock materials. Conversely, fluvial and glacial activity transport allochthonous sediments for variable distances, masking the spectral signature of the bedrock.

The geological map shows Strand Diapir extending across the valley inland from Strand Fjord (Harrison et al. 2015). In the ASTER TIR data, the salt signature covers a much smaller surface area and is constrained to the north and south valley walls (Figure 40). Ground-truthing confirms that diapiric outcrops cover less of Strand Fjord at the surface than mapped by Harrison and Jackson (2014). However, that does not mean that the Otto Fjord Formation does not constitute the bedrock beneath the valley, only that the bedrock is occulted by glacial outwash plains. Perhaps the diapir spread across the valley long ago, but any surface exposure has been eroded away and buried by smooth Quaternary sediments during the last ice age.

Diapir exposures in the field appear to be rough at many scales, not just at the C-Band and L-Band wavelengths. The surfaces are covered in very poorly sorted colluvium, with sand, gravel, and rubble sized material. Based on surface texture alone, distinctive contacts can be effectively drawn between diapirs and adjacent units both in the field and in terrain corrected radar imagery. However, traditional geological mapping facilitates structural measurements (i.e. the strike and dip of rock beds) which provides insight into the lateral continuity of buried rock exposures. Field mapping also enables precise identification of units by being able to physically sample the rock. Gypsum and anhydrite have similar spectral signatures and cannot be differentiated via remote sensing alone.
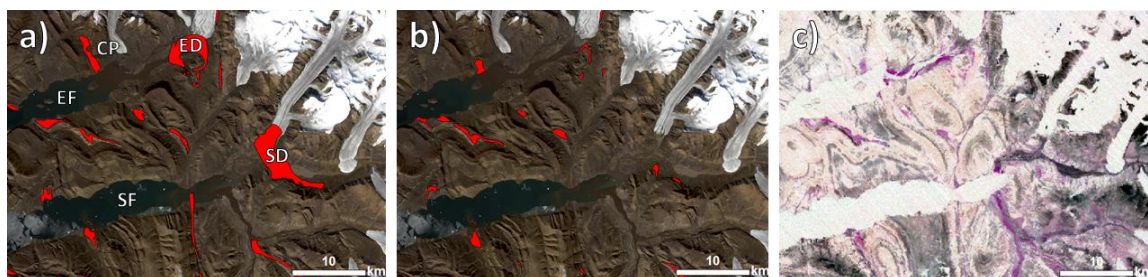
Figure 40: Strand and Expedition Fjords on western Axel Heiberg Island (CP: Colour Peak, ED: Expedition Diapir, EF: Expedition Fjord, SD: Strand Diapir, SF: Strand Fjord). a) Otto Fjord Formation salt as mapped by Harrison et al. (2015) b) Salt domes as mapped using ASTER TIR and Landsat-8 VNIR imagery, omitting hypothesized secondary salts c) ASTER TIR composite image, showing the very weak salt signature in purple over the northern extent of Strand Diapir.

A geomorphological distinction between salt diapirs and the surrounding rock and quaternary sediments is the absence of patterned ground. Patterned ground refers to land that has undergone seasons of cryoturbation, or freeze-thaw processes. During summer seasons, ice melts to liquid water which fills troughs and gaps in the earth. In winter, this water freezes and expands, wedging these troughs and gaps open further. This process produces a variety of surface patterns that are characteristic of periglacial terrain. Diverse forms of patterned ground and terrain polygons were observed across Axel Heiberg Island (Figure 41). However, polygonal terrain did not seem capable of surviving on any of the salt diapirs themselves, likely because of the steep slopes along diapir flanks and susceptibility of the diapirs for karstic dissolution (Figure 42). In contrast, areas that had accumulated thick quaternary sediments, including diapir derived materials, like the secondary salts and mechanically eroded diapir pebbles, were able to form these features (Figure 43). As an example, Whitsunday Bay Diapir is a large structure that is rough along its flanks and peak, with sharp contacts with smooth ground at its base. Below the diapir are smooth terraces with developed polygonal terrain.

Figure 41: Two adjacent textures of patterned ground in a stream floodplain on Axel Heiberg Island (Photo credit: Gordon Osinski).

Figure 42: Pits on Stolz Diapir collapsing from karstic dissolution. These troughs and gullies are the most similar structures to patterned ground seen on a salt diapir.

Figure 43: Patterned ground in valley and on upper terrace. The troughs between polygons have effloresced salts within them.

Although field mapping is more precise and gives more structural and petrological information than remote sensing, it is costly and time consuming. Areas that are not physically visited rely on extrapolation and interpolation. In contrast, satellite imagery provides widespread spatial coverage at low cost. For example, the island west of Strand Fjord discussed in Chapter 3 shows the characteristic TIR signature for gypsum and anhydrite but has not been previously mapped through geological survey due to its remote location.

4.2   Effects of Weather

Ground truth exercises during the July 2017 field season demonstrated that weather may play a role in the interpretation of remote sensing data. During the expedition, South Fjord Diapir was almost completely covered in a thick mantle of ice and snow. Conversely, both Landsat imagery and field exploration in June 2007 show the diapir being mostly exposed (Figure 44).

Although SAR is capable of penetrating materials, the presence of minute amounts of liquid water reduces the penetration depth by an order of magnitude. This means that SAR is less capable of penetrating to the ground in areas covered with veneers of snow mixed with near freezing water, as common in Arctic summers in which temperatures frequently rise above $0°$ C. Instead of representing the ground roughness, the SAR imagery reflects the snow surface roughness (König et al. 2001). This effect is useful for studies measuring snow and ice, but it obscures the local geology.

Spectral imagery may also be affected by weather. In our time at Lost Hammer Spring, the weather changed twice. When we arrived, the valley was sunny and dry. Abundant anhydrite/gypsum and halite salt minerals encrusted surface materials in channel floodplains, in gullies, and on hillslopes. After a four-day period of rain and snow, the amount of visible salt encrustations decreased. After the inclement weather, salts began reappearing on hillslopes and gullies as the landscape dried. Because the ASTER TIR images show widespread abundance of secondary salt minerals, it is probable that these images were acquired during a dry period. Furthermore, if the sky were cloudy, the clouds would block passive spectral sensors from detecting the surface. Although weather
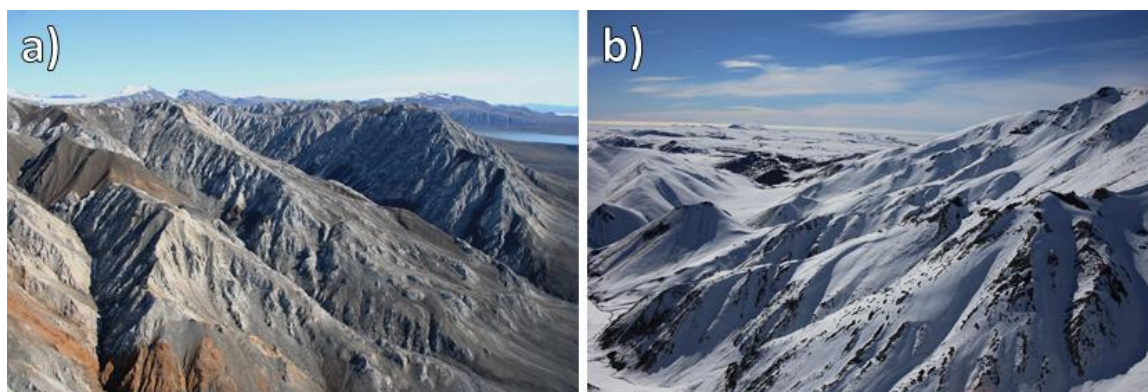
Figure 44: South Fjord Dome as seen during helicopter traverses. a) In July 2007, the diapir is almost free of snow. b) In July 2017, the diapir was not traversable by foot, being completely coated in snow (Photo credits: Gordon Osinski).

in the Arctic is highly variable, with many days fluctuating between sun, cloud, and precipitation, this may introduce bias in the spectral mapping as there is a higher abundance of precipitated secondary salts during sunny periods. TIR images acquired during wet intervals would probably show weaker salt signatures, with fewer salt minerals present at surface. Landsat-8 imagery can identify cloudy vs. clear days and estimate the weather. Unfortunately, no Lansdat-8 imagery is available around the time of the ASTER acquisitions, so it is not possible to confirm whether the ASTER images were acquired during a dry period or not. However, as Axel Heiberg Island is located within a polar desert, with mean annual precipitation <120 mm (Mueller and Pollard 2004) it is unlikely that precipitation will be a significant obstacle for spectral imaging.

4.3   Terrestrial Salts as a Planetary Analogue

Evaporitic minerals occur across the solar system. While they have only been confirmed via in situ analysis on Earth and Mars, salts have been inferred through spectral data to be present on the dwarf planet Ceres, Jupiter's moons Europa and Io, and Saturn's moon Enceladus. Some of these salts are dissolved in oceans, only to reach the surface when water upwells and breaches an icy crust, as with the case of Europa and Enceladus. Others are preserved within the rock record, like the sulphate sandstones comprising Meridiani Planum, Mars. Others are more enigmatic, possibly emerging from subsurface

brines forming the recurring slope lineae on Mars, or the bright spots on Ceres. On Io, NaCl and Cl_2SO_2 (sulfuryl chloride) are thought to arise from volcanism, depositing on to the surface and photodissociatiating into the atmosphere (Carlson et al. 2007). Although no spectral data are available, sulphate and carbonate melts have been hypothesized as a formation mechanism of Venusian canali (Kargel et al. 1994). The unique forces at play in salt tectonism, and the variable water chemistries of perennial springs sourced from diapirs are valuable analogues for studying salt minerals on other planetary bodies.

4.3.1   Mars

Although no Martian diapirs have been identified, layers of evaporites, including magnesium, sodium, and calcium sulphates, have been identified in Meridiani Planum (Clark et al. 2005) through measurements made by the Mars Exploration Rover "*Opportunity*" (Figure 45). These sandstones differ from most terrestrial sequences because the water has interacted with basalt rather than the felsic continental crust on Earth. Acidic waters leached abundant Mg^{2+} and Ca^{2+} ions from olivine in the basalt to form sulphates and chlorides, whereas remnant iron produced hematite (Fe_2O_3) nodules.

These salts have undergone multiple stages of diagenesis, with varying textures including recrystallization and vuggy dissolution. The different water chemistry formed relative abundances of salt minerals different from what we see on Axel Heiberg Island, favouring magnesium sulphates and including jarosite ($KFe^{3+}_3(OH)_6(SO_4)_s$) in addition to gypsum/anhydrite (McLennan et al. 2005). Although this study has not meaningfully quantified mm scale variations in surface roughness, the diapirs on Axel Heiberg Island do show variable mm-scale roughness between crystalline and vuggy surfaces. Future work could explore the diagenetic textural similarities, and the processes which form them, between terrestrial and Martian evaporates, despite compositional differences.

Besides the evaporite salts in Meridiani Planum, subterranean brines have been proposed to form recurring slope lineae (RSL). RSLs are dark streaks identified on slopes in equatorial Mars (Figure 46). They have been observed to grow in length downslope during warm seasons and fade or disappear during cold seasons (McEwen et al. 2001). The brine hypothesis proposes that a high concentration of salts underground would
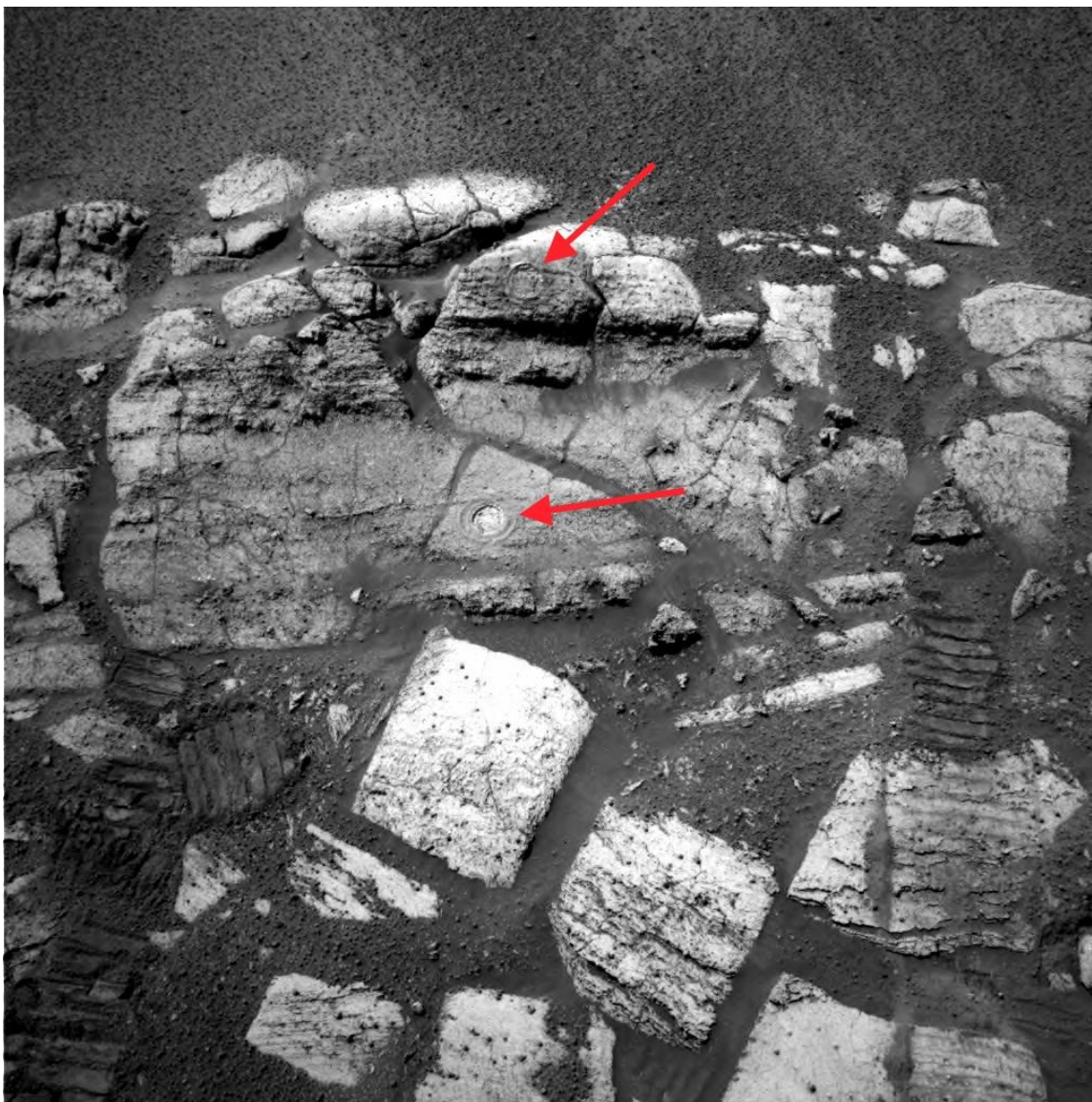
Figure 45: One of the first sites sampled by Mars Exploration Rover, Opportunity. Two holes 45 mm wide, 5 mm deep, (red arrows) were cleaned by the rock abrasion tool, then analyzed using spectrometers. The rocks contain types of sulphate minerals (Imaged modified from: NASA/JPL).

lower the melting point of subterranean ice, allowing liquid water to seasonally surface (McEwen et al. 2001). The water would facilitate downslope movement of regolith more easily than gravity alone. However, alternative hypotheses do not depend on brines, suggesting instead that flows may be fluidized by CO_2 or ice (Dundas et al. 2017).
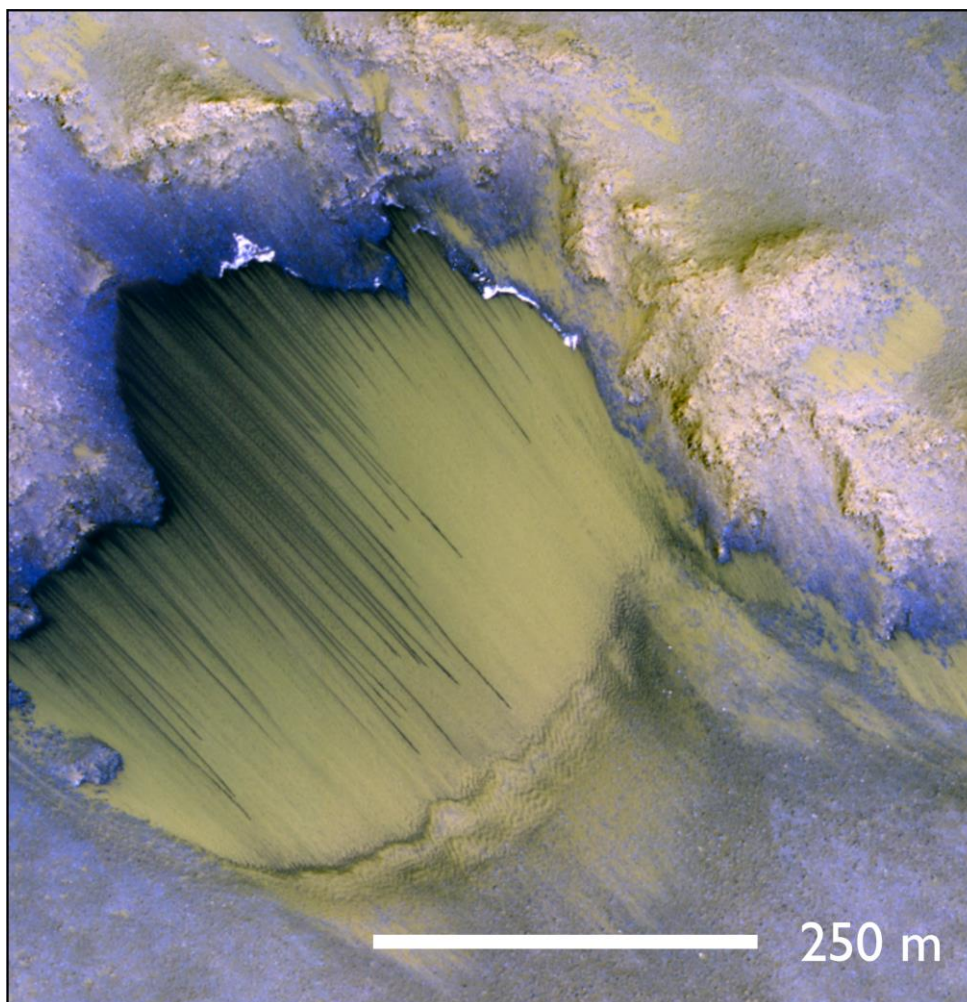
Figure 46: False-colour image showing recurring slope linae in Melas Chasma, Mars. (Image Credit: NASA / JPL-Caltech / University of Arizona, modified by The Planetary Society).

The spectral signatures associated with hydrated chlorate and perchlorate salts have been identified in the vicinity of RSLs (Ojha et al. 2015). The presence of near-surface brine would affect the dielectric properties of Martian soils in a few ways. First, the presence of water in the soil would greatly increase the dielectric constant in the soil, increasing SAR backscatter. This effect is amplified with the presence of conductive salts in the brine. These salts would precipitate as the brines dry out, remaining in the dry soil during the cold seasons. The salty dry soil would have higher dielectric properties than non-salty Martian soil, but less so than a wet soil. SAR is sensitive to dielectric properties, so if a

SAR instrument should be including on the Next Mars Orbiter, the possibility of salt minerals needs to be considered during SAR image interpretation.

Salts may also affect periglacial processes in both the high arctic and on Mars. Dissolved salts lower the liquidus of water, which in turn broadens the temperature window for freeze-thaw periglacial processes. With different times and seasons for freeze-thaw processes, salty ice-wedge polygons and cryoturbated patterned ground may show variations from fresh-water counterparts. Future studies may wish to explore patterned ground formations in salty versus non-salty soils to better understand periglacial terrain on Earth, as well as an analogue for other planetary bodies. The lowered liquidus of water from salts also broadens the temperature window for habitability of microbial life. If liquid water is stable in Martian hydrological systems, salty areas could be key targets for astrobiological exploration.

4.3.2   Europa

Jupiter's moon, Europa, is an ocean world. Its surface is a shell of water ice of unknown thickness (Billings and Kattenhorn 2005). However, a veneer of distinctive non-ice material is seen along some of the cracks and fissures in this shell (Figure 47). Although their composition is still unknown, a leading hypothesis is that the non-icy materials identified on Europa are hypothesized to be salt precipitates – water from Europa's oceans upwell through the fissures, spilling out, and precipitating dissolved salts (Greeley et al. 2000).

There is much interest in Europa's oceans, and their potential habitability for life. As a result, NASA has targeted this moon for the next flagship mission *Europa Clipper.* Europa Clipper will launch in the early to mid-2020s to assess the moon's composition, geology, ocean, and ice shell. To achieve these science objectives, she will carry an instrument payload including an ice-penetrating radar for detecting ice depth and subsurface water, an infrared spectrometer to determine compositions of non-water ice materials, a stereo camera for high resolution imaging and topography, a neutral mass spectrometer to study the atmosphere and geophysical tools for study of Europa's interior (Phillips and Pappalardo 2014). By characterizing the composition and spectral properties
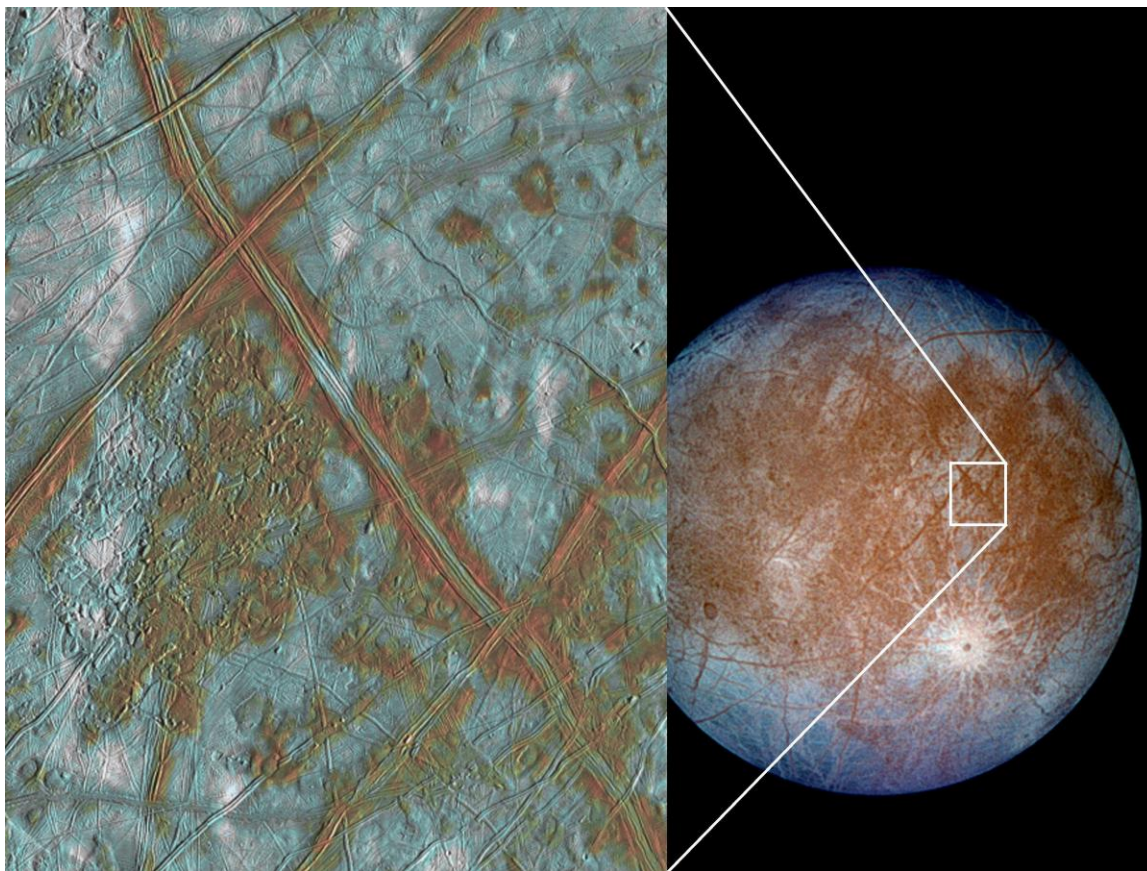
Figure 47: Chaos terrain on the icy shell of Europa. The light material is water ice, whereas the thin veneer of rusty material is not ice and is hypothesized to be a type of salt (Credit NASA/JPL/University of Arizona).

of naturally occurring terrestrial salts in the Canadian Arctic, we may be able to better constrain which salts are occurring on Europa when data from Clipper are returned (Fox-Powell et al. 2018). Ultimately, by gaining insight into what chemical materials are present in Europa's waters, astrobiologists will have a better understanding of what kind of life could potentially inhabit this ocean.

4.3.3   Ceres

Salt diapirism is possible on Ceres. With a radius of 470 km, Ceres is the largest body, and the only dwarf planet, in the asteroid belt. Ceres has enough mass to have undergone hydrostatic equilibrium from its gravity, giving it a spherical shape (Ermakov et al. 2017). It is geologically differentiated with separated silicate core, ice-rich mantle, and

rocky crust compositions (Buczkowski et al. 2016). Because Ceres' crust is denser than salt minerals and water ice, the differential loading and buoyancy requirements for diapirism and cryovolcanism are met. Three lines of evidence support the possibility of salt diapirism: the presence of bright salt patches on Ceres' surface, the presence of dome structures, and extensional fracturing resembling upwelling subsurface material. Across Ceres' generally dark surface are spots punctuated by very high albedo. The largest of these bright spots is in Occator Crater (Figure 48). Many materials have been postulated to comprise the bright spots, but spectroscopic data from the Dawn spacecraft have determined the materials to be natrite (Na_2CO_3) and ammonium salts (De Sanctis et al. 2016). The bright spots in Occator crater appear to be associated with fractures in the crater floor, as well as a large dome (Buczkowski et al. 2016). It is probable that these carbonates and salts emerged from below the surface, through the fractures or uplifting the dome. The presence of many such domes across Ceres suggests that there is either active convection or diapiric processes in the subsurface.

Figure 48: Colour composite image of Occator crater, Ceres. Bright white areas are natrite and ammonium salt exposures. This image shows topography with three times vertical exaggeration (from Nathues et al. 2017).

Upwelling processes have been confirmed at Samhain Catenae, a highly fractured topographic high on Ceres. The crust over Samhain Catenae is estimated to be at least 14 km thicker than Ceres' global average. The fractures appear extensional in original, supporting the hypothesis that internal convection or diapirism is a key tectonic process acting upon the surface of Ceres (Scully et al. 2017). If diapirism is causing the upwelling and extensional stresses associated with fractures and domes, and if the salt is sourced from areas of diapirism, then perhaps salt tectonics is a plausible process on Ceres. Should salt diapirism be occurring, a spectroscopic imager coupled with a SAR instrument may be able to differentiate between rough diapiric domes and precipitated salts on the surface of Ceres.

Chapter 5

5   Conclusions

The purpose of this study was to determine if SAR can be a useful tool for remote predictive geological mapping. Because traditional geological field mapping techniques are expensive, time consuming, and often unfeasible in remote locations, it is important to explore new methods of acquiring data remotely. In the past few decades, satellite spectroscopy has become a popular tool for predicting and identifying geological materials. In contrast, very few studies have incorporated SAR techniques into the geological mapping process. By exploiting the physical properties of salt minerals, (i.e. that they are softer than other rocks, more soluble than other rocks, and subsequently erode more readily producing rough surfaces), this study has demonstrated one geological application of SAR. Specifically, we aimed to determine the radar characteristics of anhydrite and gypsum salt diapirs in the Canadian High Arctic.

Remote predictive geological mapping is most effective when multiple datasets are used. In this study, we primarily used Landsat-8 VNIR and ASTER TIR composite images to manually map salt exposures on Axel Heiberg Island. The VNIR data have better spatial resolution (30 m/pixel) than the TIR (90 m/pixel) data but have more gaps from topographic shadowing than the TIR images. Therefore, detailed mapping was performed using the VNIR images, and the TIR images were used to fill in any gaps. After salt was mapped using the spectral data, the average circular polarization ratio values of the salt regions were extracted in terrain corrected C-Band and L-Band SAR imagery.

The hypothesis for this study was that salt diapirs would appear rough in SAR (i.e. have a greater CPR value than surrounding sedimentary rocks) because of the physical properties of gypsum and anhydrite. The remote data show that salt diapirs appear rough in both C-Band (5.6 cm) and L-Band (23 cm) SAR. These observations were confirmed during ground truth exercises which revealed that the diapirs on Axel Heiberg Island are rough from the millimeter to meter scale. However, the initial hypothesis did not account for secondary salt minerals precipitating downstream of diapirs. It was found that salt exposures mapped through spectroscopy have bimodal SAR characteristics – diapiric salt

is rough in SAR, whereas remobilized secondary salts are smooth in SAR. These results show that SAR can be used to differentiate the genetic origins of salt minerals based on their surface roughness. Because both surficial secondary salts and diapiric salts are highlighted in the VNIR and TIR spectral images, it is important to have a means to differentiate between them. Salt diapirs are a bedrock unit, whereas secondary salts are forming on surficial sediments. Therefore, SAR can be used as a tool to map salt diapirs, in conjunction with spectral techniques used for bedrock mapping. Furthermore, when combined with spectroscopy, it can be used to map the radar-smooth secondary salts for studying hydrological and environmental applications of salt ion transport pathways.

Remote predictive mapping therefore increases the ability to look for natural resources at lowered costs, and with decreased risk of human life. This study has provided a new method of using orbital imagery for regional geological mapping of salt diapirs – a key target in preliminary resource exploration. Because salt diapirs frequently provide traps for petroleum reservoirs and lead-zinc ore deposits, the findings of this study are applicable to resource exploration in the energy and mining industries. It would be beneficial for companies and government agencies to utilize SAR data when performing remote mapping in regions with known, or suspected, diapirism. This study also has implications for planetary research. Salt minerals are found on multiple planets and moons, with potential diapiric processes occurring there as well. Because it is not yet feasible to send human explorers to other planetary bodies, it is important to develop new applications for remote sensing methods to best understand the materials and processes occurring within our solar system. International space agencies should consider including SAR instruments on future planetary spacecraft.

5.1 Limitations and Future Work

In the field, analyses were limited by weather and helicopter availability. The field team had intended on ground truthing the composition of the "salt island" identified through spectral imagery in chapter three, but this was not feasible during our timeline. Similarly, the team had intended to land on the "anomalous radar-rough" region in the Isachsen Formation, also mentioned in chapter three, but due to inclement weather only a fly-by was permissible. We were unable to sample this radar-rough material, nor accurately

measure the size and distribution of materials on its surface beyond observations from the helicopter – though these materials did appear consistent with the scale of roughness observable by RADARSAT-2 C-Band SAR. Finally, the team had intended on incorporating a high-resolution backpack LiDAR system for measuring diapiric surface roughness down to the mm scale, but our system failed a few days from the start of the expedition. It would be beneficial for a future field team to confirm the presence of gypsum or anhydrite on the "salt island", as well as to ground-truth the surface grain size distribution via hiked traverse on the "anomalous radar-rough" region.

Future work may also measure sets of two-dimensional roughness profiles to calculate precise roughness parameters over the salt diapirs. Such measurements would provide a stronger quantitative assessment of diapiric surface roughness to compare with the remote imagery and evaluate differences in roughness parameters across different geomorphological slopes of the salt domes. These could then be compared to previous works performed around the Haughton Impact Structure on Devon Island in the Canadian High Arctic (Choe 2017; Zanetti et al. 2017). Whereas on Axel Heiberg Island most roughness is occurring from the disintegration of salt diapirs, on Devon Island most roughness is a product of cryoturbation and other periglacial processes breaking apart the bedrock. It would be possible to differentiate between units on either island using a combination of spectral imagery and SAR. Within the Haughton Impact Structure, because of their softness, "evaporite-rich units weathered to fine-grained plains," (Choe 2017) and reflected predominantly single-bounce scattering in RADARSAT-2 imagery (i.e. were smooth in C-Band). In contrast, the harder carbonate bedrock had broken apart into angular cobbles and blocky boulders that produced volumetric scattering (i.e. moderately rough in C-Band). This is opposite what we see on Axel Heiberg Island, where the evaporite-rich diapirs are more recently eroded than on Devon Island, and are breaking apart into larger fragments.

This study used C-Band (5.6 cm) and L-Band (23 cm) SAR, so the polarimetric radar images only characterized roughness at these two scales. Unfortunately, because of layover and foreshortening issues with the PALSAR-1 L-Band images, these data may not be as reliable as the RADARSAT-2 data. For planetary analogue work, it may also be

beneficial to characterize the diapiric surface roughness in P-Band SAR (30-100 cm). P-Band has been suggested as a strong candidate SAR wavelength for a Mars orbiter, due to its ability to penetrate through the veneer of Martian dust (Campbell et al. 2004; Paillou et al. 2006). Additionally, only circular polarization ratio image products were produced in the scope of this study. CPR images require fully polarimetric SAR data. Future studies may wish to explore the capabilities of dual-polarimetric SAR, by characterizing the radar properties of salt in cross-polarization imagery. Cross-polarization images are the ratio of the horizonal polarized backscatter intensity (σ^o_{vh}) over vertically polarized backscatter intensity (σ^o_{vv}) (Equation 11) and only require the radar to transmit in one polarization direction (Oh 2004).

$$\frac{\sigma^o_{vh}}{\sigma^o_{vv}} \qquad\qquad (Equation\ 11)$$

Future work can compare the radar characteristics of salt exposures in quad-polarimetric SAR versus dual-polarimetric SAR. This would compare the utility between fully polarimetric SAR products, or if equally useful results can be achieved using fewer polarization modes.

Finally, the powder XRD samples revealed the presence of thenardite and mirabilite in the secondary salt deposits. These salts are characteristic of the mineralogy of Axel Heiberg Island's perennial springs. Future work may investigate the orbital spectral properties of these minerals to see if it may be possible to isolate them from gypsum and anhydrite during preliminary spectral mapping. This may allow future researchers to focus exploration exclusively on diapiric or perennial spring salts depending on their research interests.

Previous field mapping exercises have produced substantial work in characterizing the main geological units on Axel Heiberg Island (Harrison et al. 2015). These works have provided a regional tectonic context for the development of a wall-and-basin structure in the Sverdrup Basin and the formation of a subsurface salt canopy. The tectonic context has provided a chronological history for the basin structural development and rise of abundant salt diapirs exposed on the island (Jackson and Harrison 2006). With recent

advancements in orbital spectroscopy, and the new implementation of SAR for geological mapping, these maps can be refined, and detailed mapping can be expanded beyond the WABS region. Remote mapping of surface salts and salt domes can be extended across Axel Heiberg Island, the Sverdrup Basin, and to inaccessible and remote countries as well as other planets and moons.

References

Andersen, D.T., Pollard, W.H., McKay, C.P., and Heldmann, J. 2002. Cold springs in permafrost on Earth and Mars. Journal of Geophysical Research: Planets, **107**. Wiley Online Library pp. 66-74.

Antenucci, J.C., Antenucci, R., and Smith, J.W. 2010. Private Sector Applications. *In* Manual of Geospatial Science and Technology, Second Edi. *Edited by* J.D. Bossler, J.B. Campbell, R.B. McMaster, and C. Rizos. pp. 761–776.

Battler, M.M., Osinski, G.R., and Banerjee, N.R. 2013. Mineralogy of saline perennial cold springs on Axel Heiberg Island, Nunavut, Canada and implications for spring deposits on Mars. Icarus, **224**: 364–381. doi:10.1016/j.icarus.2012.08.031

Boerner, W.-M., Yan, W.-L., Xi, A.-Q., and Yamaguchi, Y. 1992. Basic concepts of radar polarimetry. *In* Direct and Inverse Methods in Radar Polarimetry. Springer. pp. 155–245.

Bragg, W.H. 1915. Bakerian Lecture: X-Rays and Crystal Structure. Philosophical Transactions of the Royal Society of London. Series A, Containing Papers of a Mathematical or Physical Character, **215**: 253–274. The Royal Society. Available from http://www.jstor.org/stable/91108.

Buczkowski, D.L., Schmidt, B.E., Williams, D.A., Mest, S.C., Scully, J.E.C., Ermakov, A.I., Preusker, F., Schenk, P., Otto, K.A., Hiesinger, H., and others. 2016. The geomorphology of Ceres. Science, **353**: 1004-1010. American Association for the Advancement of Science.

Campbell, B.A., Maxwell, T.A., and Freeman, A. 2004. Mars orbital synthetic aperture radar: Obtaining geologic information from radar polarimetry. Journal of Geophysical Research: Planets, **109**. Wiley Online Library.

Campbell, J.B., and Wynne, R.H. 2011. Introduction to remote sensing. Cambridge University Press. pp. 1-643

Carlson, R.W., Kargel, J.S., Douté, S., Soderblom, L.A., and Dalton, J.B. 2007. Io's surface composition. *In* Io After Galileo: A New View of Jupiter's Volcanic Moon. Springer Berlin Heidelberg, Berlin, Heidelberg. pp. 193–229. doi:10.1007/978-3-540-48841-5_9.

Carrier, W.D., Olhoeft, G.R., and Mendell, W. 1991. Physical properties of the lunar surface. Lunar sourcebook: 475–594. Cambridge University Press, Cambridge.

Choe, B. 2017. Polarimetric Synthetic Aperture Radar (SAR) Application for Geological Mapping and Resource Exploration in the Canadian Arctic. University of Western Ontario. Available from https://ir.lib.uwo.ca/etd/5133.

Clark, B.C., Morris, R. V, McLennan, S.M., Gellert, R., Jolliff, B., Knoll, A.H., Squyres, S.W., Lowenstein, T.K., Ming, D.W., Tosca, N.J., Yen, A., Christensen, P.R., Gorevan, S., Brückner, J., Calvin, W., Dreibus, G., Farrand, W., Klingelhoefer, G., Waenke, H., Zipfel, J., Bell, J.F., Grotzinger, J., McSween, H.Y., and Rieder,

R. 2005. Chemistry and mineralogy of outcrops at Meridiani Planum. Earth and Planetary Science Letters, **240**: 73–94. doi:https://doi.org/10.1016/j.epsl.2005.09.040.

De Sanctis, M.C., Raponi, A., Ammannito, E., Ciarniello, M., Toplis, M.J., McSween, H.Y., Castillo-Rogez, J.C., Ehlmann, B.L., Carrozzo, F.G., Marchi, S., Tosi, F., Zambon, F., Capaccioni, F., Capria, M.T., Fonte, S., Formisano, M., Frigeri, A., Giardino, M., Longobardo, A., Magni, G., Palomba, E., McFadden, L.A., Pieters, C.M., Jaumann, R., Schenk, P., Mugnuolo, R., Raymond, C.A., and Russell, C.T. 2016. Bright carbonate deposits as evidence of aqueous alteration on (1) Ceres. Nature, **536**: 54. Nature Publishing Group, a division of Macmillan Publishers Limited. All Rights Reserved. Available from http://dx.doi.org/10.1038/nature18290.

Dundas, C.M., McEwen, A.S., Diniega, S., Hansen, C.J., Byrne, S., and McElwaine, J.N. 2017. The formation of gullies on Mars today. Geological Society, London, Special Publications, **467**: SP467--5. Geological Society of London.

Elachi, C. 1988. Spaceborne radar remote sensing: applications and techniques. *In* New York, IEEE Press. IEEE Press, New York.

Elachi, C., and Van Zyl, J.J. 2006. Introduction to the physics and techniques of remote sensing. John Wiley & Sons.

Embry, A.F., Powell, T.G., and Mayr, U. 1991. Petroleum resources, Arctic Islands. Geology of the Innutian Orogen and Arctic Platform of Canada and Greenland (Ed. by HP Trettin). Geol. Surv. Can., Geology of Canada, **3**: 517–525.

Farr, T.G. 1993. Guide to Magellan Image Interpretation. Jet Propulsion Laboratory, Cap. Radar Interactions With Geologic Surfaces,: 45–56.

Fiol, L., Fornós, J.J., and Ginés, A. 1996. Effects of biokarstic processes on the development of solutional rillenkarren in limestone rocks. Earth Surface Processes and Landforms, **21**: 447–452. doi:10.1002/(SICI)1096-9837(199605)21:5<447::AID-ESP607>3.0.CO;2-X.

Fox-Powell, M.G., Osinski, G.R., Gunn, M., Applin, D., Cloutis, E., and Cousins, C.R. 2018. Low-Temperature Hydrated Salts on Axel Heiberg Island, Arctic Canada, as an Analogue for Europa. *In* 49th Lunar and Planetary Science Conference. Lunar and Planetary Institute, Houston. Abstract #2564. Available from http://www.lpi.usra.edu/meetings/lpsc2018/pdf/2564.pdf.

Franceschetti, G., and Lanari, R. 1999. Synthetic aperture radar processing. CRC press.

Freeman, A., and Durden, S.L. 1998. A three-component scattering model for polarimetric SAR data. IEEE Transactions on Geoscience and Remote Sensing, **36**: 963–973. IEEE.

Gupta, R.P. 2017. Remote sensing geology. Springer. Berlin. 1-427.

Harrison, J.C., and Jackson, M.P.A. 2014a. Exposed evaporite diapirs and minibasins above a canopy in central Sverdrup Basin, Axel Heiberg Island, Arctic Canada. Basin Research, **26**: 567–596. doi:10.1111/bre.12037.

Harrison, J.C., and Jackson, M.P.A. 2014b. Tectonostratigraphy and allochthonous salt tectonics of Axel Heiberg Island, central Sverdrup Basin, Arctic Canada. Geological Survey of Canada, Bulletin 607; Bureau of Economic Geology Report of Investigations No. 279. doi:10.4095/293840.

Harrison, J.C., Le, M., Lynds, T., Ford, A., Balkwill, H.R., Thorsteinsson, R., and Okulitch, A. V. 2015. Geology, tectonic assemblage map of Massey Sound, Amund Ringnes Island, and surrounding islands, Nunavut. Natural Resources Canada. doi:10.4095/292824.

Hawthorne, F.C., and Ferguson, R.B. 1975. Anhydrous sulphates; II, Refinement of the crystal structure of anhydrite. The Canadian Mineralogist, 13: 289–292. Mineralogical Association of Canada.

Hudec, M.R., and Jackson, M.P.A. 2006. Advance of allochthonous salt sheets in passive margins and orogens. AAPG bulletin, **90**: 1535–1564. American Association of Petroleum Geologists.

ISO, E.N. 2002. 14688-1: 2002: Geotechnical investigation and testing--Identification and classification of soil--Part 1: Identification and description. International Organization for Standardization, Geneva.

Jackson, M.P.A., and Harrison, J.C. 2006. An allochthonous salt canopy on Axel Heiberg Island, Sverdrup Basin, Arctic Canada. Geology, **34**: 1045–1048. doi:10.1130/G22798A.1.

Jackson, M.P.A., and Hudec, M.R. 2017. Salt Tectonics: Principles and Practice. Cambridge University Press.

Kargel, J.S., Kirk, R.L., Fegley, B., and Treiman, A.H. 1994. Carbonate-Sulfate Volcanism on Venus? Icarus, **112**: 219–252. doi:https://doi.org/10.1006/icar.1994.1179.

König, M., Winther, J.-G., and Isaksson, E. 2001. Measuring snow and glacier ice properties from satellite. Reviews of Geophysics, **39**: 1–27. doi:10.1029/1999RG000076.

Lane, M.D., and Christensen, P.R. 1999. Spectral behavior of hematite at visible/near infrared and midinfrared wavelengths. NASA Technical Reports Server.

Lee, J.-S., and Pottier, E. 2009. Polarimetric radar imaging: from basics to applications. CRC press.

McEwen, A.S., Ojha, L., Dundas, C.M., Mattson, S.S., Byrne, S., Wray, J.J., Cull, S.C., Murchie, S.L., Thomas, N., and Gulick, V.C. 2011. Seasonal Flows on Warm Martian Slopes. Science, **333**: 740 LP-743. Available from http://science.sciencemag.org/content/333/6043/740.abstract.

McLennan, S.M., Bell, J.F., Calvin, W.M., Christensen, P.R., Clark, B.C., de Souza, P.A., Farmer, J., Farrand, W.H., Fike, D.A., Gellert, R., Ghosh, A., Glotch, T.D., Grotzinger, J.P., Hahn, B., Herkenhoff, K.E., Hurowitz, J.A., Johnson, J.R., Johnson, S.S., Jolliff, B., Klingelhöfer, G., Knoll, A.H., Learner, Z., Malin, M.C., McSween, H.Y., Pocock, J., Ruff, S.W., Soderblom, L.A., Squyres, S.W., Tosca,

N.J., Watters, W.A., Wyatt, M.B., and Yen, A. 2005. Provenance and diagenesis of the evaporite-bearing Burns formation, Meridiani Planum, Mars. Earth and Planetary Science Letters, **240**: 95–121. doi:https://doi.org/10.1016/j.epsl.2005.09.041.

McMaster, R.B., and Manson, S.M. 2010. Geographic information systems and science. *In* Manual of Geospatial Science and Technology, Second Edi. *Edited by* J.D. Bossler, J.B. Campbell, R.B. McMaster, and C. Rizos. CRC Press. pp. 513–523.

Mockert, D. 2010. Geographic Information Technology in State Governments of the United States. *In* Manual of Geospatial Science and Technology, Second Edition, Second Edi. *Edited by* J.D. Bossler, J.B. Campbell, R.B. McMaster, and C. Rizos. CRC Press. pp. 713–732.

Mueller, D.R., and Pollard, W.H. 2004. Gradient analysis of cryoconite ecosystems from two polar glaciers. Polar Biology, 27: 66–74.

Nathues, A., Platz, T., Thangjam, G., Hoffmann, M., Mengel, K., Cloutis, E.A., Le Corre, L., Reddy, V., Kallisch, J., and Crown, D.A. 2017. Evolution of Occator crater on (1) Ceres. The Astronomical Journal, **153**: 112. IOP Publishing.

Neish, C.D., Bussey, D.B.J., Spudis, P., Marshall, W., Thomson, B.J., Patterson, G.W., and Carter, L.M. 2011. The nature of lunar volatiles as revealed by Mini-RF observations of the LCROSS impact site. Journal of Geophysical Research: Planets, **116**: n/a--n/a. doi:10.1029/2010JE003647.

Neish, C.D., and Carter, L.M. 2014. Planetary Radar. *In* Encyclopedia of the Solar System. pp. 1133–1159. doi:10.1016/B978-0-12-415845-0.00053-0.

Neish, C.D., Hamilton, C.W., Hughes, S.S., Nawotniak, S.K., Garry, W.B., Skok, J.R., Elphic, R.C., Schaefer, E., Carter, L.M., Bandfield, J.L., Osinski, G.R., Lim, D., and Heldmann, J.L. 2017. Terrestrial analogues for lunar impact melt flows. Icarus, **281**: 73–89. doi:10.1016/j.icarus.2016.08.008.

Nesse, W.D. 2012. Introduction to Mineralogy: Second Edition. Oxford University Press, New York.

Oh, Y. 2004. Quantitative retrieval of soil moisture content and surface roughness from multipolarized radar observations of bare soil surfaces. IEEE Transactions on Geoscience and Remote Sensing, **42**: 596–601. IEEE.

Ojha, L., Wilhelm, M.B., Murchie, S.L., McEwen, A.S., Wray, J.J., Hanley, J., Massé, M., and Chojnacki, M. 2015. Spectral evidence for hydrated salts in recurring slope lineae on Mars. Nature Geoscience, **8**: 829-832. Nature Publishing Group.

Paillou, P., Lasne, Y., Heggy, E., Malézieux, J.-M., and Ruffié, G. 2006. A study of P-band synthetic aperture radar applicability and performance for Mars exploration: Imaging subsurface geology and detecting shallow moisture. Journal of Geophysical Research: Planets, **111**: n/a-n/a. doi:10.1029/2005JE002528.

Pedersen, B.F., and Semmingsen, D. 1982. Neutron diffraction refinement of the structure of gypsum, CaSO4. 2H2O. Acta Crystallographica Section B: Structural

Crystallography and Crystal Chemistry, 38: 1074–1077. International Union of Crystallography.

Phillips, C.B., and Pappalardo, R.T. 2014. Europa clipper mission concept: exploring Jupiter's ocean moon. Eos, Transactions American Geophysical Union, **95**: 165–167. Wiley Online Library.

Ramberg, H. 1981. Gravity, deformation, and the earth's crust: In theory, experiments, and geological application. Academic press. 1-452.

Scully, J.E.C., Buczkowski, D.L., Schmedemann, N., Raymond, C.A., Castillo-Rogez, J.C., King, S.D., Bland, M.T., Ermakov, A.I., O'Brien, D.P., Marchi, S., Longobardo, A., Russell, C.T., Fu, R.R., and Neveu, M. 2017. Evidence for the Interior Evolution of Ceres from Geologic Analysis of Fractures. Geophysical Research Letters, **44**: 9564–9572. doi:10.1002/2017GL075086.

Stenson, R.E., and Ford, D.C. 1993. Rillenkarren on gypsum in Nova Scotia. Geographie physique et Quaternaire, **47**: 239–243. Les Presses de l'Université de Montréal.

Suppe, J. 1985. Principles of structural geology. Prentice Hall. 1-537.

Thompson, A.A., and McLeod, I.H. 2004. The radarsat-2 sar processor. Canadian journal of remote sensing, **30**: 336–344. Taylor & Francis.

Warren, J.K. 2006. Evaporites: sediments, resources and hydrocarbons. Springer Science & Business Media. 1-1035.

Williamson, M.-C., Percival, J.B., Behnia, P., Harris, J.R., Peterson, R.C., Froome, J., Fenwick, L., Rainbird, R.H., Bédard, J.H., McNeil, R.J., Day, S.J., Kingsbury, C.G., Grunsky, E., McCurdy, M.W., Sheperd, J., Hillary, E.M., and Buller, G. 2014. Environmental and economic impact of oxide-sulphide gossans, Northwest Territories and Nunavut. *In* Geological Survey of Canada, Open File. Natural Resources Canada. doi:10.4095/293922.

Williamson, M.-C., Smyth, H.R., Peterson, R.C., and Lavoie, D. 2011. Comparative geological studies of volcanic terrain on Mars: Examples from the Isachsen Formation, Axel Heiberg Island, Canadian High Arctic. Geological Society of America Special Papers, **483**: 249–261.

Zanetti, M., Neish, C.D., Kukko, A., Choe, B.-H., Osinski, G.R., and Mahathantila, N. 2017. Surface Roughness and Radar Scattering Properties of Periglacial Terrain: Geologic Applications of Personal Mobile LiDAR Scanning. *In* 48th Lunar and Planetary Science Conference. Lunar and Planetary Institute, Houston. Abstract #2775. Available from https://www.hou.usra.edu/meetings/lpsc2017/pdf/2775.pdf

Appendices

Appendices A-D are the data for the acquired from the zonal CPR statistics for each polygon mapped as salt using the TIR, VNIR, and SWIR spectral data. The XRD data from each of the salt samples are also provided. Appendix E shows the powder XRD results from collected rock and mineral samples during the 2017 field season.

Appendix A: Values of RADARSAT-2 CPR Zonal Statistics for spectrally mapped salt diapirs

SALT EXPOSURE ID	COUNT	AREA (M^2)	MIN CPR	MAX CPR	RANGE	MEAN	STD
0	14334	20664843.9	0.05	1.79	1.74	0.39	0.17
1	444	640099.8	0.06	0.94	0.88	0.32	0.16
2	1003	1445991.2	0.06	1.14	1.08	0.37	0.19
3	191	275358.3	0.09	0.76	0.67	0.27	0.12
4	125	180208.3	0.05	0.55	0.50	0.19	0.08
5	129	185974.9	0.02	0.87	0.85	0.24	0.18
6	190	273916.6	0.09	0.84	0.75	0.39	0.13
7	345	497374.9	0.07	0.82	0.75	0.37	0.15
8	37	53341.7	0.34	0.95	0.61	0.57	0.12
9	66	95150.0	0.12	0.57	0.45	0.32	0.11
10	129	185974.9	0.17	1.14	0.97	0.59	0.23
11	560	807333.1	0.03	1.26	1.23	0.33	0.20
12	76	109566.6	0.11	0.95	0.84	0.38	0.18
13	207	298424.9	0.13	0.59	0.46	0.31	0.09
14	2157	3109674.1	0.03	1.17	1.14	0.26	0.15

15	158	227783.3	0.02	0.82	0.80	0.24	0.14
16	60	86500.0	0.14	0.57	0.43	0.32	0.11
17	46	66316.6	0.09	0.30	0.21	0.18	0.05
18	285	410874.9	0.04	0.84	0.80	0.32	0.17
19	115	165791.6	0.09	0.50	0.41	0.18	0.07
20	517	745341.4	0.05	1.78	1.73	0.29	0.18
21	649	935641.4	0.16	1.61	1.46	0.43	0.22
22	2278	3284115.7	0.04	1.36	1.32	0.38	0.18
23	715	1030791.4	0.07	1.10	1.03	0.31	0.17
24	1134	1634849.5	0.06	2.64	2.57	0.59	0.42
25	459	661724.8	0.07	1.70	1.63	0.48	0.28
26	1058	1525282.9	0.11	1.73	1.63	0.55	0.28
27	210	302749.9	0.15	1.45	1.30	0.67	0.25
28	186	268149.9	0.15	1.37	1.22	0.58	0.20
29	1394	2009682.7	0.06	1.81	1.75	0.43	0.20
34	1240	1787666.1	0.15	1.97	1.82	0.61	0.31
35	1328	1914532.8	0.14	2.06	1.92	0.64	0.25
36	967	1394091.3	0.08	1.41	1.33	0.52	0.28
37	155	223458.3	0.23	1.11	0.88	0.60	0.18
38	51	73525.0	0.20	0.68	0.49	0.40	0.12
39	605	872208.1	0.09	1.41	1.32	0.49	0.25
40	255	367624.9	0.16	1.39	1.24	0.46	0.25
41	753	1085574.7	0.10	2.97	2.87	0.88	0.39
42	344	495933.2	0.10	3.39	3.29	0.86	0.46

43	258	371949.9	0.11	1.77	1.66	0.62	0.28
44	81	116775.0	0.12	2.08	1.96	0.82	0.41
45	268	386366.6	0.16	2.20	2.04	0.71	0.38
46	62	89383.3	0.14	1.91	1.77	0.52	0.38
47	186	268149.9	0.17	2.10	1.93	0.97	0.42
48	782	1127383.0	0.15	2.65	2.50	0.62	0.37
49	244	351766.6	0.08	1.97	1.89	0.66	0.37
50	2733	3940073.8	0.03	3.16	3.13	0.44	0.33
51	8118	11703446.6	0.02	2.79	2.77	0.65	0.34
52	447	644424.8	0.07	1.11	1.04	0.36	0.20
60	577	831841.4	0.07	2.31	2.24	0.55	0.38

Appendix B: Values of RADARSAT-2 CPR Zonal Statistics for mapped secondary salts

SALT EXPOSURE ID	COUNT	AREA	MIN	MAX	RANGE	MEAN	STD
5	7227	10418921.9	0.02	1.14	1.12	0.16	0.07
6	1381	1990941.1	0.01	1.46	1.44	0.26	0.21
12	14021	20213602.4	0.03	1.45	1.42	0.25	0.10
13	1336	1926066.1	0.08	0.95	0.87	0.24	0.08
14	721	1039441.4	0.07	0.58	0.51	0.25	0.07
15	337	485841.5	0.11	0.61	0.50	0.25	0.08
16	423	609824.8	0.10	0.53	0.43	0.20	0.06
17	788	1136033.0	0.07	0.50	0.43	0.18	0.07

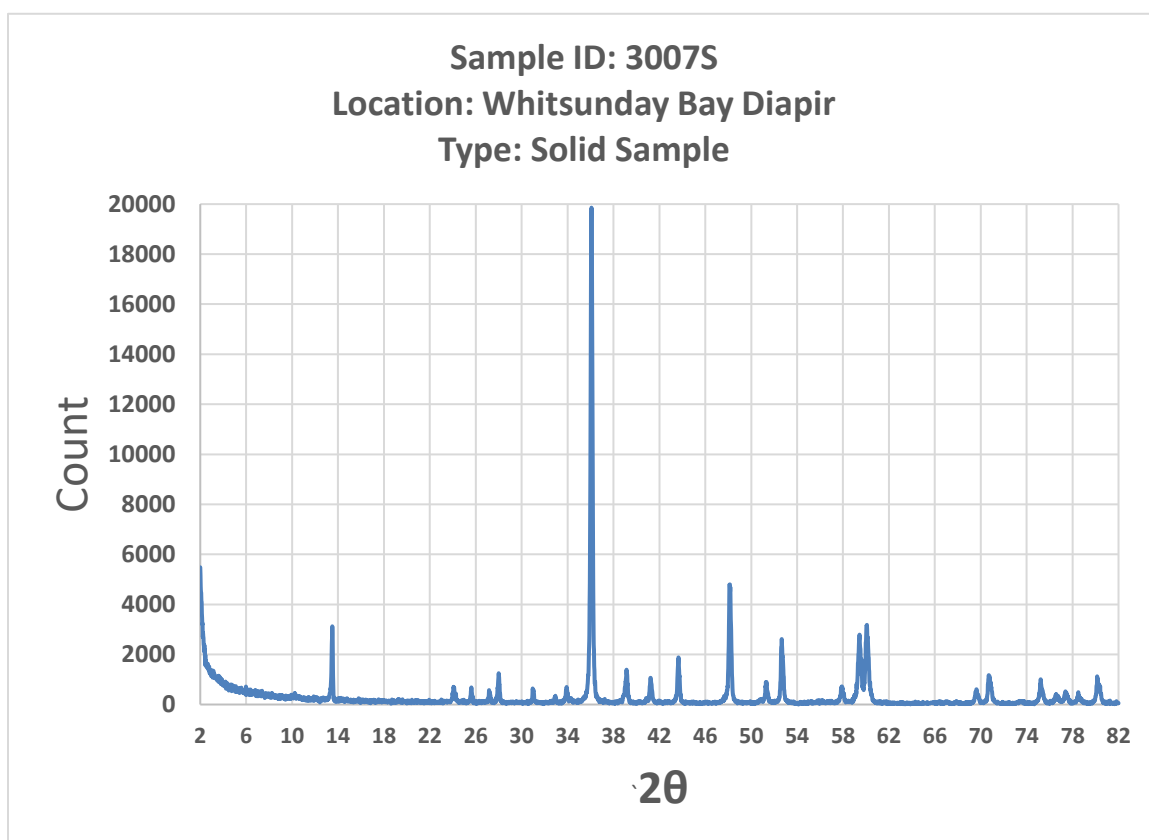|							
18	624	899599.7	0.09	0.53	0.44	0.21	0.07
19	1456	2099066.0	0.05	0.93	0.88	0.21	0.07
20	3865	5572040.0	0.06	0.82	0.76	0.21	0.08
23	462	666049.8	0.18	0.88	0.70	0.38	0.11
24	192	276799.9	0.13	0.54	0.41	0.25	0.07

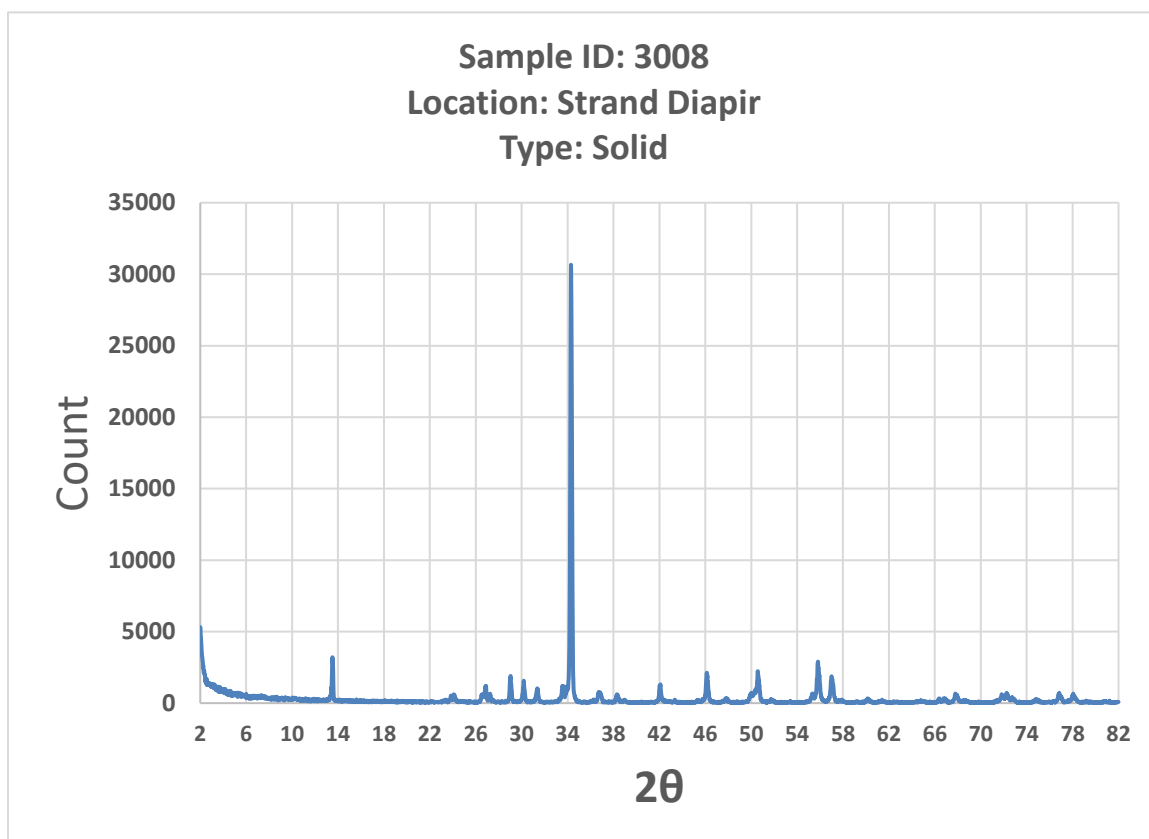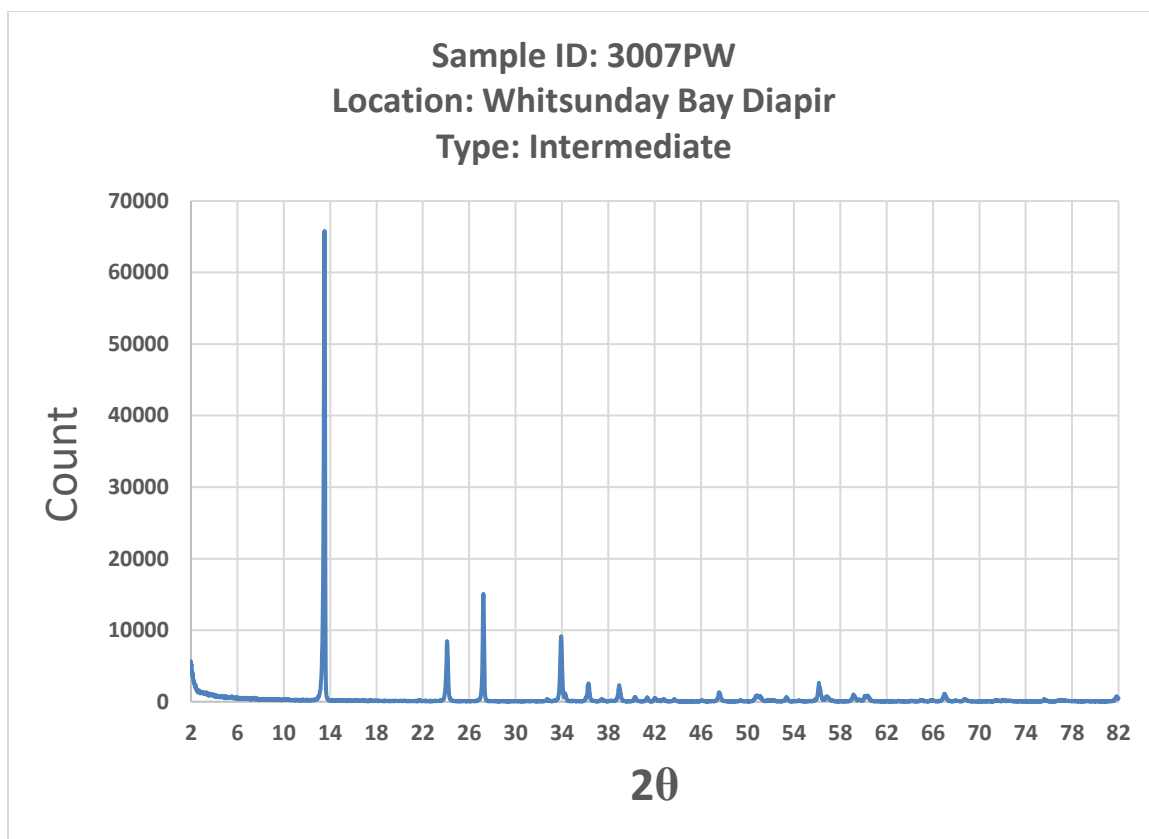## Appendix C: Values of PALSAR-1 CPR Zonal Statistics for mapped Salt Domes (adjusted polygons)

Salt Exposure ID	COUNT	AREA	MIN	MAX	RANGE	MEAN	STD
0	667	1430459.0	0.02	1.62	1.60	0.46	0.27
1	1525	3270540.0	0.01	3.28	3.27	0.46	0.33
2	843	1807911.0	0.03	2.46	2.43	0.44	0.35
3	3018	6472451.0	0.02	4.93	4.91	0.76	0.38
4	213	456803.2	0.25	1.46	1.21	0.66	0.22
5	40	85784.6	0.24	2.04	1.80	0.85	0.46
6	9630	20652653.0	0.03	2.67	2.65	0.67	0.35
7	108	231618.5	0.12	1.92	1.79	0.69	0.31
8	37	79350.8	0.12	1.54	1.42	0.74	0.25
9	31	66483.1	0.32	1.06	0.74	0.66	0.18
10	190	407477.1	0.07	1.31	1.24	0.39	0.20
11	421	902883.4	0.03	1.60	1.57	0.31	0.25
12	458	982234.2	0.06	1.98	1.93	0.50	0.37
13	621	1331807.0	0.02	1.21	1.20	0.37	0.20

14	838	1797188.0	0.09	1.48	1.38	0.62	0.26
15	897	1923721.0	0.01	1.98	1.98	0.45	0.34
16	402	862135.7	0.07	2.17	2.10	0.56	0.31
17	172	368874.0	0.13	2.48	2.35	0.77	0.45
18	233	499695.6	0.11	1.59	1.48	0.55	0.29
19	174	373163.2	0.19	1.68	1.49	0.89	0.30
20	54	115809.3	0.14	1.59	1.45	0.67	0.32
21	183	392464.7	0.06	2.24	2.18	0.86	0.41
22	124	265932.4	0.18	1.02	0.84	0.52	0.19
23	539	1155948.0	0.04	1.75	1.71	0.32	0.23

Appendix D: Values of PALSAR-1 CPR Zonal Statistics for areas mapped as secondary salt deposits (adjusted polygons)
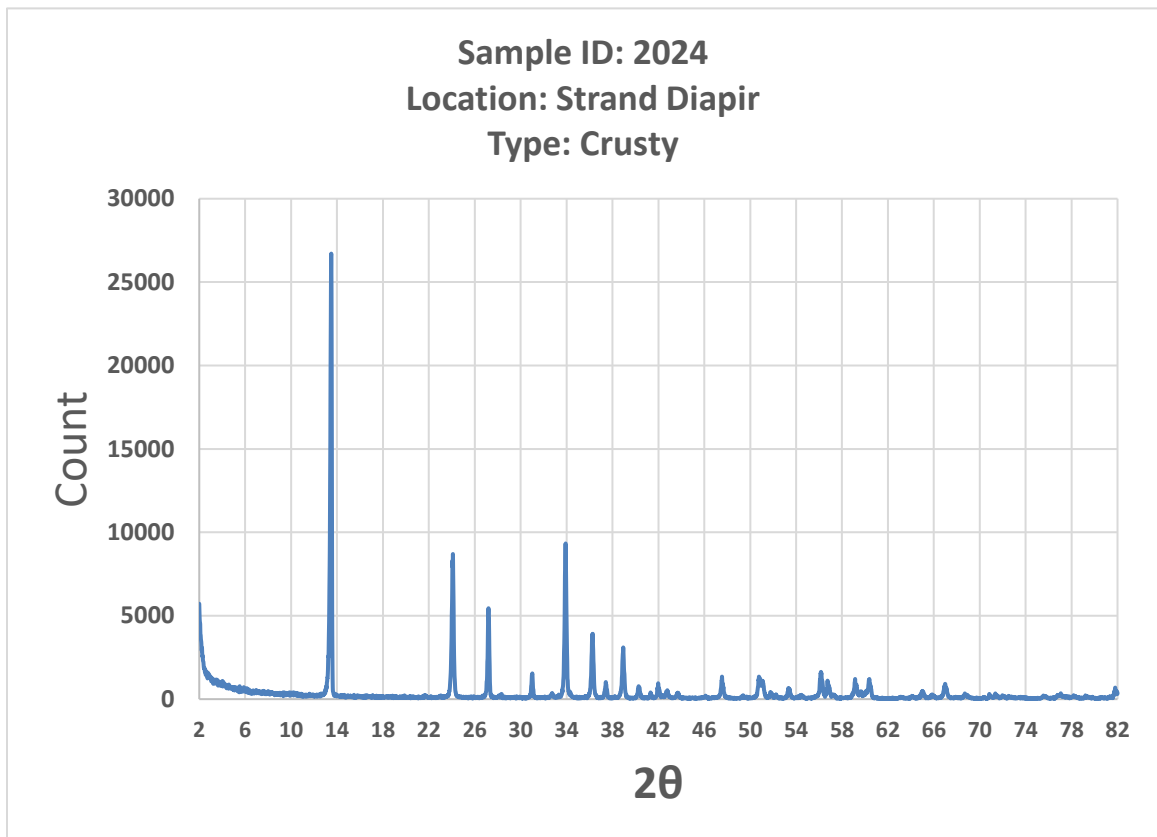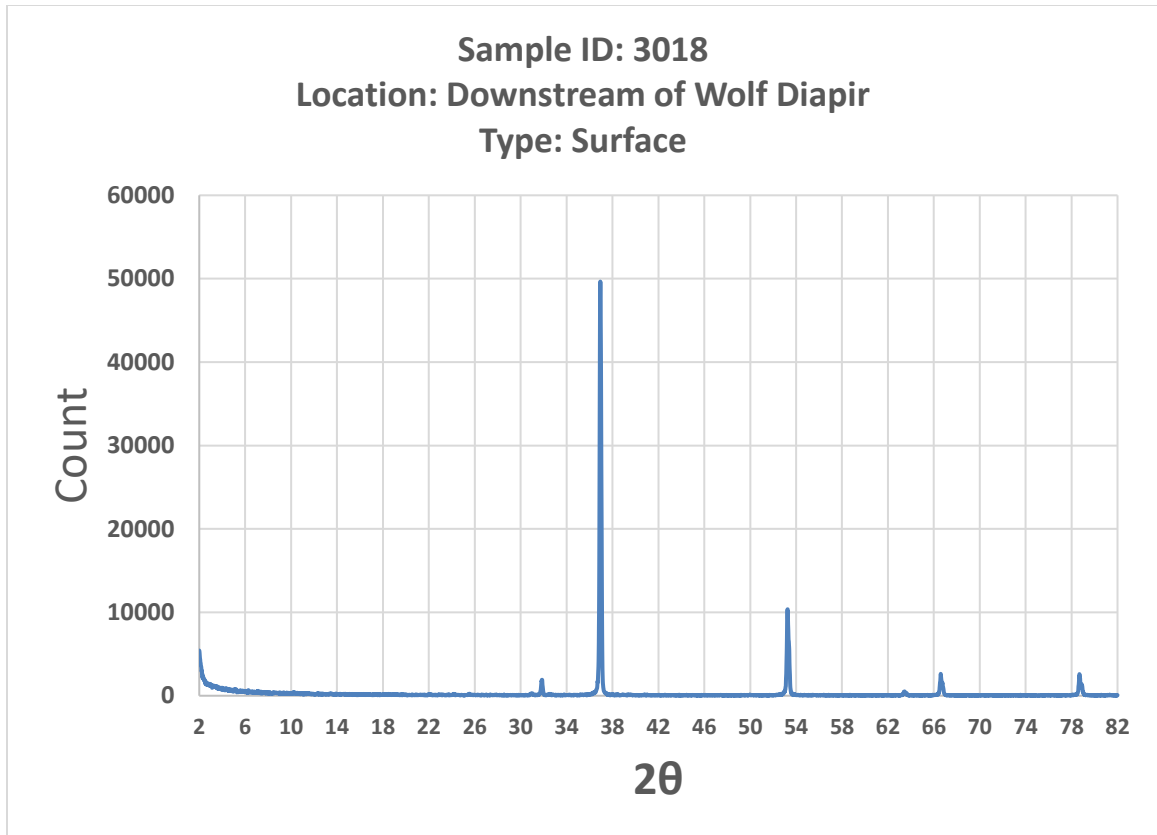
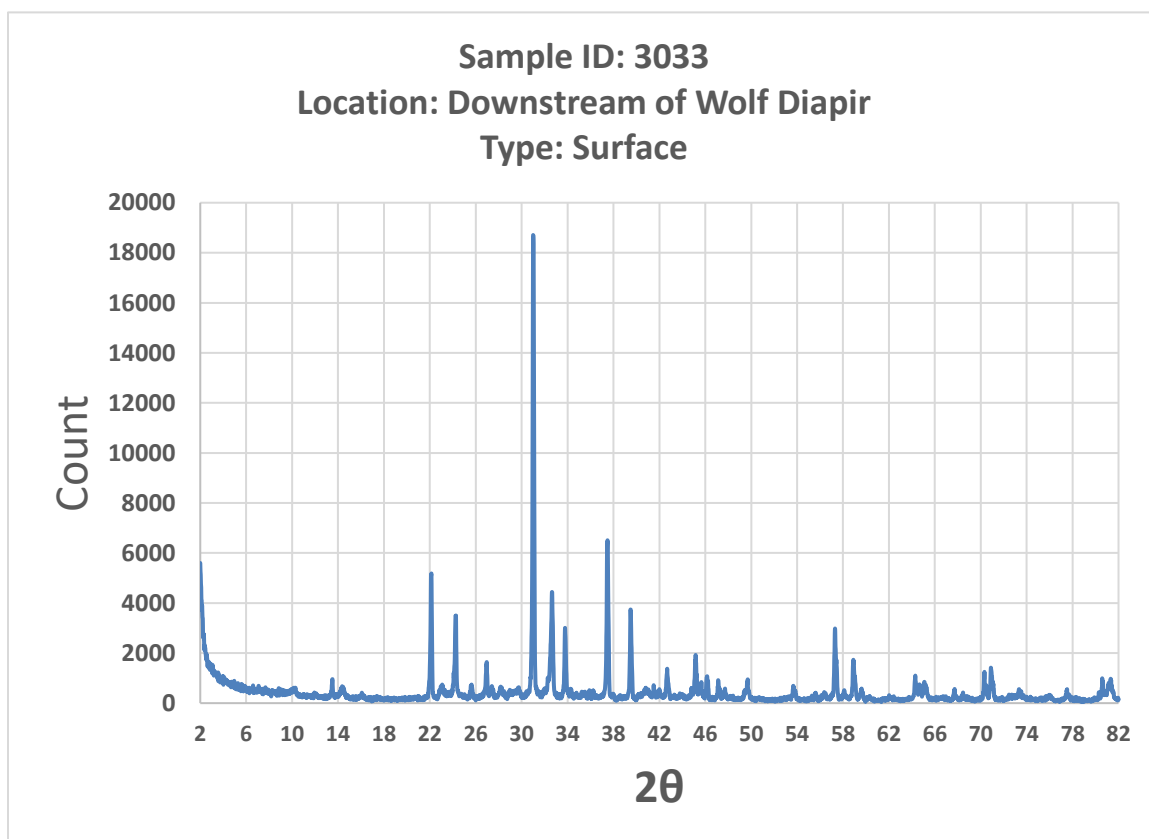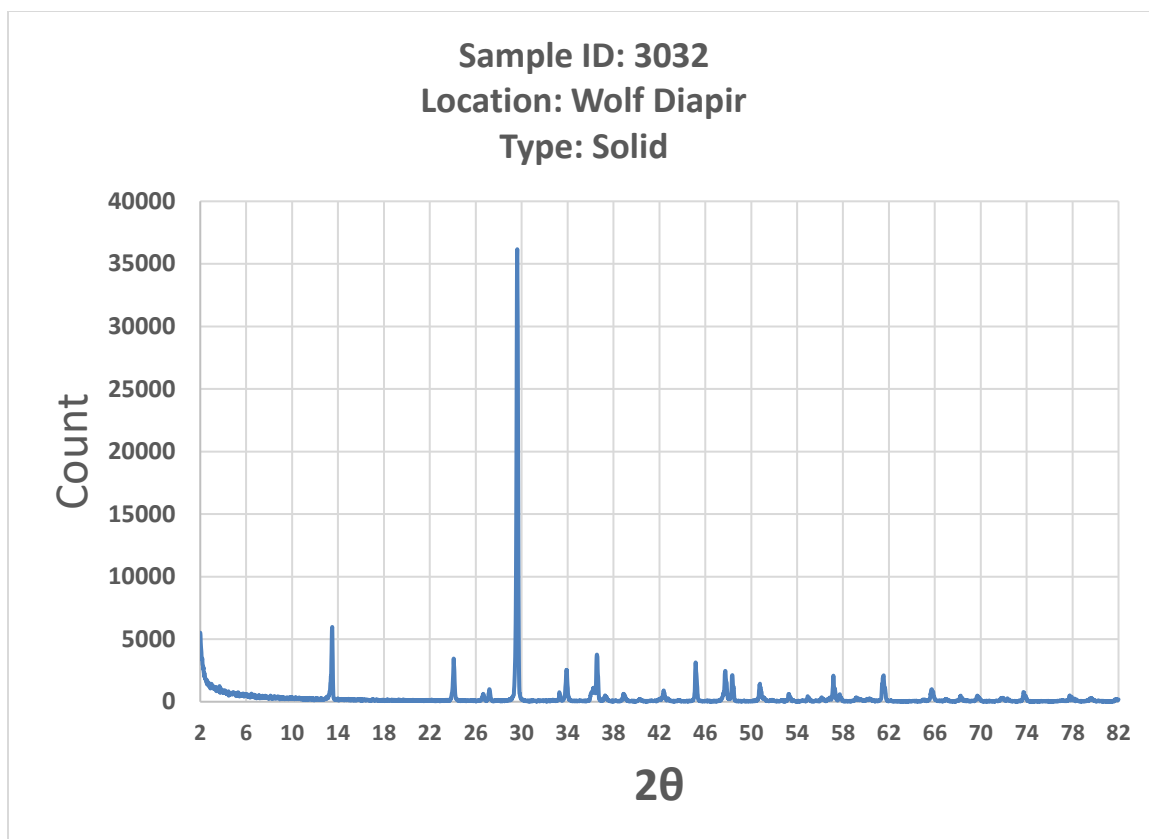| SALT EXPOSURE ID	COUNT	AREA	MIN	MAX	RANGE	MEAN	STD
0	906	1943022.0	0.03	1.62	1.59	0.21	0.18
1	481	1031560.0	0.04	0.79	0.75	0.21	0.10
2	282	604781.7	0.08	0.86	0.78	0.19	0.10
3	533	1143080.0	0.07	0.95	0.88	0.25	0.16
4	1562	3349890.0	0.04	0.93	0.88	0.26	0.11
5	125	268077.0	0.06	0.38	0.32	0.17	0.06
6	14781	31699571.0	0.02	2.19	2.17	0.22	0.14

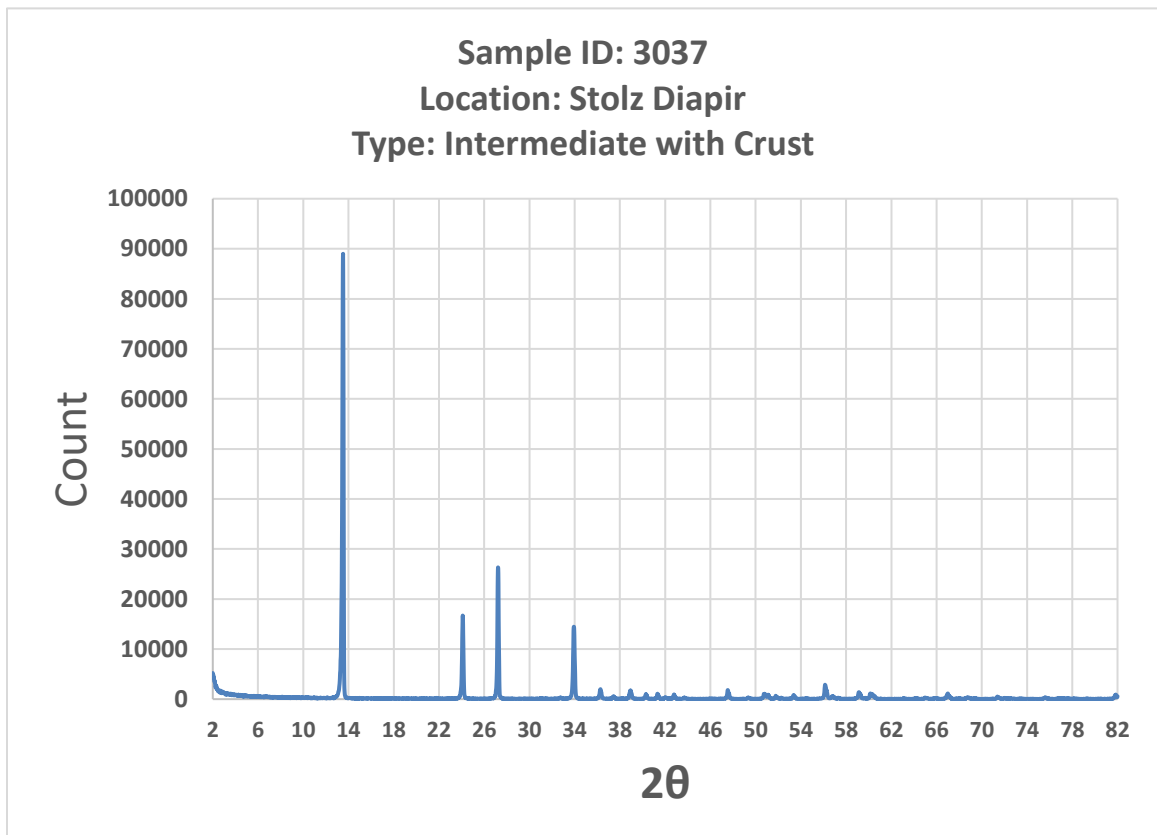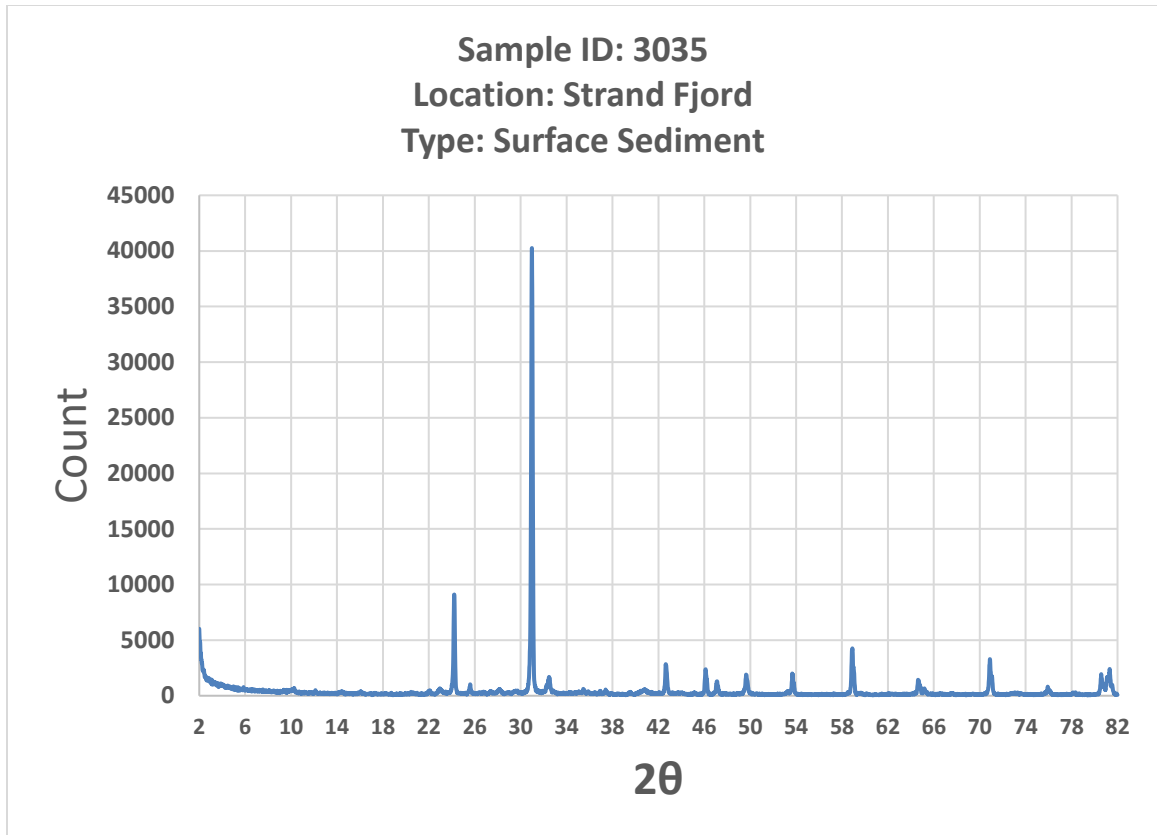**Appendix E: XRD Results for Samples collected from Axel Heiberg Island**

Sample ID: 3007S
Location: Whitsunday Bay Diapir
Type: Solid Sample

Sample ID: 3007PW
Location: Whitsunday Bay Diapir
Type: Intermediate

Sample ID: 3008
Location: Strand Diapir
Type: Solid

Sample ID: 3016
Location: Wolf Diapir
Type: Intermediate

Sample ID: 3017
Location: Colour Peak
Type: Solid

Sample ID: 3018
Location: Downstream of Wolf Diapir
Type: Surface

Sample ID: 2024
Location: Strand Diapir
Type: Crusty

Sample ID: 3032
Location: Wolf Diapir
Type: Solid

Sample ID: 3033
Location: Downstream of Wolf Diapir
Type: Surface

Sample ID: 3035
Location: Strand Fjord
Type: Surface Sediment

Sample ID: 3037
Location: Stolz Diapir
Type: Intermediate with Crust

Sample ID: 3038
Location: Stolz Diapir
Type: Intermediate

Sample ID: 3043
Location: Strand Diapir
Type: Solid

Sample ID: 3047
Location: Colour Peak
Type: Crusty

Sample ID: 3050
Location: Gullies North of Wolf Diapir
Type: Surface

Sample ID: 3051
Location: Wolf Diapir
Type: Crusty

Sample ID: 3052
Location: Whitsunday Bay Diapir
Type: Intermediate

Curriculum Vitae

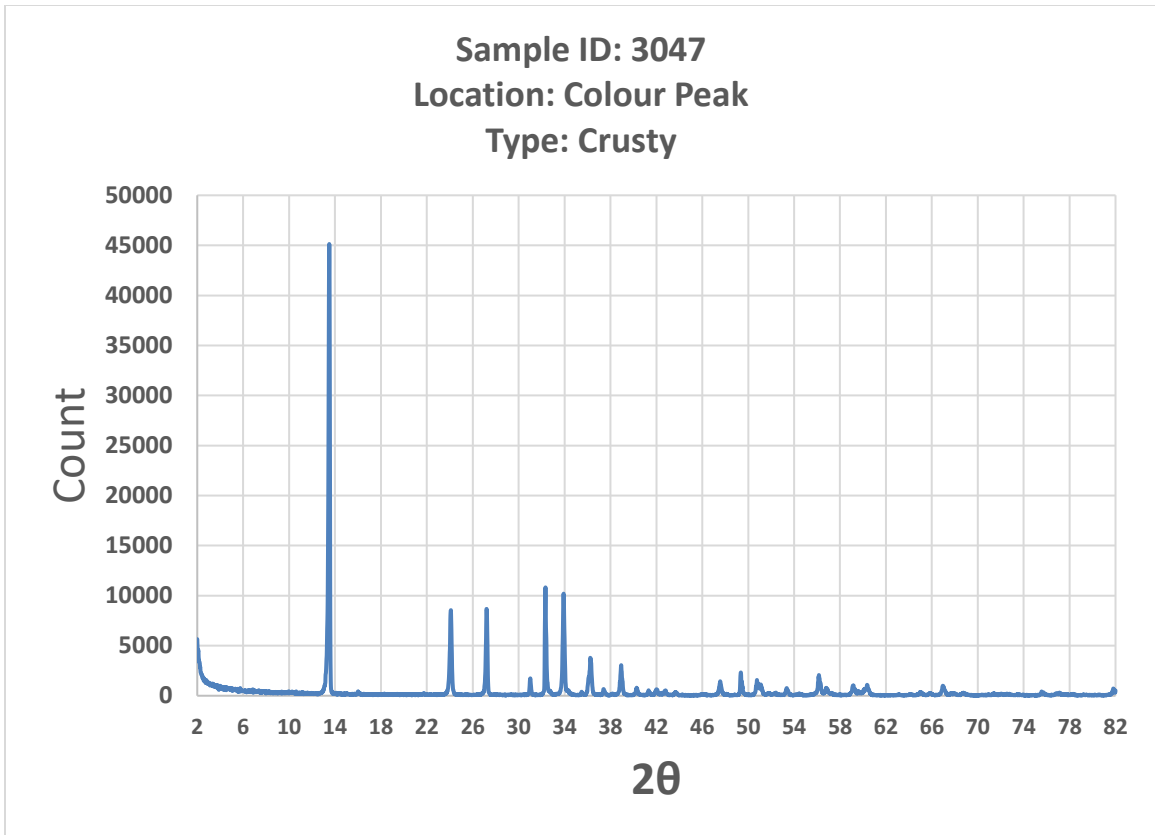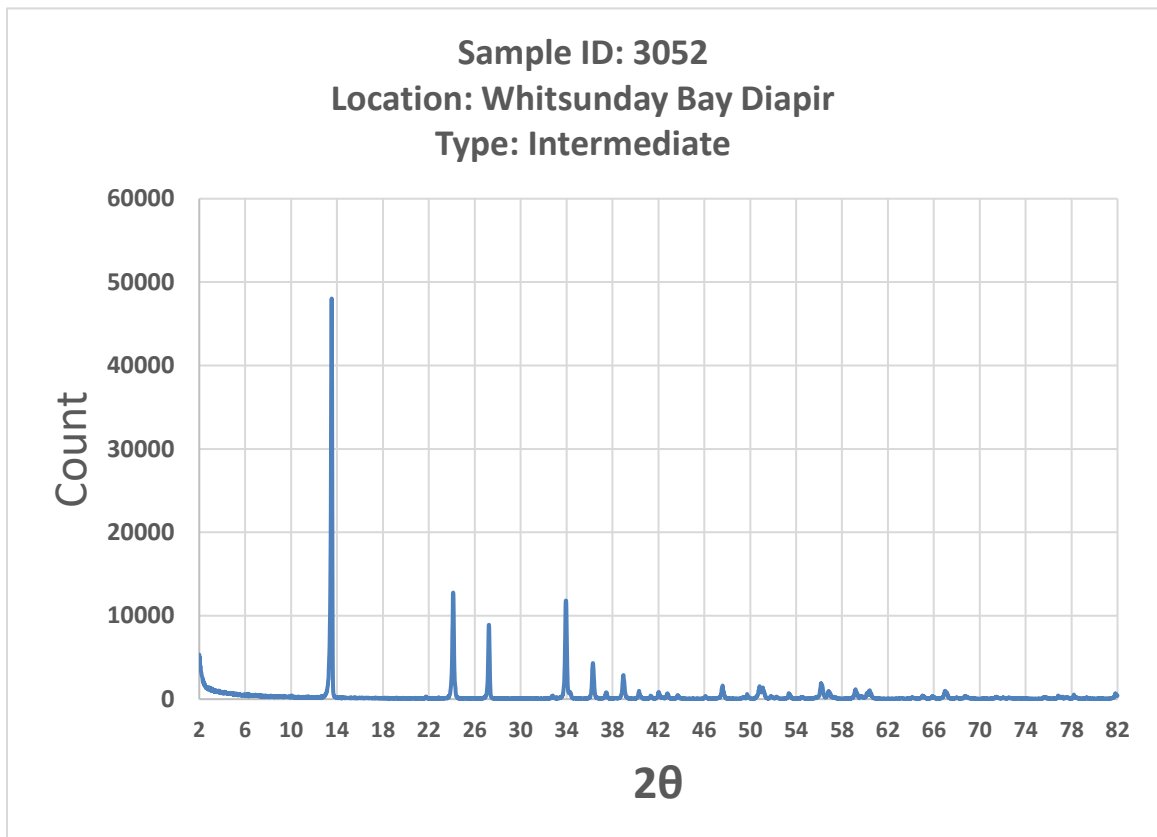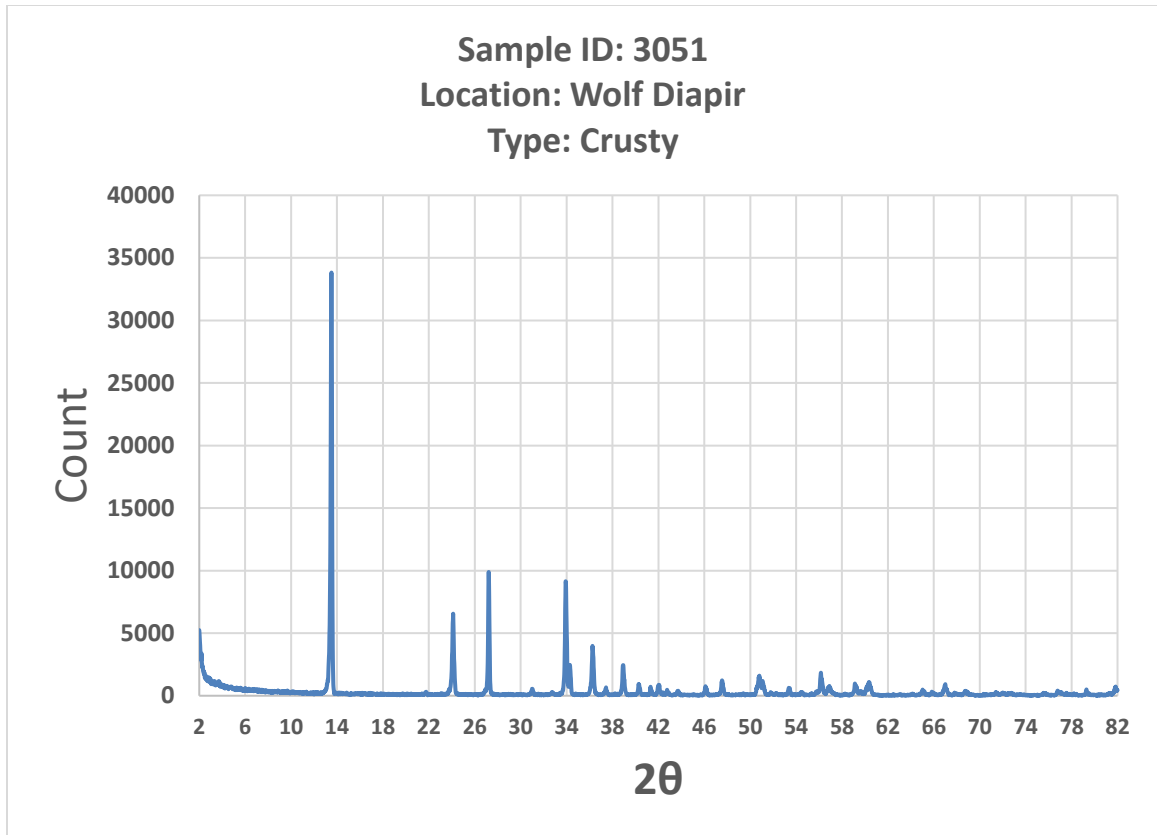|	
Name:	Elise Harrington

Post-secondary Education and Degrees:

Simon Fraser University
Burnaby, British Columbia, Canada
2010-2016 B.Sc. (Honours)

The University of Western Ontario
London, Ontario, Canada
2016-2018 M.Sc.

Honours and Awards:

Alexis Clague Award in Earth Sciences
Simon Fraser University
2015

Province of Ontario Graduate Scholarship
2016-2017

Career Development Award
Lunar and Planetary Institute
2017

Northern Scientific Training Program
Northern Studies Committee, Government of Canada
2017

Natural Sciences and Engineering Research Council (NSERC)
Canada Graduate Scholarship – Master's Program
2017-2018

Related Work Experience

LPI Summer Intern Program in Planetary Sciences
Lunar and Planetary Institute
2014

Misasa International Summer Internship Program
Institute of Planetary Materials, Okayama University
2015

Teaching Assistant
The University of Western Ontario
2016, 2018

Publications:

Trieman, Allan. Harrington, Elise. Sharpton, Virgil. (2016). Venus' radar-bright highlands: Different signatures and materials on Ovda Regio and on Maxwell Montes. Icarus, 280, 172-182.

Morse, Zach. Harrington, Elise. Christoffersen, Peter. Hill, Patrick. Newman, Jennifer. Choe, Byung-Hun. Tornabene, Livio L. Caudil, Christy. Osinski, Gordon R. (2018). The Use of GIS and immersive technologies in the CanMars Mars Sample Return Analogue Mission: Advantages for science interpretation and operational decision-making. Planetary and Space Science (Submitted – Submission no: PSS_2018_6).